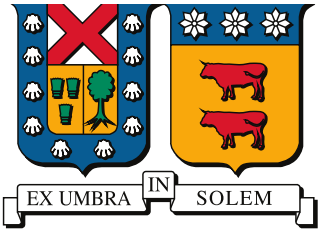

UNIVERSIDAD TECNICA
FEDERICO SANTA MARIA

Modeling of GaN-based DC-DC Converters with Model Predictive Control and Active Thermal Control for Powertrain applications in Electric Vehicles

Thesis presented by
Jhonattan Gabriel Berger Díaz
as a partial requirement for the title of
Ingeniero Civil Electrónico
and for the degree of
Magister en Ciencias de la Ingeniería Electrónica

Professor Guide
Dr. Christian Rojas Monrroy

Internal Examiner
Dr. Samir Kouro

External Examiner
Dr. Abraham M. Alcaide

March 18th, 2023, Valparaiso, Chile

La vida es una fiesta en la que coincides con mucha gente, van llegando nuevos invitados, pero también hay otros que, por la razón que sea, se van antes. A todos nos tocará irnos algún día, no se olviden. Lo peor de todo es asumir que la fiesta continúa sin nosotros.

-Merlí

We cannot choose the times we live in, but we can choose what to do with the time that is given to us.

-Gandalf

ACKNOWLEDGEMENT

I WOULD like to express my deep gratitude to all those who have contributed to my academic preparation, and most especially, to my thesis supervisor, Professor Christian Rojas. I also appreciate the support from Professors Samir Kouro, Juan Yuz, César Silva and Abraham M. Alcaide for their contributions to the development of my academic training.

This work was supported by FONDECYT under grant N° 1210757, by the Advanced Center of Electrical and Electronics Engineering (AC3E) under BASAL Project FB0008, and by the Dirección de Postgrado y Programas, Universidad Técnica Federico Santa María, Valparaíso, under Grant PIIC-025/2023.

My sincere thanks for the friendship and support of all the members of the Power Electronics Research Laboratory, PowerLab, Universidad Técnica Federico Santa María. Special thanks to Rodrigo Bugueño, Alejandro Peralta, Alan Wilson, Alejandro Stowhas, Katia Urrutia, Sebastián Salinas, Dave Figueroa, Iván Choque, Alexander Palacio, Pedro Mora, and many others who were always willing to help me. Thank you all for your assistance in the laboratory and for sharing great moments during these years. I would like to extend my heartfelt appreciation to my university friends who have been an integral part of my academic journey. Our shared experiences have enriched my time at the university. Thank you to Matías Huichaqueo, Daniel Gross, Sebastián Hernández, Gerald Lavergne, Fernando Álvarez, Katherine Vicencio, Camila De Améstica and David Tapia, among others, for your support, discussions, and occasional study sessions. Your presence has added a valuable dimension to my university life, and I am grateful for the shared moments that made this journey memorable. Gratitude to my closest friends, David Pizarro, Joaquín Agusto, and Diego Tapia; your encouragement and understanding made this challenging journey a bit more bearable. Heartfelt thanks to Carmen Carrasco for the laughter, encouragement, and occasional distractions that kept me sane throughout this thesis adventure.

I genuinely appreciate the fundamental support of **my family**, especially my mother, Iralin Díaz, and Alejandro Silva, who always supported and encouraged me to keep going. To my father, Gabriel Berger, who consistently supported and advised me wisely. To my sister, Nilari Berger, who inspired me with all her achievements. To my grandparents, Gabriel Berger and Teresa Cabrera, Mrs. Teresa Fernández, and Mr. Carlos Silva, thank you for always spoiling me and showering me with your love. This work belongs to all of you.

Jhonattan Gabriel Berger Díaz

ABSTRACT

IN recent decades, as the demand for more sustainable and environmentally friendly energy sources has grown, there has been a significant increase in the utilization of electric transportation. This surge in electric transport usage has brought forth new challenges for power electronics. One of the primary challenges posed by this advancing technology is the efficient management of energy flows inherent in electric vehicles.

Within the spectrum of power flows in electric vehicles, a pivotal aspect concerns the transfer of energy between the energy storage system and the mechanical power transmission, facilitated through the DC link within the vehicle. This power flow exhibits a bi-directional nature – during conduction mode, energy moves from the storage system to the powertrain, and during regenerative braking, this direction is reversed, with energy flowing from the powertrain to the storage system.

Consequently, DC-DC converters play a pivotal role in managing this power flow by connecting the storage system with the DC link of the vehicle. The essential characteristics that these power converters must possess include the ability to operate bidirectionally, maintain a constant voltage on the DC link, and adapt the voltage level of the storage system to that of the inverter. Therefore, the effective implementation of control loops becomes imperative for ensuring their optimal performance.

In this work is presented a Continuous-Control-Set Model Predictive Control (CCS-MPC) proposed for DC-DC converters for EV powertrains based on Gallium Nitride High Electron Mobility Transistors (GaN HEMTs) devices. The CCS-MPC allows full control of system states by adopting a multi-objective control approach, ensuring optimal power exchange between the DC link bus and a battery.

The main contribution is a systematic implementation of the thermal-management of power devices by including an Active Thermal Control (ATC) in order to mitigate the thermal stress in the semiconductors, in the context of CCS-MPC. The secondary contribution is to verify the proposed method in a Two-Level Buck Converter (TLBC), used in EV applications for e.g. auxiliary battery charging interfaces. Finally, simulation and experimental results are presented to verify the performance of the proposed control scheme.

Keywords

- Model Predictive Control (MPC)
- Active Thermal Control (ATC)
- DC-DC Converter
- Gallium Nitride (GaN)
- Electric Vehicle (EV)
- Two-Level Buck Converter (TLBC)

CONTENTS

List of Figures

List of Tables

ACRONYMS

AC	: alternate current
ATC	: active thermal control
CCS-MPC	: continuous control set model predictive control
DC	: direct current
DSP	: digital signal processor
dq	: direct quadrature
E-HEMT	: enhancement mode high electron mobility transistor
EV	: electric vehicle
FCS-MPC	: finite control set model predictive control
FPGA	: ield programmable gate array
HEMT	: high electron mobility transistor
HMI	: human machine interface
GaN	: gallium nitride
IGBT	: insulated gate bipolar transistor
KKT	: karush-Kuhn-Tucker
MOSFET	: metal-oxide-semiconductor field-effect transistor
MPC	: model predictive control
PI	: proportional-integral coefficients of linear controllers
PWM	: pulsewidth modulation
ZOH	: zero order holder

SYMBOLOGY

Matrices

$\mathbf{A}$	: state matrix, $\mathbf{A} \in \mathbb{R}^{n \times n}$
$\mathbf{B}$	: input matrix, $\mathbf{B} \in \mathbb{R}^{n \times p}$
$\mathbf{C}$	: output matrix, $\mathbf{C} \in \mathbb{R}^{q \times n}$
$\mathbf{D}$	: feedforward matrix, $\mathbf{D} \in \mathbb{R}^{q \times p}$
$\mathbf{I}$	: identity matrix, $\mathbf{I} \in \mathbb{R}^{n \times n}$

Vectors

$\mathbf{x}$	: state-variables, $\mathbf{x} = [x_1 \ x_2 \ \cdots \ x_n]^T$
$\mathbf{u}$	: input variables, $\mathbf{u} = [u_1 \ u_2 \ \cdots \ u_p]^T$
$\mathbf{y}$	: output variables, $\mathbf{y} = [y_1 \ y_2 \ \cdots \ y_q]^T$
$\mathbf{y}^*$	: reference variables, $\mathbf{y}^* = [y_1^* \ y_2^* \ \cdots \ y_q^*]^T$
$\mathbf{S}$	: firing pulses, $\mathbf{S} = [S_1 \ S_2 \ \cdots \ S_r]^T$

Scalars

M	: prediction horizon
N	: receding horizon
J	: cost function

Superscripts

$*$	: references
k	: k-th sampling time, $\mathbf{x}(kT_s) \equiv \mathbf{x}(k) \equiv \mathbf{x}^k$
min	: minimum value, e.g., $g^{\min}$
max	: maximum value, e.g., $g^{\max}$

Chapter 1

INTRODUCTION

1.1 State of the Art Review

ENERGY transition is a mandatory target for next decades, where alternatives such as sustainable clean energy and electromobility applications can help to achieve emission goals of the transportation sector [1]. The estimated and measured CO2 levels by NASA are shown in Fig. 1.1.

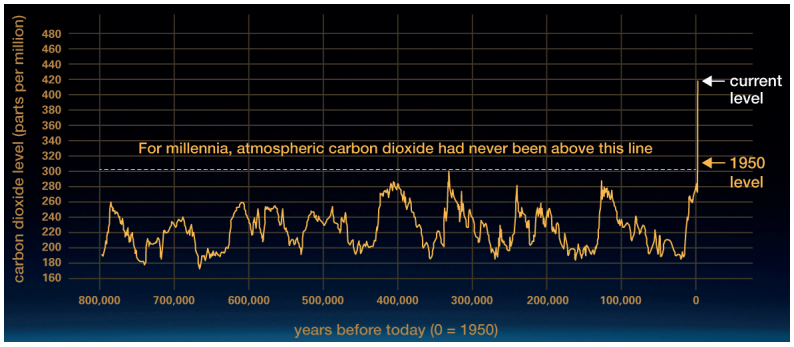

Figure 1.1: NASA estimate and measurements of CO2 level [1]

In Fig. 1.2, the breakdown of carbon dioxide (CO2) emissions in the European Union (EU) is detailed, emphasizing road transportation as the primary contributor, mainly from combustion-based cars. In 2019, the majority of European road vehicles relied on diesel (67%) and petrol (25%).

Recognizing the urgency to address heightened CO2 levels, there is a crucial need for transformative measures. Electric vehicles (EVs) play a crucial role in providing a promising solution to mitigate the environmental impact of traditional road transportation. The integration of modern power electronics is fundamental in transportation applications, with a trend towards high-power density converter interfaces and a power-building-block design.

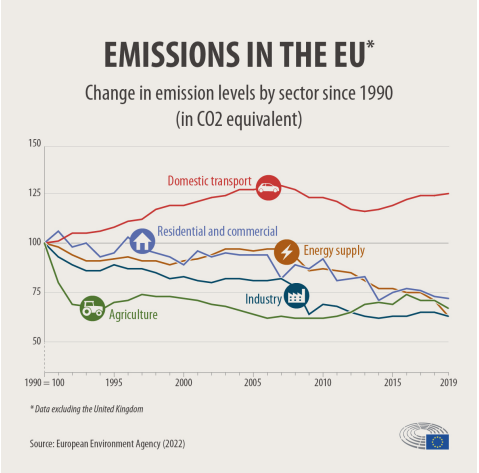

(a) Evolution of CO2 emission in the EU by sector.

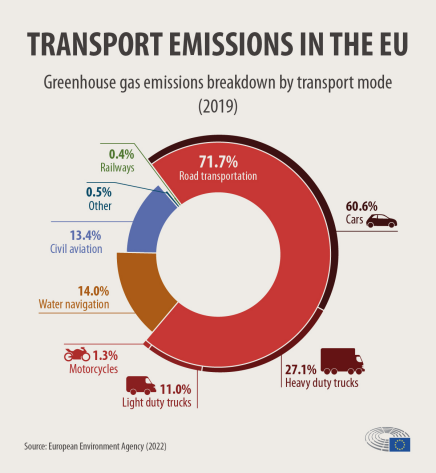

(b) Transport CO2 emissions in the EU.

Figure 1.2: CO2 emissions in the European Union (EU).

Nonetheless, it's imperative to recognize that EVs are not entirely exempt from environmental ramifications, as their manufacturing entails procedures and materials that may engender environmental repercussions [2,3]. These encompass the extraction of crucial battery constituents such as lithium, cobalt, and nickel, which give rise to environmental and social apprehensions [4,5]. Battery fabrication methods might produce emissions and waste, while dependence on specific metals may pose issues regarding their availability and demand. Additionally, the production of EV components such as electric motors entails processes that could yield pollutants. The energy consumed in EV manufacturing, if derived from non-renewable sources, has the potential to contribute to greenhouse gas emissions [6].

Despite these concerns, the overall environmental benefits of EVs, especially when charged with renewable energy, often outweigh their manufacturing impacts. Ongoing research aims to enhance the sustainability of EV supply chains and manufacturing processes [7,8].

1.1.1 Power Converters and batteries in Electrical Vehicles systems

An EV powertrain typically consists of a battery pack, bidirectional DC-DC an DC-AC converters and an electric motor, as shown in Fig. 1.3. Bidirectional DC-DC converters are used to manage power flows between the main/auxiliary batteries and the inverter DC-link. Buck and boost converters are employed to supply power to the wheels during motor driving mode, while also facilitating the charging of the battery using regenerative energy generated during vehicle deceleration and braking. In this work a Two-Level Buck Converter (TLBC) to charge auxiliary batteries in Fig. 1.3 is studied.

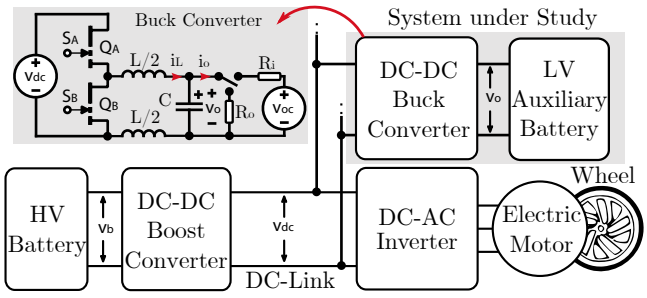

Figure 1.3: EV Powertrain and system under study.

Nonetheless, the energy generated during deceleration and braking is insufficient to fully recharge the batteries. As a result, the power electronics configuration in a standard Electric Vehicle Supply Equipment (EVSE) adopts a two-stage system, depicted in Fig. 1.4. This system consists of a rectifier stage equipped with power-factor correction (PFC) linked to AC mains. The AC mains connection can be either single-phase or three-phase, depending on the power requirements. Subsequently, a DC-DC stage takes charge of regulating the battery voltage and current. As illustrated in Fig. 1.4, a crucial component in the system is the galvanic isolation stage, consistently present to meet the stringent leakage current requirements set by standards such as IEC 61851-23, JEVS G105-1993, SAE J1772, and UL 2231. The placement of this isolation stage depends on design considerations, with options including low-frequency (LF) deployment at 50/60Hz, necessitated by the grid connection, or high-frequency (HF) integration within the DC-DC stage, employing technologies like the Dual Active Bridge (DAB). The latter approach is chosen to minimize transformer size, even though the cost of high-frequency transformers exceeds that of their low-frequency counterparts.

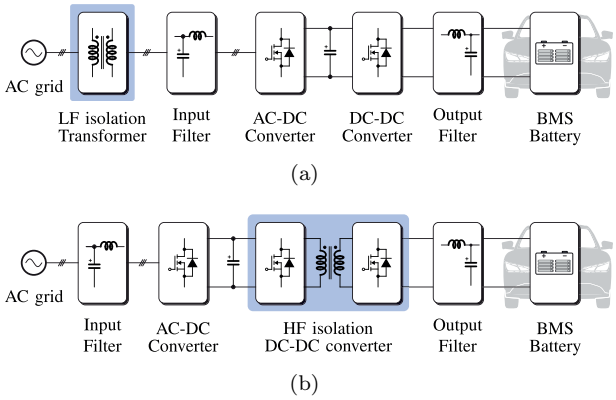

Figure 1.4: General structure of an EV battery charger. Galvanic isolation can be either at (a) LF or (b) HF where applicable. Although less frequent, some approaches feature both isolations in order to enable simultaneous charging and other features [9].

Currently, there are various types of Electric Vehicles (EVs) available in the market. Based on their drive train configurations, EVs can be categorized as Battery Electric Vehicles (BEVs), Plug-in Hybrid Electric Vehicles (PHEVs), Hybrid Electric Vehicles (HEVs), and Fuel Cell Electric Vehicles (FCEVs). The fundamental layouts of these configurations are illustrated in Fig. 1.5.

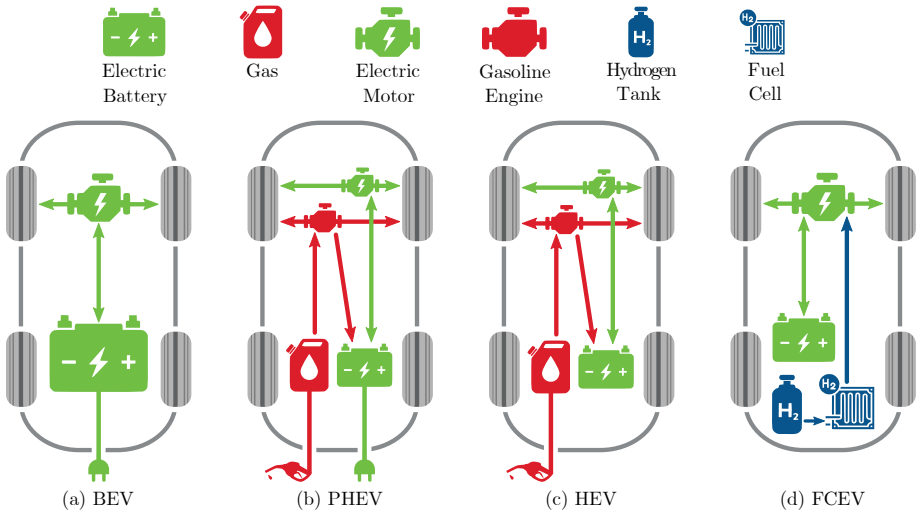

Figure 1.5: Types of Electric Vehicle [10].

BEVs commonly use Lithium-ion (Li-ion) batteries due to their high energy density and extended lifespan [11], see Tab. 1.1 and Fig. 1.6. The State of Charge (SoC) indicates the remaining battery charge as a percentage, and monitoring and managing SoC are crucial for optimizing battery lifespan and performance. Ongoing research explores advancements in Li-ion batteries and emerging technologies like solid-state batteries, aiming for higher energy density and faster charging. Effective SoC management and optimal charging practices significantly impact the longevity and efficiency of EV batteries.

Table 1.1: Comparison of major battery technologies [11].

Battery Type	Nominal Voltage (V)	Specific Energy(Wh/kg)	Energy Density(Wh/L)	Specific Power (W/kg)	Life Cycle
Pb-acid	2.1	30-40	100	180	500
Ni-Cd	1.2	50-80	300	200	2000
Ni-MH	1.2	60-120	180-220	200-300	<3000
ZEBRA	2.6	90-120	160	155	>1200
Li-ion	3.6	120-250	200-600	200-430	2000
LiPo	3.7	130-225	200-250	260-450	>1200

Pb-acid: Lead Acid, Ni-Cd: Nickel-Cadmium, Ni-MH: Nickel-Metal Hydride, ZEBRA: Zero Emissions Batteries Research Activity, Li-ion: Lithium-ion, LiPo: Lithium-ion polymer.

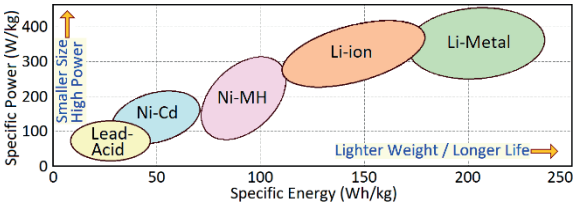

Figure 1.6: Power and energy capabilities of different batteries [11].

In [12], the focus is on maximizing powertrain efficiency through the implementation of a Smart Adjustable DC Link with IGBTs and SiC MOSFETs, with particular emphasis on precise DC-Link Voltage Control. Without this control, efficiency becomes dependent on the battery State of Charge (SoC). However, the degradation of energy efficiency due to varying battery SoC levels is mitigated when employing adjustable DC-link voltage powertrains, making the powertrain efficiency less sensitive to changes in battery SoC.

On the other hand, in [13], the emphasis is placed on maintaining a Li-ion battery within the optimal temperature range to ensure excellent performance and an extended lifespan. The paper proposes a control-oriented model for the Battery Thermal Management System (BTMS), which includes an electric pump, cooling plate, and radiator.

Different charging methods are outlined in Tab. 1.2. Conventional Charging, Level 1, utilizes standard power outlets for slower but convenient overnight charging, while Level 2 is suitable for short to long charging times, such as when parked in work buildings. Fast Charging, Level 3, involves DC fast-charging stations for rapid charging during long trips [14]. However, the IEEE 2030.1.2 standard currently stipulates that fast charging systems can accommodate powers up to 500 kW, while the IEC 61851-1, 3rd edition 2017 standard specifies that they can operate with voltages up to 1000V. This contrasts with the information provided in [14].

There are other charging methods, such as Wireless Charging, which is still in development. It uses magnetic induction for cable-free charging, allowing the EV to charge while driving on the road.

Table 1.2: Charging level parameter comparison [14].

Item description	Level 1	Level 2	Level 3
Speed	Slow charging	Slow/semi-fast charging	Fast charging
Charger location	Onboard	Onboard	Offboard
Connection to vehicle	AC	AC	DC
Typical use	Home	Home and work	Charging station
Typical charging time	6-10 h	30 min to 4 h	15-50 min
Power level	1.1-3.3 kW	3.3-19.2 kW	20-150 kW
Voltage	120 V	208 or 240 V	480 V
Number of phases	Single phase	Single/three phase	Three phase

Another current and ongoing research focus is Vehicle-to-Grid (V2G) [15], enabling EVs to function as Energy Storage Systems (ESS) [16], akin to Battery Storage Systems (BESS). The main driver for adopting Vehicle-to-Grid (V2G) technology is the energy imbalance that occurs during the day, often covered by gas-based, polluting energy. This approach aligns well with renewable

energy sources, as their peak generation usually coincides with low energy demand as can be seen in Fig. 1.7. Companies are conducting tests to understand how flexible charging can benefit smart grids, even proposing monetary incentives for users of this technology. V2G technology enables monitoring and controlling the interaction between electric vehicle batteries and the power grid, leveraging parked cars for flexible charging to address daily energy imbalances.

A bidirectional management system offered by an automotive and energy storage company, aims to charge batteries during off-peak hours and extract energy from parked vehicles when needed. This storage capacity supports grids with high renewable energy presence, utilizing low-pollution excess generation during periods of low demand.

The primary challenge is economic, as both vehicles and batteries are costly. To showcase the potential a utility company in USA proposed selling 50 cheaper buses with this technology to schools. V2G technology is complex and currently not very consumer-friendly, requiring infrastructure safety assessments and often relying on offline information [17].

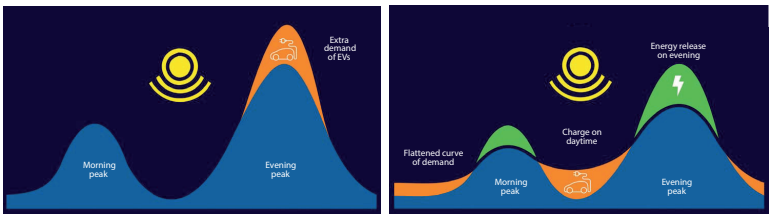

(a) Without V2G (b) With V2G

Figure 1.7: Powerloop demand scenario with and without V2G, showing flattened peaks [15]

In distributed power systems within smart grids and microgrids [18], a prevalent architecture features a common DC bus that connects various renewable energy sources, such as wind turbines and Photovoltaic (PV) panels, to loads like batteries and data centers [19]. Consequently, the modeling and stability analysis of cascaded DC-DC systems are crucial considerations, particularly in the context of EV systems.

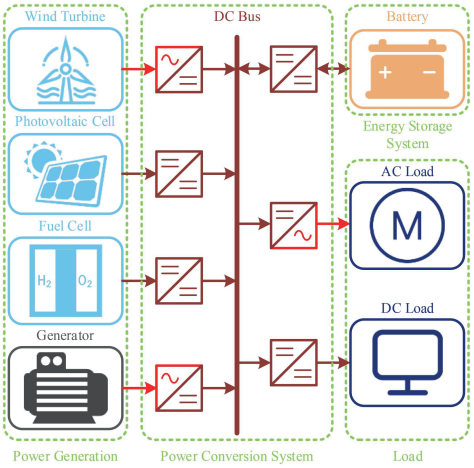

Figure 1.8: Typical distributed power system [19]

In summary, power electronics are crucial in modern power systems, enabling efficient energy conversion, grid integration of renewables, and enhancing overall energy efficiency across various applications. They play a vital role in shaping sustainable energy systems and enabling the transition towards a more electrified world.

1.1.2 Power semiconductors

For bidirectional operating characteristics in powertrain converters, it is imperative to structurally design them based on bidirectional semiconductors. At present, the predominant technology employed in most power converters is Silicon Carbide (SiC) MOSFET, chosen for its ability to handle high voltage and current levels while sustaining operation at elevated temperatures. Nevertheless, recent years have witnessed the emergence of semiconductors based on Gallium Nitride (GaN) technology. These novel devices demonstrate superior performance attributes, encompassing heightened power density, diminished switching losses, and enhanced overall efficiency in comparison to SiC. However, GaN semiconductors maximum voltage tolerance is currently capped up to 1200V [20–22]. Fig. 1.9 provides a comprehensive comparative analysis of diverse semiconductor technologies across various applications, where SiC and GaN domains coexists in electromobility.

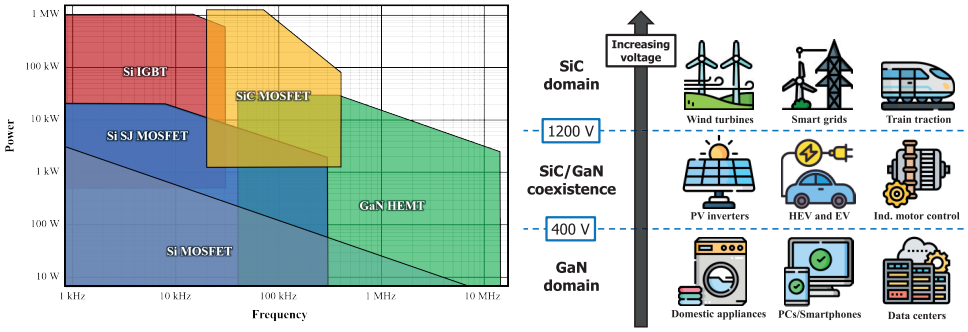

(a) Frequency and power regimes.

(b) Fields of interest for GaN and SiC.

Figure 1.9: Techonology power devices (a) comparison in frequency and power regimes and (b) current and future fields for GaN and SiC [22]

The GaN Enhancement mode High Electron Mobility Transistor (E-HEMT) semiconductors are capable of operating as power semiconductors, similar to MOSFETs or IGBTs, while leveraging the inherent benefits offered by GaN technology. Structurally, GaN E-HEMT devices exhibit three connection terminals identified as gate (G), drain (D), and source (S), conforming to the standard configuration of widely adopted power semiconductors. This structural representation is elucidated in Fig. 1.10. The figure also showcases the electrical symbol utilized for GaN-HEMT semiconductors, conduction modes, and the I/V characteristic curve.

Several challenges in GaN devices [23] include mis-triggering due to crosstalk and electromagnetic interference (EMI) induced signal integrity issues, particularly given GaNs' operation at high frequencies. Additionally, the Miller effect, also known as cross-talk or Miller turn-on, poses a significant concern. This phenomenon involves synchronous devices unintentionally turning on when the complementary device in the same phase leg is intentionally activated. Consequently, both switches in the phase leg activate simultaneously, creating a short circuit across the DC link and resulting in a shoot-through event. A common solution to mitigate this issue involves applying a negative bias at the gate during turn-off. For instance, the GS66516B operates

with a gate voltage of 6/-3V. However, it is important to note that this approach may compromise the third quadrant behavior (Zone C, Fig. 1.10) of the GaN HEMT and lead to increased energy loss during the dead-time period [24].

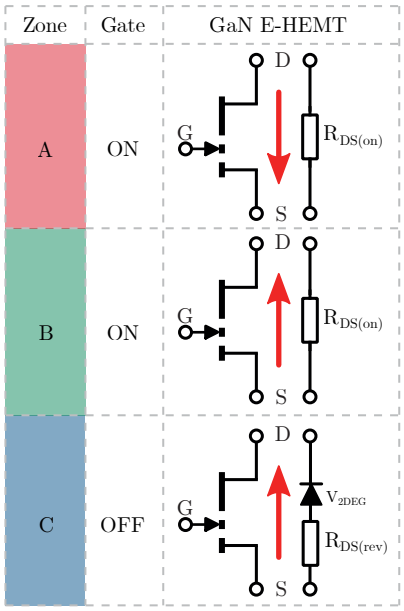

(a) GaN conduction modes

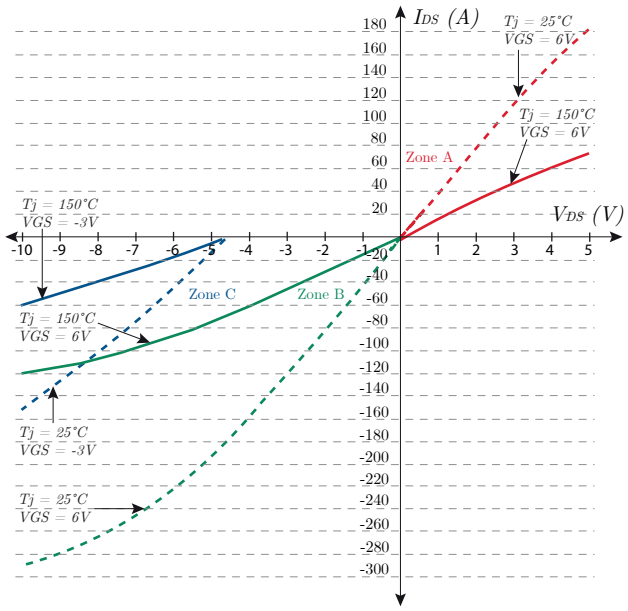

(b) I_{DS} vs V_{DS} characteristic curve at different temperatures

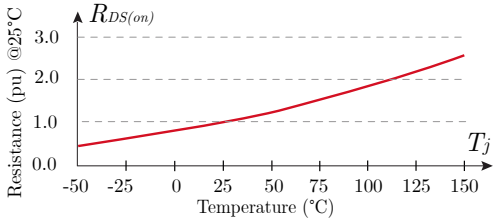

(c) Normalized $R_{DS(on)}$ as a function of T_j

Figure 1.10: GaN module (a) conduction modes and (b,c) GS66516B characteristic curves [25]

Considering that the conduction resistance ($R_{DS(on)}$) and thermal resistance from junction to heatsink (R_{thJ-HS}) of GaN with Insulated Metal Substrate (IMS) are generally smaller compared to other device technologies, GaN devices can effectively operate at higher frequencies without reaching hazardous junction temperatures (T_j). It is crucial, however, to acknowledge inherent limitations, as elevated temperatures may still be attained, resulting in an increase in $R_{DS(on)}$ relative to T_j, this is illustrated in Fig. 1.10.c. To model and estimate power losses accurately in GaN [26], as well as to understand their impact on T_j, a comprehensive consideration of this temperature-dependent relationship is mandatory.

In [27], a comparative analysis is presented between SiC MOSFETs and GaN HEMTs for high-frequency operation in EV Battery Charger applications. The system operates at 7.2 kW, with the findings summarized in Table 1.3.

Table 1.3: The Overall Charger Comparison (4 GaN HEMTs vs 2 SiC MOSFETs) [27].

Metrics	Comparison
Conduction loss	SiC ≈ GaN (@100°C)
Dead-band loss	GaN > SiC
Switching-on loss	GaN = SiC = 0
Switching-off loss	SiC > GaN
Gate-drive power	SiC > GaN
Thermal capability	SiC ≈ GaN
Cost	SiC > GaN
Power Density	GaN > SiC
Efficiency	GaN ≈> SiC

In Fig. 1.11, the IGBT conduction modes and the I/V characteristic curve at different junction temperatures are illustrated. A comparison between Fig. 1.10 and Fig. 1.11 reveals that GaN exhibits highly linear behavior across a wide current range, with a conduction resistance smaller than that of the IGBT in both Zone A and B. In Zone B, GaN operates linearly, while the IGBT module functions as a diode. However, Zone C indicates that GaN possesses a greater forward diode voltage than the IGBT module, implying more losses during the dead-time. Nevertheless, GaN requires less dead-time than IGBT, highlighting a trade-off in this aspect. In [28], an electro-thermal model of a Floating Interleaved Boost Converter (FIBC) with IGBT devices is implemented in a Field Programmable Gate Array (FPGA) to simulate the IGBT thermal behavior in real-time. The FIBC network model can effectively be simulated with a 500ns time step, producing the insulated-gate bipolar transistor transient switching waveforms authentically with a 5ns resolution.

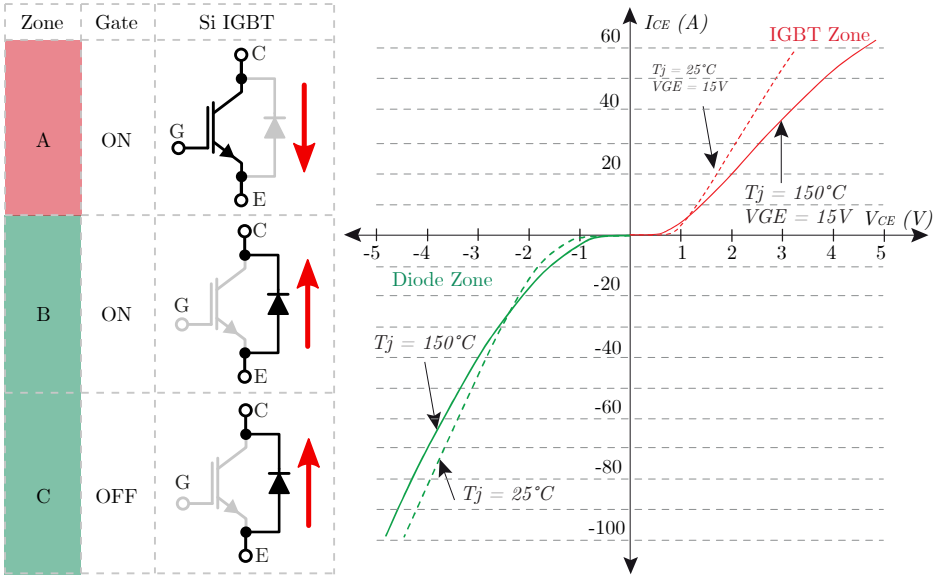

(a) IGBT conduction modes

(b) I_{CE} vs V_{CE} characteristic curve

Figure 1.11: IGBT module conduction modes and SK25GH12T4 characteristic curve [29]

1.1.3 CCS-MPC in Power Electronics

Static converters conventionally rely on modulators to generate firing pulses, utilizing an external reference signal and real system measurements. This reference signal can be externally generated in an open-loop operation or provided by a control scheme in a closed-loop system, with the control scheme adopting either a linear or non-linear form. In the field of power electronics, PI controllers are commonly employed for linear control, while non-linear methods may encompass dead-beat controllers or hysteresis control.

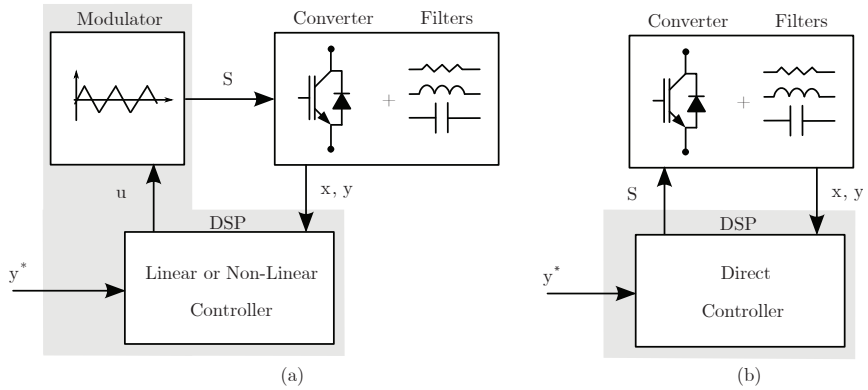

Figure 1.12: Comparison between conventional and direct controllers: (a) conventional controller; (b) direct controller [30].

Two noteworthy non-linear methods involve generating firing pulses directly without any modulation stage: Finite Control Set Model Predictive Control (FCS-MPC) and Selective Harmonic Elimination (SHE) techniques. These methods have been extensively studied in the literature [31, 32], standing out for their effectiveness. Conventional and direct controller schemes are illustrated in Fig. 1.12.

Over the last decade, Model Predictive Control (MPC) has gained global popularity due to its simplicity and intuitive nature. MPC is a potent approach that necessitates a model of the system to calculate the optimal input to be applied within a predefined prediction time horizon N. By minimizing a cost functional that describes the control objective, a parameterized control input sequence is to be found by solving an optimal control problem (OCP) subjected to an initial condition, corresponding system dynamics, and constraints of the system states and control inputs. The feedback is achieved in MPC by the receding horizon principle that at each sampling period, the prediction horizon is moved forward into the future by one step, while applying only the first control input from the obtained control sequence to the plant. While MPC demonstrates strong performance in well-studied and non-linear systems, it may not be suitable when an accurate model is unavailable. The utilization of Digital Signal Processors (DSP) and the development of powerful and fast microprocessors have made it possible to implement MPC in the power electronics field. The technique offers advantages over linear control, as linearization often results in information loss about the system model. Linear control theory typically relies on continuous control for stability, observability, and controllability analysis. However, for real-time applications, these control techniques must be discrete, leading to the development of discrete control theory.

In power converters, even when the control is continuous, the input signals exhibit a switching

nature. Continuous inputs of the controller are, therefore, transformed into discrete inputs using modulators. This realization emphasizes the importance of employing discrete-time controllers in digital platform implementations [33].

In MPC, there also exists Continuous-Control-Set Model Predictive Control (CCS-MPC), presented as a viable alternative for modern power converters [34]. One advantage of CCS-MPC is its flexibility, capable of handling different types of variables and incorporating specific hard restrictions into the cost function, similar to FCS-MPC. However, the main distinction is that the control inputs in FCS-MPC are, as the name suggests, finite. For example, the firing pulse of a switch is either 0 or 1. In CCS-MPC, the control input is sent as the duty cycle of the firing pulses and can have values from 0 to 1, providing continuity. The real-time computation of a long-horizon MPC implementation remains a challenge in WBG semiconductor devices systems [35], such as GaN-based DC-DC converters, due to their high-frequency commutation nature [36–39]. However, in CCS-MPC, this limitation is absent, as the sampling frequency does not need to be the same high switching frequency to control the converter. The optimization algorithm might be numerical or analytical by using a deadbeat function solved [40, 41]. Furthermore, thermal management in GaN-based DC-DC converters is imperative for reliable operation in EV applications. In general, power converters can be modeled as bilinear systems [42–45] for electrical and thermal subsystems.

Despite the advantages of various control techniques, each has its limitations. For example, PI controllers, commonly used in linear control, exhibit non-linearity during converter operation, necessitating an anti-windup scheme to prevent controller integration and address intrinsic input actuation saturation, such as duty cycle limitations from 0 to 1. SHE has a better harmonic spectrum due to efficient elimination of dominant harmonics. However, closed-loop control with this method is limited to slow systems such as SAG mills. MPC, although powerful, encounters limitations such as computational calculation time, model mismatch, challenging determination of weighting factors, and insufficient long-horizon prediction. Additionally, FCS-MPC, by not using a modulator with a fixed switching frequency, introduces random harmonics in the output signal, which may pose risks in systems with resonant frequencies. This aspect is considered in [46], achieving a pseudo fixed switching frequency with FCS-MPC for a two-level inverter and an induction machine. Similarly, this aspect is achieved in [47] in a Single-phase three-level NPC converter with IGBT devices.

Regarding the implementation of any control technique in a discrete system, a process of discretization is mandatory. For linear systems, the Zero Order Hold (ZOH) method is often the best approach, even when the system may contain time delays. However, for non-linear systems, the Taylor series is considered one of the most effective discretization techniques [48–51]. However, a high-order Taylor series is computationally expensive. Therefore, the forward Euler method is preferred in case of long-horizon MPC implementation due to its low computational time [52], which is equivalent to the first-order Taylor series, although it requires a relatively high sampling frequency.

Typically, to analyze and adjust a continuous linear controller for a linearized system with time delay, Padé approximation is used. Yet, this complicates the design, and eventually, this continuous controller will be discretized for implementation. Therefore, another advantage of non-linear controllers, such as MPC, is their capability to easily model and consider time delays [53].

In [54, 55], CCS-MPC is proposed for a three-level Flying Capacitor Boost Converter (FCBC) with a constant switching frequency, demonstrating that CCS-MPC has a better dynamic response than a PI controller while, in addition, optimally considering current saturations and duty cycles. Also, a Luenberger observer is used to take advantage of the fact that MPC has faster dynamics

and its response is better when there are fluctuations in input voltage and load conditions.

Bilinear systems, incorporating both linear and nonlinear dynamics, are integral to MPC in Power Electronics Systems. MPC utilizes detailed bilinear models for accurate predictions, effectively managing nonlinearities and optimizing system performance. CCS-MPC has been applied to address uncertainties in bilinear systems, as observed in [43]. However, CCS-MPC is predominantly employed for current control loops in power electronics, showcasing its adaptability in challenging modeling scenarios.

In [56], a modulated MPC, equivalent to CCS-MPC, is proposed for a Modular Multilevel Converter (MMC) operating in a wide frequency range. An exhaustive active-set method is used to evaluate all possible active sets until the Karush-Kuhn-Tucker (KKT) conditions are satisfied, since this method can guarantee that the optimal solution can definitely be found [57]. This process is done with matrix inversion, and therefore, this method suffers from a heavy computational burden.

Then in [58], a CCS-MPC is proposed to control two Permanent Magnet Synchronous Motors (PMSM) with a Five Leg Voltage Source Inverter (FL-VSI). Conventional speed and current control methodologies employing Proportional-Integral (PI) controllers in the dq reference frame are implemented. However, the duty cycles that must be applied to each leg are obtained with CCS-MPC, considering that one of them is connected to both motors. Again, KKT conditions are used. However, in this case, explicit control laws are obtained to calculate the duty cycle. Yet, as not all cases are evaluated, it is not ensured that the optimal solution can definitely be found. In this work, if the global optimum does not fulfill constraints, then four boundary solutions limit their duty cycles if they are larger than 0 or 1 to the nearest value and finally evaluate the cost function to determine which one achieves the smallest value.

In [59], a CCS-MPC is proposed for the control of a PMSM using a Two-level Voltage Source Inverter (2L-VSI). The method incorporates a field weakening operation, addressing the Optimization Problem (OP) through Quadratic Programming (QP) and employing a dual-active set solver from [60]. The approach involves the inversion of the KKT matrix with iterative cases. Real-time experiments demonstrate execution times and iteration numbers ranging between 50 to 100 microseconds.

Similarly, in [61], the OP for a PMSM with a 2L-VSI is solved using QP, with the inclusion of a Kalman filter to mitigate measurement noises. While Explicit Model Predictive Control (EMPC) is discussed, its attractiveness diminishes with an increasing number of regions in the resulting Piecewise Affine (PWA) controller, as it may demand a substantial amount of memory. Instead, a QP solver based on an active-set method is presented to address the OP within a time limit of 0.3 ms. This timeframe encompasses ADC sampling, state estimation, and real-time optimization.

Also in [62] for PMSM with a 2L-VSI IGBTs devices a CCS-MPC is proposed to obtain minimal steady-state ripples, tracking offsets, over/undershoot, and fast dynamic response. The proposed control scheme based on the Interior-point IP numerical solver was experimentally tested on an IPMSM and an SMPMSM.

In [63], a Geometrical Modulated MPC (GM^2PC) for grid-connected converters is introduced. This method employs a geometrical solution based on KKT conditions. The effectiveness of the approach is validated by its capability to restrict the converter-side currents, synthesize reference voltages with a fixed switching frequency, and adeptly address the overmodulation issue, all achieved efficiently on low-cost DSPs.

Similarly, in [64], a Space Vector Modulated MPC (SVM2PC) for VSI is proposed. KKT conditions are used, and computation is made offline, storing the data in the program memory of the DSP. The control algorithm has a very low computational burden, closed-loop responses have

low settling times, low THD, small tracking errors under strong and weak grid conditions, and operation both in linear and overmodulation regions.

In [65], a critical soft switching principle with optimal-frequency MPC is proposed for a TLBC based on SiC devices to eliminate the turn-on losses, especially during the transient period. It is concluded that the traditional PI controller cannot guarantee the critical soft switching during the transient period because of the oscillation. To compute MPC solution, the Newton iterative method is used, and if the sampling time is not long enough, the maximum feasible frequency is directly calculated according to the critical soft switching constraints. Then in [66], this method is implemented and shows a significant improvement in efficiency.

In [67], CCS-MPC based on PWM plus triple-phase shift (TPS) modulation is proposed in a DAB converter with MOSFETs to improve dynamic performance, as well as to maintain the output voltage level of DC-DC converters. To expand Zero Voltage Switching (ZVS) range, it minimizes the circulating current and conduction losses. The simplicity of implementation PWM has combined with the triple-phase shift method to reduce current stress, reduces EMI interruption.

In [68], a study compares three control methods for regulating the output voltage of a GaN-based nine-level Flying Capacitor Converter (FCC) in DC/DC buck applications: Linear controller with Phase Shifted Pulse Width Modulation (PS-PWM), Finite Control Set - Model Predictive Control (FCS-MPC), and Sequential Phase Shifted - Model Predictive Control (SPS-MPC). The FCS-MPC method effectively controls state variables but exhibits non-periodic switching frequencies, resulting in poor FFT performance. In contrast, the SPS-MPC method combines both techniques, ensuring constant switching frequencies through PWM for Flying Capacitors (FCs) while utilizing a predictive model. This makes it suitable for non-linear systems, capable of regulating inner and output voltages, and maintaining lower error in steady state, crucial for GaN-based converters operating at high frequencies with small dead-times.

1.1.4 Active Thermal Control in Power Semiconductors

In contemporary power electronics research, the implementation of Active Thermal Control (ATC) has gained prominence as an essential strategy for optimizing performance and extending the operational life of power semiconductors [69]. This paradigm shift is particularly evident in the domain of EV powertrains, where efficient energy conversion plays a crucial role.

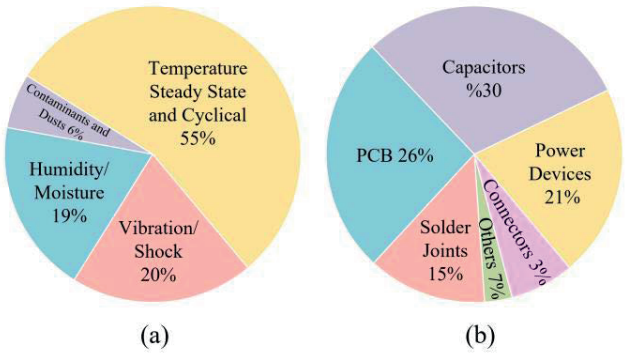

Figure 1.13: Surveys on failures of converters: (a) Distribution of sources of stresses for failures of electronic equipment (b) Failure distribution among major components in a typical converter [70].

Fig. 1.13 shows the failure rate of critical components of an inverter. As the core part of the drive system, the power semiconductors are very prone to failure due to their frequent on-off switching and the influence of thermal and electrical overstress. As illustrated in Fig. 1.13.a, temperature emerges as the primary stressor, constituting 55% of the overall distribution, thereby underscoring its significance in influencing the reliability of electronic equipment.

The implementation of ATC is demonstrated through various studies in the field of power electronics, including switching frequency variation and current limitation [71], as well as fan control [72, 73]. A study focusing on an H-Bridge configuration [74] utilizes IGBTs and employs hysteresis control to regulate the switching frequency. Subsequently, a separate study introduces an ATC scheme for a DC-DC Three-Level Buck Boost Converter [75], incorporating GaN devices and employing a Proportional-Integral (PI) controller to regulate the switching frequency. In both cases, the primary objective is to control the operating temperature of the semiconductors. The precision achieved through these control mechanisms not only alleviates thermal stress on the converters but also significantly extends the lifespan of the GaN devices, underscoring the importance of precise DC-Link Voltage Control.

Extending this theme, further exploration of the practical application of ATC in EV scenarios is presented in [76]. The study demonstrates a notable enhancement in junction temperature regulation based on a typical EV usage profile, emphasizing the efficacy of the proposed ATC scheme.

In a different context, [77] introduces an ATC scheme for a DC-DC Buck Converter utilizing MOSFET devices. This scheme incorporates modifications to the gate voltage during triggering pulses, operating in cut-off and saturation regions. The estimation of junction temperature through encapsulation temperature and power loss measurements plays a crucial role. The proposed control strategy is expected to result in a significant increase in the lifespan of the semiconductor devices.

Another innovative approach is proposed in [78], optimizing switching losses and power distribution in a hybrid H-bridge DC-DC converter. The design involves legs with different semiconductor technologies, such as Si-based devices, IGBTs, and diodes, operating at lower frequencies, and SiC-based devices, MOSFETs, operating at higher frequencies. A sophisticated loss model, considering power distribution and high-frequency switching, is presented, with the resulting algorithm estimating junction temperature and offering a comprehensive solution for effective control.

Another control approach is presented in [79], where FCS-MPC is employed in an ATC scheme for an MMC with incorporated IGBT devices. This strategy integrates Negative-temperature-coefficient (NTC) thermistors, commonly employed as temperature sensors, and power loss estimation to adjust the switch distribution. The algorithm aims to balance thermal stress across the converter. Leveraging FCS-MPC, the model utilizes each module through indirect control of the duty ratio and the equivalent switching frequency. This approach reflects a sophisticated method for temperature regulation and power loss management within the MMC structure. Then in [80], a Modulated MPC (M2PC) is proposed for the extremely low-frequency power amplifier (ELFPA) in Electromagnetic Wave Communication system (ELFEWC) to reduce the junction temperature swing of the power device and extend the life of ELFPA. The fixed switching frequency is selected by considering the tradeoff between junction temperature swing and total harmonic distortion to improve reliability.

An ATC system for a two-phase interleaved buck converter is introduced in [81, 82], employing MOSFET devices. The estimation of junction temperature relies on case temperature measurements, enabling the adjustment of current sharing through ratio configurations via a devised

Thermal Balancing Control (TBC). In [83], similarly a Thermal Distribution Analysis of MMC with IGBTs devices is proposed based on dc current modulation ratio.

An Electrothermal Performance-based (ETP) FCS-MPC for dynamic thermal balance control is proposed in [84], effectively eliminating the necessity for temperature sensors. The system utilizes Three-Level Neutral-Point-Clamped (3L-NPC) converters with IGBT devices in an Interior Permanent Magnet Synchronous Motor (IPMSM)-based traction drive.

The proposed models consider the impact of losses on both electrical and thermal behaviors, offering a more accurate representation for converter systems. Thus, the incorporation of ATC in modern power electronics stands as a promising avenue for achieving higher efficiency, reduced stress, and an extended lifespan of power semiconductors across various applications [70], with particular relevance to the growing field of electric mobility.

1.1.5 Summary

The application of CCS-MPC in GaN-based DC-DC converters presents a considerable challenge in managing electrical and thermal dynamics, which operate on distinct temporal scales—microseconds for current and hours for temperature. Despite this discrepancy, CCS-MPC exhibits adaptability in both domains. Notably, the integration of Karush-Kuhn-Tucker (KKT) conditions remains unexplored within this framework, thus prompting investigation in this thesis. This study endeavors to uncover the feasibility and effectiveness of CCS-MPC with KKT conditions, providing valuable insights into advanced control strategies for GaN-based systems.

1.2 Hypothesis and Contributions

The contribution of this research lies in presenting a novel control strategy for DC-DC GaN-based Converters, which utilizes CCS-MPC with a focus on KKT conditions to consistently attain optimal solutions. The primary hypothesis is that it is possible to mathematically model, simulate, and implement a two-level step-down DC-DC converter based on GaN technology, capable of efficiently handling power bidirectionally between the battery and the powertrain of an electric vehicle.

Furthermore, it is posited that the integration of an active thermal control scheme into the proposed CCS-MPC can effectively modify the switching frequency of the semiconductors, thereby reducing the thermal stress on devices. This technique is anticipated to outperform conventional PI control methods due to its faster dynamic response and improved disturbance rejection.

The performance of the converter, as obtained in simulation tests, can be validated through experimental tests in the laboratory.

1.3 General and Specific Objectives

The primary objective of this study is to design and implement a predictive control algorithm for a two-level bidirectional DC-DC buck converter employing GaN-based semiconductors. This converter facilitates power transmission between the battery and the powertrain of an electric vehicle, incorporating precise current and voltage control for battery charging, along with an active temperature control system.

The specific objectives are:

- Perform a state-of-the-art study on converters used for power transmission to and from the battery in electric vehicles.
- Study topologies and control schemes proposed by other authors.
- Develop an innovative solution incorporating a simple-to-implement topology as a proof of concept for evaluating predictive techniques based on electrical and thermal models.
- Build a converter simulation to test the designed control schemes.
- Validate the converter's performance based on simulation results.
- Experimentally implement the converter and validate the obtained results with simulations.

1.4 Methodology

The methodology to follow for the development of this work is:

- **Research:** Conduct a literature review on converters used in electric vehicles for power transmission to and from the battery.
- **Analysis:** Theoretical study of system models and design of control schemes.
- **Simulation:** Implement the chosen topology and designed control schemes in simulation for system validation.
- **Experimental Validation:** Implement a low-power hardware prototype of the proposed system, with reduced voltages and currents to validate the concept. Obtain experimental results to compare with simulation results.

1.5 Scope and Limitations

This research primarily focuses on the analysis, modeling, and control—both electrically and thermally—of DC-DC converters for electric vehicle applications, specifically within the powertrain. A two-level Buck converter is employed. The proposed system integrates the Continuous Control Set Model Predictive Control (CCS-MPC) technique with the aim of enhancing the control precision and response of the buck converter. Topics such as battery parameterization, various battery models and loads, the DC-AC converter model, and the electric machine model within the powertrain are not comprehensively addressed in this study.

The limitations of the work are:

- Unidirectional Load: The scope of this study is confined to resistive loads, excluding bidirectional loads. The implications and performance of the proposed control technique may differ in applications involving bidirectional energy flow.
- Semiconductor Loss Thermal Model: The thermal loss model of the semiconductors implemented in both experiments and simulations corresponds to the GaN E-HEMT GS66516 semiconductor model from the manufacturer GaN Systems.

- Low Voltage and Power: The experimental investigations focus on the buck converter's performance under low-voltage conditions, inherently limiting the power levels analyzed. Extrapolating the findings to high-power scenarios may require additional considerations.
- Frequency Limitation: The employed synchronous sampling technique imposes a maximum switching frequency of 300 kHz due to current probes constraints. It is feasible to switch at frequencies up to a maximum of 500 kHz; however, this upper limit is dictated by the measurement probes, which lack sufficient bandwidth to accurately sample the current.
- Specific Control Technique: The study primarily concentrates on the application of Continuous Control Set Model Predictive Control. Alternative control strategies, although relevant, fall beyond the immediate scope of this research.
- Thermal Dynamics Scaling in Simulation: The thermal dynamics implemented in the simulation are time scaled-down by reducing the value of thermal capacitances in a 1:100 proportion, as experiments typically operate on the order of hours. Furthermore, the control is verified with a simulation of the thermal model decoupled from the electrical dynamics to reduce the simulation time and obtain results on the same time scale as the experiments.

In conclusion, while this study contributes valuable insights into the application of DC-DC GaN-based Converters with CCS-MPC control under specific conditions, it is essential to acknowledge the delineated limitations when interpreting the results and considering potential applications in broader contexts.

1.6 Chapter Summary

This document is divided into six chapters and two appendices.

- **Chapter 1**: Introduction to the research topic, including a review of the state of the art, establishment of thesis contributions, and an outline of the general chapter structure.
- **Chapter 2**: Presentation of the dynamical modeling of DC-DC GaN-based Converters, considering the interaction between thermal and electrical models.
- **Chapter 3**: Introduction of concepts related to Model Predictive Control (MPC) and Active Thermal Control, along with the proposal of a control strategy based on Karush-Kuhn-Tucker (KKT) conditions.
- **Chapter 4**: Presentation of simulation results, validating the proposed control strategy and comparing it with a classical Proportional-Integral (PI) controller.
- **Chapter 5**: Presentation of experimental results controlling current and temperature, validating the hypotheses.
- **Chapter 6**: The conclusions and comments from this research are included.
- **Appendix A**: Contains a list of codes used in this research.
- **Appendix B**: Contains a list of publications derived from this research.

Chapter 2

MODELING OF GAN-BASED DC-DC CONVERTERS

2.1 Introduction

THE unwavering commitment to enhancing power electronics efficiency has propelled Gallium Nitride (GaN) into a fundamental role as a semiconductor material, fundamentally reshaping the landscape of DC-DC converters. This chapter delves into the intricate task of modeling GaN-based DC-DC converters, with a specific focus on their application in EV systems.

GaN semiconductors, exemplified by devices like the GaN E-HEMT GS66516 from GaN Systems [25], present a paradigm shift in converter design due to their exceptional performance characteristics. This chapter aims to provide a comprehensive understanding of the complexities of modeling associated with these converters, elucidating the electrical and thermal aspects crucial for their accurate representation in simulation environments.

The exploration begins with an in-depth examination of the fundamental principles underlying GaN-based DC-DC converters. Through a meticulous description of the components and their interactions, a solid foundation for the subsequent modeling endeavors is established in this work. The incorporation of thermal dynamics, mirroring real-world conditions, becomes a crucial aspect, warranting a detailed analysis of the semiconductor losses using the GaN E-HEMT GS66516 model.

This chapter not only serves as a theoretical exposition but also lays the groundwork for subsequent chapters, where these models will be applied and validated through simulations and experimental trials. Navigating through the intricacies of GaN-based DC-DC converter modeling aims to unravel insights that contribute to the broader discourse on advanced power electronic systems, especially within the context of electric vehicles and sustainable energy solutions.

2.2 Modeling in state variables for converters

In the field of power electronics, the inherent nonlinearity of converters arises from the amalgamation of switched discrete actuations with continuous variables, such as voltage and currents. This nonlinearity is mathematically encapsulated in the state-space representation:

$$\frac{d}{dt}x = f(x,u) \qquad\qquad y = g(x,u) \tag{2.1}$$

Furthermore, the general expression for power converters can be characterized by bilinear models:

$$\frac{d}{dt}x = \mathbf{A}(u)x + \mathbf{B}u + \mathbf{E} \qquad\qquad y = \mathbf{C}x + \mathbf{D}u + \mathbf{F} \tag{2.2}$$

Here, the state matrix $\mathbf{A}(u)$ is contingent upon I control inputs, defined as:

$$\mathbf{A}(u) = \mathbf{A}_0 + \sum_{i=1}^{I} \mathbf{A}_i u_i. \tag{2.3}$$

To facilitate the use of linear controllers, such as proportional-integral controllers (PI), a crucial step involves linearization to compute fundamental transfer functions for PI controller design. Through linearization, the nonlinear state-space equation (2.1) transforms into a linear system:

$$\frac{d}{dt}x = \mathbf{A}x + \mathbf{B}u + \mathbf{E} \qquad\qquad y = \mathbf{C}x + \mathbf{D}u + \mathbf{F} \tag{2.4}$$

In the computation of the matrices **A**, **B**, **C**, **D**, **E**, and **F**, their values are determined within an equilibrium point as follows:

$$\begin{aligned}
\mathbf{A} &= \frac{\partial f}{\partial x}\bigg|(x_Q,u_Q), \qquad \mathbf{B} = \frac{\partial f}{\partial u}\bigg|(x_Q,u_Q), \quad \mathbf{E} = f(x_Q,u_Q) - x_Q\frac{\partial f}{\partial x}\bigg|(x_Q,u_Q) - u_Q\frac{\partial f}{\partial u}\bigg|(x_Q,u_Q)\\
\mathbf{C} &= \frac{\partial g}{\partial x}\bigg|(x_Q,u_Q), \qquad \mathbf{D} = \frac{\partial g}{\partial u}\bigg|(x_Q,u_Q), \quad \mathbf{F} = g(x_Q,u_Q) - x_Q\frac{\partial g}{\partial x}\bigg|(x_Q,u_Q) - u_Q\frac{\partial g}{\partial u}\bigg|(x_Q,u_Q)
\end{aligned} \tag{2.5}$$

Moreover, the fundamental transfer functions are computed as:

$$G(s) = \mathbf{C}(s\mathbf{I} - \mathbf{A})^{-1}\mathbf{B} + \mathbf{D} \tag{2.6}$$

This chapter embarks on the task of extending these fundamental principles to the modeling domain of GaN-based DC-DC converters, offering a crucial foundation for subsequent analyses and design considerations.

2.3 Description of the GaN semiconductor model and principle of operation

Due to the physical construction of the semiconductors, a conduction characteristic is generated that depends on the activation through the gate source voltage. In Fig. 1.10 it is observed that there are 3 conduction mode zones. In zones A and B, a fairly linear relationship is observed for a wide current range between I_{ds} and V_{ds} that can be modeled as a conduction resistance $R_{DS(on)}$. However, this relationship also depends on the junction temperature T_j. According to the GaN GS66516B datasheet this relationship is quadratic between $R_{DS(on)}$ and T_j. Hence, the resistance can be approximated as follows

$$R_{DS(on)}(T_j) = R_{DS(on)}^{25^\circ C} \ (aT_j^2 + bT_j + c) \tag{2.7}$$

where the parameters $R_{DS(on)}^{25^\circ C}$, a, b, and c are shown in Table 2.1. Considering the conduction resistance in GaN-based DC-DC converters in the electrical model is an interesting modeling approach due to its direct relationship between the input and output voltages, which change significantly for small duty cycles, leading to small $R_{DS(on)}$ variations. This issue is more relevant in boost operation cases, as will be explained in the electrical model of the Two-Level Boost Converter.

Table 2.1: Parameters of $R_{DS(on)}(T_j)$ of GS66516B GaN device [25]

Parameter	Value
On resistor, $R_{DS(on)}^{25^\circ C}$	$25m\Omega$
Constant, a	$2.76 \cdot 10^{-5}\ ^\circ C^{-2}$
Constant, b	$7.81 \cdot 10^{-3}\ ^\circ C^{-1}$
Constant, c	$7.693 \cdot 10^{-1}$

According to Fig. 1.10, the GaN device can be modeled as a switch that, when turned on by the gate-source voltage V_{GS}, is a conduction resistance, and when turned off, is a diode with some conduction resistance. This electrical model can be seen in Fig. 2.1.

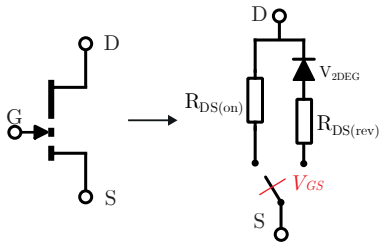

Figure 2.1: Electrical model of GaN.

To simplify modeling the switching behavior of GaN, it can be assumed that the reverse conduction resistance is zero and that only the diode operates by blocking a certain constant voltage V_D when the current I_{DS} is in the correct direction.

2.4 Electrical models of DC-DC converters

In this section, two DC-DC converters used in a powertrain system shown in Fig. 1.3 are analyzed. The Two-Level Boost Converter is used to boost the voltage of a battery v_b and set the DC-Link voltage v_{dc} that powers the DC-AC converters that control the vehicle's electric motors, and the Two-Level Buck Converter is used to charge low-voltage batteries..

2.4.1 Two Level Boost Converter

The Two Level Boost Converter is analyzed only dynamically. The topology under study is depicted in Fig. 2.2(a), and its commutation states are depicted in Fig. 2.2(b,c).

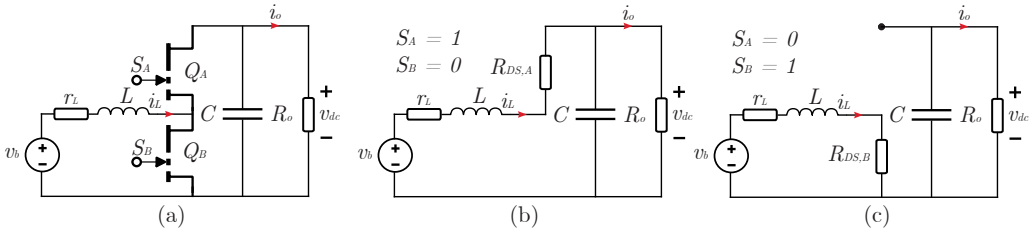

Figure 2.2: Two Level Boost Converter (a) Topology and (b,c) conmutation states.

The input control signals of the converter are S_A and S_B, and the conduction resistances $R_{DS,A}$ and $R_{DS,B}$ of devices Q_A and Q_B respectively are also considered, and r_L takes into account the parasitic resistance of the inductor and cable.

The converter must avoid a short circuit between semiconductors and DC-Link voltage, so the state $S_A = S_B = 1$ is forbidden, and the state $S_A = S_B = 0$ is used when dead time is implemented; therefore, if the dead time is short enough, this state can be neglected for dynamical analysis. Then, S_B can be considered as the complementary signal of S_A, such that $S = S_A = \overline{S}_B$, and the equations for every state are given in Eq. (2.8).

$$\begin{aligned} &S = 1 && S = 0 \\ &v_b = (R_{DS,A} + r_L)i_L + L\frac{d}{dt}i_L + v_{dc} && v_b = (R_{DS,B} + r_L)i_L + L\frac{d}{dt}i_L \\ &i_L = C\frac{d}{dt}v_{dc} + \frac{v_{dc}}{R_o} && 0 = C\frac{d}{dt}v_{dc} + \frac{v_{dc}}{R_o} \end{aligned} \tag{2.8}$$

Combining the equations of each state into a single equation, the following equations are obtained as the commuted model in Eq. (2.9).

$$v_b = (S \cdot R_{DS,A} + (1 - S) \cdot R_{DS,B} + r_L)i_L + L\frac{d}{dt}i_L + S \cdot v_{dc} \tag{2.9a}$$

$$S \cdot i_L = C\frac{d}{dt}v_{dc} + \frac{v_{dc}}{R_o} \tag{2.9b}$$

Then, assuming that the switching signal S generated by PWM, inductor current i_L, and DC-Link voltage v_{dc} can be approximated with their average values known as duty cycle d, I_L, and V_{dc}

respectively, the following continuous averaging model is obtained in Eq. (2.10).

$$\frac{d}{dt}I_L = -\frac{R_{DS,B}+r_L}{L}I_L + \frac{R_{DS,B}-R_{DS,A}}{L}I_L d - \frac{1}{L}V_{dc}d + \frac{V_b}{L} \tag{2.10a}$$

$$\frac{d}{dt}V_{dc} = \frac{1}{C}I_L d - \frac{1}{R_o C}V_{dc} \tag{2.10b}$$

Which is a bilinear model since the duty cycle d, the actuation, is multiplied by inductor current I_L and DC-Link voltage V_{dc}, state variables. From this notation, it can be seen that $\mathbf{A}(d) = \mathbf{A}_0 + \mathbf{A}_1 d$, and $\mathbf{B} = 0$.

$$\frac{d}{dt}\begin{bmatrix} I_L \\ V_{dc} \end{bmatrix} = \left(\begin{bmatrix} -\frac{R_{DS,B}+r_L}{L} & 0 \\ 0 & -\frac{1}{R_o C} \end{bmatrix} + \begin{bmatrix} \frac{R_{DS,B}-R_{DS,A}}{L} & -\frac{1}{L} \\ \frac{1}{C} & 0 \end{bmatrix} d \right) \begin{bmatrix} I_L \\ V_{dc} \end{bmatrix} + \begin{bmatrix} \frac{V_b}{L} \\ 0 \end{bmatrix} \tag{2.11}$$

Unlike the Two Level Buck Converter, as will be explained, in this model, it is not enough to assume that the conduction resistances are 0 or that they are equal to obtain a linear model. To carry out a linear control design, the model must be linearized at an operating point such that:

$$I_{L,Q} = \frac{V_{dc,Q}}{d_Q R_o} \qquad V_{dc,Q} = \frac{d_Q R_o}{d_Q^2 R_o + d_Q(R_{DS,A} - R_{DS,B}) + R_{DS,B} + r_L}V_b \tag{2.12}$$

The ideal system where $r_L = R_{DS,A} = R_{DS,B} = 0\Omega$ the equilibrium point is:

$$I_{L,Q} = \frac{V_b}{d_Q^2 R_o} \qquad V_{dc,Q} = \frac{1}{d_Q}V_b \tag{2.13}$$

Fig. 2.3 shows the comparison of the ideal and real expected boost voltage and current curves in a equilibrium point.

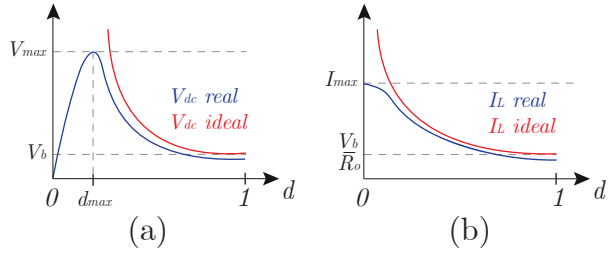

Figure 2.3: Comparison of steady state curves of boost converter considering ideal and real parameters (a) DC-Link voltage V_{dc} and (b) inductor current I_L.

Where the maximum voltage V_{max} and its duty cycle d_{max} are obtained in Eq. (2.14) by equating the derivative of $V_{dc,Q}$ to zero and substituting.

$$d_{max} = \sqrt{\frac{R_{DS,B}+r_L}{R_o}} \qquad V_{max} = \frac{d_{max}R_o}{2R_{DS,B} + r_L + (R_{DS,A} - R_{DS,B})d_{max}}V_b \tag{2.14}$$

The linearizated system in the equilibrium point can be written such that:

$$\frac{d}{dt}\Delta I_L = K_{I1}\Delta I_L + K_{V1}\Delta V_{dc} + K_{d1}\Delta d \tag{2.15a}$$

$$\frac{d}{dt}\Delta V_{dc} = K_{I2}\Delta I_L + K_{V2}\Delta V_{dc} + K_{d2}\Delta d \tag{2.15b}$$

Where the constants are:

$$\begin{aligned} K_{I1} &= -\frac{R_{DS,B} + r_L - (R_{DS,B} - R_{DS,A})d_Q}{L} & K_{V1} &= -\frac{d_Q}{L} & K_{d1} &= -\frac{V_{dc,Q}}{L} \\ K_{I2} &= \frac{d_Q}{C} & K_{V2} &= -\frac{1}{R_o C} & K_{d2} &= \frac{I_{L,Q}}{C} \end{aligned} \tag{2.16}$$

And the linear model in matrix form:

$$\frac{d}{dt}\begin{bmatrix}\Delta I_L \\ \Delta V_{dc}\end{bmatrix} = \begin{bmatrix}K_{I1} & K_{V1} \\ K_{I2} & K_{V2}\end{bmatrix}\begin{bmatrix}\Delta I_L \\ \Delta V_{dc}\end{bmatrix} + \begin{bmatrix}K_{d1} \\ K_{d2}\end{bmatrix}\Delta d \tag{2.17}$$

To obtain a model for linear control the fundamental transfer functions are computed such that $G_v(d)$ and $G_i(s)$ from Eq. (2.18) are the transfer functions for voltage and current respect to duty cycle.

$$G_v(s) = \frac{\Delta\hat{V}_{dc}}{\Delta\hat{d}} = \frac{K_{d2}s + K_{d1}K_{I2} - K_{d2}K_{I1}}{s^2 - s(K_{I1} + K_{V2}) + K_{I1}K_{V2} - K_{I2}K_{V1}} = -K_V\frac{\omega_n^2}{s_v}\frac{s - s_v}{s^2 + 2\omega_n\xi s + \omega_n^2} \tag{2.18a}$$

$$G_i(s) = \frac{\Delta\hat{I}_L}{\Delta\hat{d}} = \frac{K_{d1}s + K_{d2}K_{V1} - K_{d1}K_{V2}}{s^2 - s(K_{I1} + K_{V2}) + K_{I1}K_{V2} - K_{I2}K_{V1}} = -K_I\frac{\omega_n^2}{s_i}\frac{s - s_i}{s^2 + 2\omega_n\xi s + \omega_n^2} \tag{2.18b}$$

Where,

$$s_v = \frac{K_{d2}K_{I1} - K_{d1}K_{I2}}{K_{d2}} = \frac{d_Q V_{dc,Q}}{I_{L,Q}L} - \frac{R_{DS,B} + r_L - d_Q(R_{DS,B} - R_{DS,A})}{L} \tag{2.19a}$$

$$s_i = \frac{K_{d1}K_{V2} - K_{d2}K_{V1}}{K_{d1}} = -\frac{d_Q I_{L,Q}R_o + V_{dc,Q}}{R_o C V_{dc,Q}} \tag{2.19b}$$

$$K_V = \frac{K_{d1}K_{I2} - K_{d2}K_{I1}}{K_{I1}K_{V2} - K_{I2}K_{V1}} = -R_o\frac{V_{dc,Q}d_Q - (R_{DS,B} + r_L - d_Q(R_{DS,B} - R_{DS,A}))I_{L,Q}}{d_Q^2 R_o + R_{DS,B} + r_L - d_Q(R_{DS,B} - R_{DS,A})} \tag{2.19c}$$

$$K_I = \frac{K_{d2}K_{V1} - K_{d1}K_{V2}}{K_{I1}K_{V2} - K_{I2}K_{V1}} = -\frac{V_{dc,Q} + R_o I_{L,Q}d_Q}{d_Q^2 R_o + R_{DS,B} + r_L - d_Q(R_{DS,B} - R_{DS,A})} \tag{2.19d}$$

$$\omega_n = \sqrt{K_{I1}K_{V2} - K_{I2}K_{V1}} = \frac{d_Q}{\sqrt{LC}}\cdot\sqrt{1 + \frac{R_{DS,B} + r_L - d_Q(R_{DS,B} - R_{DS,A})}{d_Q^2 R_o}} \tag{2.19e}$$

$$\xi = -\frac{K_{I1} + K_{V2}}{2\sqrt{K_{I1}K_{V2} - K_{I2}K_{V1}}} = \frac{1}{2\sqrt{R_o LC}}\cdot\frac{L + R_o C(R_{DS,B} + r_L - d_Q(R_{DS,B} - R_{DS,A}))}{\sqrt{d_Q^2 R_o + R_{DS,B} + r_L - d_Q(R_{DS,B} - R_{DS,A})}} \tag{2.19f}$$

Both transfer functions are second order and have a zero. In Eq. (2.19)(a,b) it can be seen that the zero s_v is positive in general if $I_{L,Q} > 0$ which is a non-minimum phase zero, while s_i can

be a non-minimum phase zero in regeneration where $I_{L,Q} < 0$ and $R_o < 0$. In Eq. (2.19)(c,d), it is observed that the gains K_V and K_I are in general negative. This phenomenon arises due to the inverse relationship between the duty cycle d and both the DC-Link voltage V_o and inductor current $I_{L,Q}$ in steady state, as illustrated in Fig. 2.3. Eq. (2.19)e reveals that the natural resonance frequency ω_n increases with higher conduction resistances $R_{DS,A}$ and $R_{DS,B}$, as well as with the parasitic resistance r_L. Lastly, Eq. (2.19)f provides insight into the damping coefficient ξ, indicating that greater conduction and parasitic resistances result in increased damping. Conversely, as the load resistance R_o approaches infinity, implying negligible load, the damping tends toward zero.

Controlling a system with non-minimum phase zeros poses significant challenges. Non-minimum phase systems exhibit zeros with positive real parts, leading to inherent instability and difficulties in achieving desired performance metrics. The presence of non-minimum phase zeros results in high-frequency resonance and limits the achievable bandwidth of the closed-loop system [85]. Consequently, control efforts must contend with delayed and anticipatory behaviors, making it more challenging to stabilize the system and meet performance specifications. Addressing non-minimum phase characteristics requires advanced control strategies and careful consideration of system dynamics to mitigate instability and ensure effective control.

2.4.2 Two Level Buck Converter

The Two-Level Buck Converter (TLBC) is analyzed both dynamically and in steady state. The topology under study is depicted in Fig. 2.4(a), and its commutation states are depicted in Fig. 2.4(b,c,d).

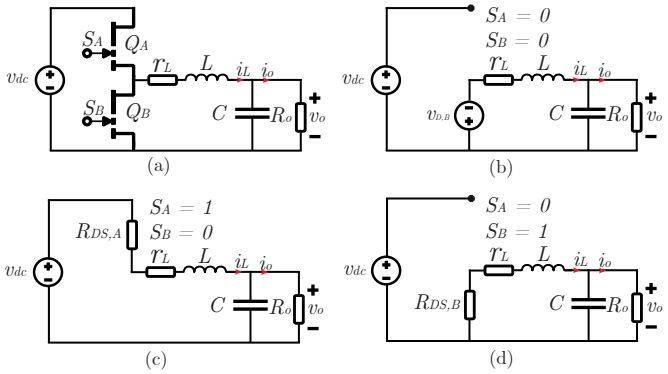

Figure 2.4: Two Level Buck Converter (a) Topology and (b,c,d) conmutation states with powerflow to load.

2.4.2.1 Dynamical analysis with average values

The control input of the TLBC is typically the duty cycle d of S_A. It's worth noting that conduction resistances $R_{DS,A}$ and $R_{DS,B}$ are considered for each semiconductor device Q_A and Q_B, respectively, and r_L takes into account the parasitic resistance of the inductor and cable.

Since the converter must avoid a short circuit between semiconductors, the state $S_A = S_B = 1$ is forbidden. The state $S_A = S_B = 0$ is used when dead time is implemented; therefore, if the dead time is short enough, this state can be neglected for dynamical analysis. Then, S_B can be

considered as the complementary signal of S_A, such that $S = S_A = \overline{S}_B$, and the equations for every state are given in Eq. (2.20).

$$\begin{aligned} &S = 1 && S = 0 \\ &v_{dc} = (R_{DS,A} + r_L)i_L + L\frac{d}{dt}i_L + v_o && 0 = (R_{DS,B} + r_L)i_L + L\frac{d}{dt}i_L + v_o \\ &i_L = C\frac{d}{dt}v_o + \frac{v_o}{R_o} && i_L = C\frac{d}{dt}v_o + \frac{v_o}{R_o} \end{aligned} \tag{2.20}$$

Combining the equations of each state into a single equation, the following equations are obtained as the commuted model in Eq. (2.21).

$$S \cdot v_{dc} = (S \cdot R_{DS,A} + (1 - S) \cdot R_{DS,B} + r_L)i_L + L\frac{d}{dt}i_L + v_o \tag{2.21a}$$

$$i_L = C\frac{d}{dt}v_o + \frac{v_o}{R_o} \tag{2.21b}$$

Then, assuming that the switching signal S generated by PWM, inductor current i_L, and output voltage v_o can be approximated with their average values known as duty cycle d, I_L, and V_o respectively, the following continuous averaging model is obtained in Eq. (2.22).

$$\frac{dI_L}{dt} = -\frac{R_{DS,B} + r_L}{L}I_L - \frac{1}{L}V_o + \frac{R_{DS,B} - R_{DS,A}}{L}I_L d + \frac{V_{dc}}{L}d \tag{2.22a}$$

$$\frac{dV_o}{dt} = \frac{1}{C}I_L - \frac{1}{R_o C}V_o \tag{2.22b}$$

which is a bilinear model since the duty cycle d, the actuation, is multiplied by inductor current I_L, one state variable. From this notation, it can be seen that $\mathbf{A}(d) = \mathbf{A}_0 + \mathbf{A}_1 d$, and $\mathbf{E} = 0$.

$$\frac{d}{dt}\begin{bmatrix} I_L \\ V_o \end{bmatrix} = \left(\begin{bmatrix} -\frac{R_{DS,B}+r_L}{L} & -\frac{1}{L} \\ \frac{1}{C} & -\frac{1}{R_o C} \end{bmatrix} + \begin{bmatrix} \frac{R_{DS,B}-R_{DS,A}}{L} & 0 \\ 0 & 0 \end{bmatrix} d \right) \begin{bmatrix} I_L \\ V_o \end{bmatrix} + \begin{bmatrix} \frac{V_{dc}}{L} \\ 0 \end{bmatrix} d \tag{2.23}$$

Then, using Forward Euler discretization, the continuous model is transformed into a discrete-time model in Eq. (2.24). Here, the model also considers the implementation delay of one sample due to the implementation of PWM.

$$i_L(k+2) = (a_1 + a_3 d(k))i_L(k+1) + a_2 v_o(k+1) + a_4 d(k) \tag{2.24a}$$

$$v_o(k+2) = a_5 i_L(k+1) + a_6 v_o(k+1) \tag{2.24b}$$

with the sampling time $T_{s,i}$ and coefficients shown in Eq. (2.25).

$$\begin{aligned} &a_1 = 1 + a_2(R_{DS,B} + r_L) && a_3 = a_2(R_{DS,A} - R_{DS,B}) && a_5 = \frac{T_{s,i}}{C} \\ &a_2 = -\frac{T_{s,i}}{L} && a_4 = -a_2 V_{dc} && a_6 = 1 - \frac{a_5}{R_o} \end{aligned} \tag{2.25}$$

When discretizing a bilinear system (2.22a)-(2.22b) with the Euler method, the discrete model remains in a bilinear form, as observed in equation (2.24a)-(2.24b).

$$\begin{bmatrix} i_L(k+2) \\ v_o(k+2) \end{bmatrix} = \left(\begin{bmatrix} a_1 & a_2 \\ a_5 & a_6 \end{bmatrix} + \begin{bmatrix} a_3 & 0 \\ 0 & 0 \end{bmatrix} d(k) \right) \begin{bmatrix} i_L(k+1) \\ v_o(k+1) \end{bmatrix} + \begin{bmatrix} a_4 \\ 0 \end{bmatrix} d(k) \tag{2.26}$$

In this case, the converter is simple enough for its bilinear form to be approximated by its linear form since the conduction resistances of the semiconductors $R_{DS,A}$ and $R_{DS,B}$ can be neglected or assumed to be equal, and therefore $a_3 = 0$.

Additionally, it should be taken into account that in real applications, the load is not a resistor R_o but rather the output or load current i_o varies depending on the power required by the system.

2.4.2.2 Waveform analysis in steady state considering dead-time

Waveform steady state analysis is carried to consider the impact of dead-time t_d assuming constant DC-Link and output voltages V_{dc} and V_o such that the average of inductor current is I_L and it is always positive due to powerflow is to load. Also it assumed a fixed switching period $T_{sw} = 1/f_{sw}$. The expected waveform is shown in Fig. 2.5 along with all variables to be used. It can be seen that d is the duty cycle of S. However, with dead time the real duty cycle d_{real} applied with S_A is $d - t_d f_{sw}$. Therefore, the stationary relationship between output voltage and duty cycle is:

$$V_o = d_{real} V_{dc} = (d - t_d f_{sw}) V_{dc} \tag{2.27}$$

Then with LVK and LCK equations in GaN devices it is analyzed the distribution of voltage and current during the conmutation states such that (2.28) are always fullfield.

$$V_{dc} = v_{DS,A} + v_{DS,B} \qquad\qquad i_{DS,A} = i_L + i_{DS,B} \tag{2.28}$$

Where from (1.10) the currents and voltages of GaN devices behavior respect to inductor current i_L, gate signals S_A and S_B are shown in Tab. 2.2 for TLBC.

Table 2.2: Conduction modes bidirectional Two Level Buck Converter GaN based

S_A	S_B	$i_L > 0$	$i_L < 0$	$i_{DS,A}$	$i_{DS,B}$	$v_{DS,A}$	$v_{DS,B}$	$p_{DS,A}$	$p_{DS,B}$
0	0	0	1	i_L	0	$-v_D$	$V_{dc} + v_D$	$-v_D i_L$	0
0	0	1	0	0	$-i_L$	$V_{dc} + v_D$	$-v_D$	0	$v_D\ i_L$
0	1	0	1	0	i_L	$V_{dc} - R_{DS,B}\ i_L$	$R_{DS,B}\ i_L$	0	$R_{DS,B}\ i_L^2$
0	1	1	0	0	i_L	$V_{dc} - R_{DS,B}\ i_L$	$R_{DS,B}\ i_L$	0	$R_{DS,B}\ i_L^2$
1	0	0	1	i_L	0	$R_{DS,A}\ i_L$	$V_{dc} - R_{DS,A}\ i_L$	$R_{DS,A}\ i_L^2$	0
1	0	1	0	i_L	0	$R_{DS,A}\ i_L$	$V_{dc} - R_{DS,A}\ i_L$	$R_{DS,A}\ i_L^2$	0

In order to illustrate the steady state waveforms as accurately as possible, the Ordinary Differential Equation (ODE) of the inductor current must be analyzed. In general the inductor current has a standard ODE such that:

$$L\frac{di_L}{dt} + Ri_L = V \tag{2.29}$$

And the general solution for a initial condition in $t = t_0$ is:

$$i_L(t) = i_L(t_0)\exp\left(-\frac{R}{L}(t-t_0)\right) + \frac{V}{R}\left(1-\exp\left(-\frac{R}{L}(t-t_0)\right)\right) \tag{2.30}$$

Considering the aproximation of exponential:

$$\exp(x) = 1 + x + \frac{x^2}{2!} + \frac{x^3}{3!} + \ldots \approx 1 + x \ , \ x \approx 0 \tag{2.31}$$

The solution can also be approximated, resulting in:

$$i_L(t) \approx \frac{V - Ri_L(t_0)}{L}(t-t_0) + i_L(t_0) \tag{2.32}$$

Time analysis is made assuming that inductor current is in steady state and therefore is periodic with fundamental frequency f_{sw} such that in an interval $[0, T_{sw}]$ the inductor current $i_L(t)$ is continuous and $i_L(0) = i_L(T_{sw})$. Considering the conmutation modes of Tab. 2.2 the inductor current is described as a Piecewise function such that

$$i_L(t) = \begin{cases} i_{L1}(t) & , \ t \in (0, t_1) \\ i_{L2}(t) & , \ t \in (t_1, t_2) \\ i_{L3}(t) & , \ t \in (t_2, t_3) \\ i_{L4}(t) & , \ t \in (t_3, T_{sw}) \end{cases} \tag{2.33}$$

Where instant time definitions are:

$$t_1 = d\ T_{sw} - t_d \qquad t_2 = d\ T_{sw} \qquad t_3 = T_{sw} - t_d \tag{2.34}$$

In each time interval it is considered the respectively ODE to express the behavior of inductor current and their extrem values.

- $t \in (0, t_1)$ with $S_A = 1$ and $S_B = 0$ where $i_L(0) = I_1$

$$L\frac{d}{dt}i_{L1} + (R_{DS,A} + r_L)i_{L1} = V_{dc} - V_o \tag{2.35}$$

$$i_{L1}(t) = I_1 \cdot \exp\left(-\frac{R_{DS,A} + r_L}{L}t\right) + \frac{V_{dc} - V_o}{R_{DS,A} + r_L}\left(1 - \exp\left(-\frac{R_{DS,A} + r_L}{L}t\right)\right) \tag{2.36}$$

$$i_{L1}(t) \approx \frac{V_{dc} - V_o - (R_{DS,A} + r_L)I_1}{L}t + I_1 \tag{2.37}$$

$$I_2 = I_1 \cdot \exp\left(-\frac{R_{DS,A} + r_L}{L}t_1\right) + \frac{V_{dc} - V_o}{R_{DS,A} + r_L}\left(1 - \exp\left(-\frac{R_{DS,A} + r_L}{L}t_1\right)\right) \tag{2.38}$$

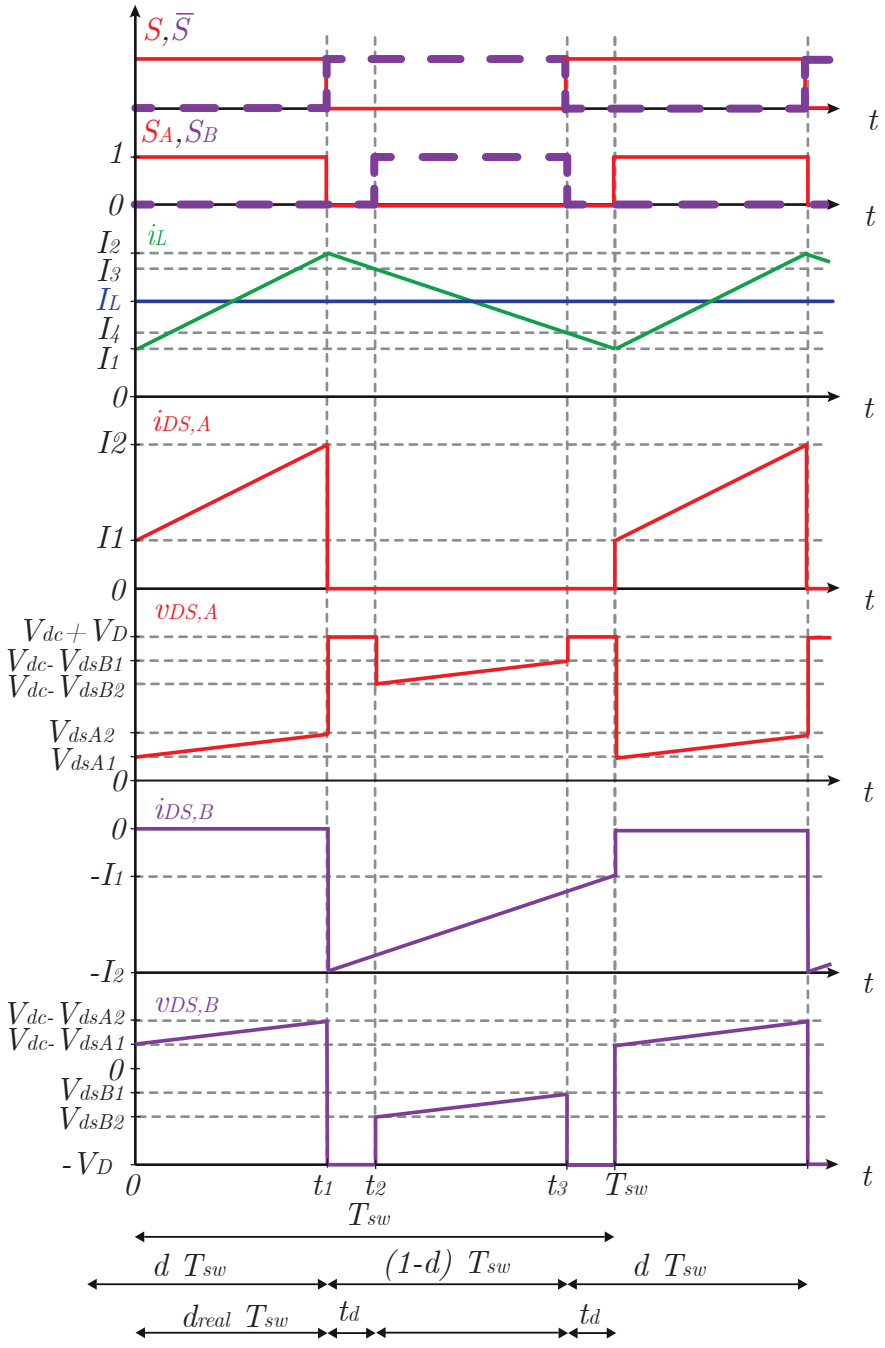

Figure 2.5: Waveform signals of TLBC in steady state with powerflow to load.

- $t \in (t_1, t_2)$ with $S_A = 0$ and $S_B = 0$ where $i_L(t_1) = I_2$

$$L\frac{d}{dt}i_{L2} + r_L i_{L2} = -V_D - V_o \tag{2.39}$$

$$i_{L2}(t) = I_2 \cdot \exp\left(-\frac{r_L}{L}(t-t_1)\right) - \frac{V_D + V_o}{r_L}\left(1 - \exp\left(-\frac{r_L}{L}(t-t_1)\right)\right) \tag{2.40}$$

$$i_{L2}(t) \approx -\frac{V_D + V_o + r_L I_2}{L}(t-t_1) + I_2 \tag{2.41}$$

$$I_3 = I_2 \cdot \exp\left(-\frac{r_L}{L}(t_2-t_1)\right) - \frac{V_D + V_o}{r_L}\left(1 - \exp\left(-\frac{r_L}{L}(t_2-t_1)\right)\right) \tag{2.42}$$

- $t \in (t_2, t_3)$ with $S_A = 0$ and $S_B = 1$ where $i_L(t_2) = I_3$

$$L\frac{d}{dt}i_{L3} + (R_{DS,B} + r_L)i_{L3} = -V_o \tag{2.43}$$

$$i_{L3}(t) = I_3 \cdot \exp\left(-\frac{R_{DS,B}+r_L}{L}(t-t_2)\right) - \frac{V_o}{R_{DS,B}+r_L}\left(1 - \exp\left(-\frac{R_{DS,B}+r_L}{L}(t-t_2)\right)\right) \tag{2.44}$$

$$i_{L3}(t) \approx -\frac{V_o + (R_{DS,B}+r_L)I_3}{L}(t-t_2) + I_3 \tag{2.45}$$

$$I_4 = I_3 \cdot \exp\left(-\frac{R_{DS,B}+r_L}{L}(t_3-t_2)\right) - \frac{V_o}{R_{DS,B}+r_L}\left(1 - \exp\left(-\frac{R_{DS,B}+r_L}{L}(t_3-t_2)\right)\right) \tag{2.46}$$

- $t \in (t_3, T_{sw})$ with $S_A = 0$ and $S_B = 0$ where $i_L(t_3) = I_4$

$$L\frac{d}{dt}i_{L4} + r_L i_{L4} = -V_D - V_o \tag{2.47}$$

$$i_{L4}(t) = I_4 \cdot \exp\left(-\frac{r_L}{L}(t-t_3)\right) - \frac{V_D + V_o}{r_L}\left(1 - \exp\left(-\frac{r_L}{L}(t-t_3)\right)\right) \tag{2.48}$$

$$i_{L4}(t) \approx -\frac{V_D + V_o + r_L I_4}{L}(t-t_3) + I_4 \tag{2.49}$$

$$I_1 = I_4 \cdot \exp\left(-\frac{r_L}{L}(T_{sw}-t_3)\right) - \frac{V_D + V_o}{r_L}\left(1 - \exp\left(-\frac{r_L}{L}(T_{sw}-t_3)\right)\right) \tag{2.50}$$

The ripple or amplitude of i_L is defined as ΔI, and to obtain the exact value, the following system of equations must be solved:

$$I_2 = a_1 I_1 + b_1(1-a_1) \tag{2.51}$$

$$I_3 = a_2 I_2 + b_2(1-a_2) \tag{2.52}$$

$$I_4 = a_3 I_3 + b_3(1-a_3) \tag{2.53}$$

$$I_1 = a_2 I_4 + b_2(1-a_2) \tag{2.54}$$

$$\Delta I = I_2 - I_1 \tag{2.55}$$

Solving

$$\Delta I = \frac{(1-a_1)((1-a_2^2a_3)c_1-(1-a_2)(1+a_2a_3)c_2-a_2(1-a_3)c_3)}{1-a_1a_2^2a_3} \tag{2.56}$$

Where from (2.34), (2.38), (2.42), (2.46) and (2.50) the constants can be reduce to

$$\begin{aligned} a_1 &= \exp\left(-\frac{R_{DS,A}+r_L}{L}(dT_{sw}-t_d)\right) & b_1 &= \frac{V_{dc}-V_o}{R_{DS,A}+r_L} \\ a_2 &= \exp\left(-\frac{r_L}{L}t_d\right) & b_2 &= -\frac{V_D+V_o}{r_L} \\ a_3 &= \exp\left(-\frac{R_{DS,B}+r_L}{L}((1-d)T_{sw}-t_d)\right) & b_3 &= -\frac{V_o}{R_{DS,B}+r_L} \end{aligned} \tag{2.57}$$

When analyzing the ideal system and considering specified limits while approximating the exponential function as previously mentioned, its relationship with the switching frequency f_{sw}, defined as the reciprocal of the switching period T_{sw}, is as follows:

$$\lim_{(t_d,R_{DS,A},R_{DS,B})\to(0,0,0)} \Delta I = \frac{\left(\exp\left(r_L\frac{d}{f_{sw}L}\right)-1\right)\left(\exp\left(r_L\frac{1-d}{f_{sw}L}\right)-1\right)}{\exp\left(\frac{r_L}{f_{sw}L}\right)-1}\frac{V_{dc}}{r_L} \tag{2.58a}$$

$$\lim_{(t_d,R_{DS,A},R_{DS,B})\to(0,0,0)} \Delta I \approx \frac{(1-d)d}{f_{sw}L-r_L(1-d)d}V_{dc} \tag{2.58b}$$

Therefore, a complete consideration of steady state amplitude in inductor current is possible to calculate with Eq. (2.56). However, the analytical expression is too complex to show with direct dependence of all parameters. Althoug, it is important to note that with a high switching frequency the ripple is reduced and this allows to consider a small inductance for final design of converter.

It is also possible to estimate the power losses in the inductor P_{r_L} such that it is proportional to the square of the RMS value of i_L.

$$P_{r_L} = \frac{1}{T_{sw}}\int_0^{T_{sw}} r_L i_L(t)^2 dt = r_L\frac{1}{T_{sw}}\int_0^{T_{sw}} i_L(t)^2 dt = r_L I_{L,RMS}^2 \tag{2.59}$$

In general, to calculate the RMS value of a signal with DC and AC components, the property shown in Eq. (2.60) can be used.

$$i = I_{DC} + I_{AC} \qquad \longrightarrow \qquad I_{RMS}^2 = I_{DC}^2 + I_{AC,RMS}^2 \tag{2.60}$$

A simplification of i_L can be done, assuming it is a triangular signal with amplitude A, offset I_L, and a 50% duty cycle:

$$i_L(t) = \begin{cases} \frac{4A}{T_{sw}}t - A + I_L & ,\ t\in[0,T_{sw}/2] \\ -\frac{4A}{T_{sw}}(t-T_{sw}) - A + I_L & ,\ t\in[T_{sw}/2,T_{sw}] \end{cases} \tag{2.61}$$

The average value of i_L is I_L, and the square of the RMS value can be calculated with the integral or using Eq. (2.60), where the RMS value of a triangular waveform with a 50% duty cycle

and amplitude A is $A/\sqrt{3}$. Then:

$$I_{L,RMS}^2 = \frac{1}{T_{sw}} \int_0^{T_{sw}} i(t)^2 dt = I_L^2 + \frac{A^2}{3} \tag{2.62}$$

The power losses in the inductor P_{r_L} for this case are given by:

$$P_{r_L} = r_L \left(I_L^2 + \frac{A^2}{3} \right) \tag{2.63}$$

Therefore, as seen in Eq. (2.58), the amplitude or ripple ΔI of i_L decreases as the switching frequency f_{sw} increases, and consequently, the power losses in the inductor will also decrease till the limit:

$$\lim_{f_{sw} \to \infty} P_{r_L} = r_L I_L^2 \tag{2.64}$$

Synchronized sampling is mandatory to measure the average value of i_L, requiring a high-bandwidth current probe. Through this comprehensive analysis, it becomes apparent that the frequency of the inductor current varies. Consequently, measuring this current presents a challenge, as the current probe necessitates a sufficiently broad bandwidth to accommodate this variability across all operational switching frequencies.

2.4.2.3 Estimation of inductor current

Alternatively, an estimation of I_L using lower-frequency signals such as v_o and i_o is proposed. Moreover, in steady state, the average inductor current is equal to the load current, $I_L = I_o$. However, integrating this estimation into the control scheme poses challenges as it introduces additional dynamics that must be accounted for. The proposed estimation is based on LCK equation:

$$i_L = C \frac{dv_o}{dt} + i_o \tag{2.65}$$

To approximate the derivate of v_o Backward Euler method is proposed

$$s \approx \frac{z-1}{zT_s} \tag{2.66}$$

Then

$$\hat{i}_L = Cs\hat{v}_o + \hat{i}_o \tag{2.67}$$

$$\hat{i}_L \approx f_s C \frac{z-1}{z} \hat{v}_o + \hat{i}_o \tag{2.68}$$

$$i_L(k) \approx f_s C(v_o(k) - v_o(k-1))) + i_o(k) \tag{2.69}$$

However, this approximation is sensible to high frequency noise. Therefore, a filter with factor α is implemented such that

$$\hat{i}_{Lo} = f_s C \frac{1-\alpha}{z-\alpha} \frac{z-1}{z} \hat{v}_o + \hat{i}_o \tag{2.70}$$

$$i_{Lo}(k) = \alpha\ i_{Lo}(k-1) + (1-\alpha) f_s C(v_o(k) - v_o(k-1))) + i_o(k) - \alpha\ i_o(k-1) \tag{2.71}$$

2.5 Thermal model of GaN devices

2.5.1 Thermal parameters of GaN devices

Thermal model considers that GaN devices are connected through an Insulated Metal Substrate (IMS) board to the heatsink. IMS board is selected because its good thermal performance compared to Fibreglass resin (FR4) PCB [86] as can be seen in Tab. 2.3.

Table 2.3: Performance comparison of 3 thermal design options for SMT power devices [86].

	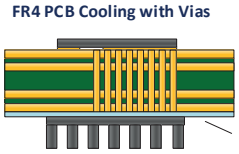	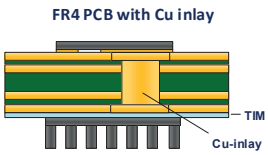	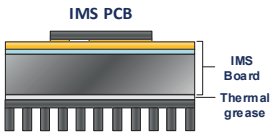
Thermal resistance	Good	Better	Best
Electrical Insulation	No, additional TIM needed	No, additional TIM needed	Yes
Cost	Lowest	High	Low
Advantages	- Standard process - Lowest cost - Layout flexibility	- Layout flexibility - Improved thermal compared to thermal vias	- Lowest thermal resistance - Electrically isolated
Design challenges	- High PCB thermal resistance	- Cu-inlay surface coplanarity - High TIM thermal resistance	- Layout limited to 1 layer - Parasitic inductance - Coupling capacitances to the metal substrate

Connection and proposed thermal model based on a Caue-type RC thermal network, including the junction-to-case RC thermal model of GaN devices, and RC thermal model of solder, IMS board, thermal grease, and heatsink is shown in Fig. 2.6. The current source P_{Loss} in the junction-to-case RC thermal model represents power losses of the GaN device, which consist of two parts: conduction losses and switching losses. In this work, P_{Loss} is obtained through simulation with a provided power loss model by GaN Systems and then adjusted by experimental measurements.

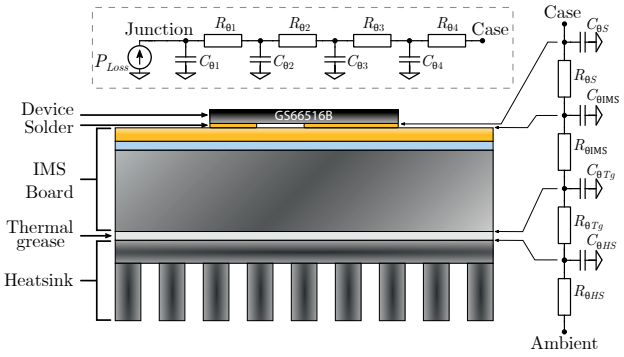

Figure 2.6: Thermal model between junction and ambient temperature [75].

Given the difficulty of measuring junction temperature, it can be estimated with a state-space model considering the temperatures of thermal capacities as state-variables, and considering as inputs the power losses P_{Loss}, and case temperature T_c. The state-space model based on thermal RC junction-to-case thermal $R_{\theta jc}$ circuit shown in Fig. 3 can be defined as:

$$\frac{dx_1}{dt} = -\frac{1}{R_{\theta 1}C_{\theta 1}}x_1 + \frac{1}{R_{\theta 1}C_{\theta 1}}x_2 + \frac{1}{C_{\theta 1}}P_{Loss} \tag{2.72a}$$

$$\frac{dx_2}{dt} = \frac{1}{R_{\theta 1}C_{\theta 2}}x_1 - \frac{R_{\theta 1}+R_{\theta 2}}{R_{\theta 1}R_{\theta 2}C_{\theta 2}}x_2 + \frac{1}{R_{\theta 2}C_{\theta 2}}x_3 \tag{2.72b}$$

$$\frac{dx_3}{dt} = \frac{1}{R_{\theta 2}C_{\theta 3}}x_2 - \frac{R_{\theta 2}+R_{\theta 3}}{R_{\theta 2}R_{\theta 3}C_{\theta 3}}x_3 + \frac{1}{R_{\theta 3}C_{\theta 3}}x_4 \tag{2.72c}$$

$$\frac{dx_4}{dt} = \frac{1}{R_{\theta 3}C_{\theta 4}}x_3 - \frac{R_{\theta 3}+R_{\theta 4}}{R_{\theta 3}R_{\theta 4}C_{\theta 4}}x_4 + \frac{1}{R_{\theta 4}C_{\theta 4}}T_c \tag{2.72d}$$

here, state variable x_1 represents junction temperature T_j. Where by datasheet the thermal parameters are shown in Tab. 2.4.

Table 2.4: Thermal parameters of Cauer model for junction to case temperature in GS66516B [25].

i	1	2	3	4
$R_{\theta i}$ $(°C/W)$	0.008	0.124	0.13	0.008
$C_{\theta i}$ $(W \cdot s/°C)$	1.48e-4	1.37e-3	12e-3	3.7e-3

If it is possible to measure the temperature of the case directly, heatsink or ambient, the estimation of the junction temperature can be carried out as:

$$T_j \approx P_{Loss}R_{jc} + T_c \approx P_{Loss}R_{jh} + T_h \approx P_{Loss}R_{ja} + T_a \tag{2.73}$$

where

$$\begin{aligned} R_{jc} &= R_{\theta 1} + R_{\theta 2} + R_{\theta 3} + R_{\theta 4} & R_{ch} &= R_{\theta IMS} + R_{\theta Tg} \\ R_{jh} &= R_{jc} + R_{ch} & R_{ja} &= R_{jh} + R_h \end{aligned} \tag{2.74}$$

In Fig. 2.7 are shown the thermal resistances per physical layers for SMT power devices [86].

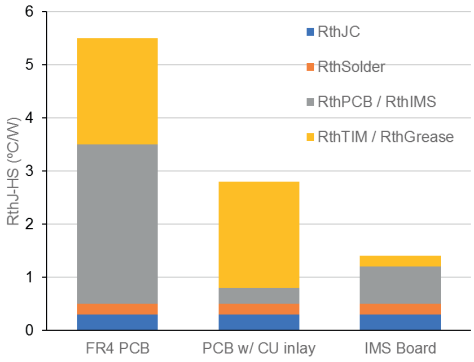

Figure 2.7: Comparison of Junction to Heatsink thermal resistance R_{thJ-HS} [86].

Therefore, using the estimations of datasheet [86] the thermal resistance between junction to case is $R_{jc} = 0.27°C/W$ and junction to heatsink is $R_{jh} = 1.4°C/W$. The thermal resistance of the heatsink R_h depends on the material and size of the heatsink used.

2.5.2 Power losses of Two-Level Buck Converter with GaN devices

In Fig. 2.8, the Cauer models are presented for a converter equipped with two GaN devices, exemplified by the Two-Level Buck Converter. In Fig. 2.8(a), it is assumed that junction temperatures are not directly measured but estimated using case temperatures. On the other hand, Fig. 2.8(b) considers that junction temperatures are approximated as equal.

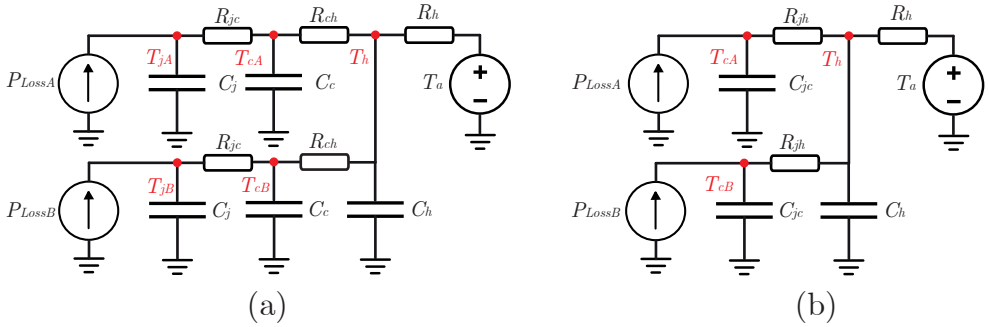

Figure 2.8: Simplified Cauer model (a) considering junction temperature different to case temperature (b) considering case temperature equal to junction temperature.

The simplified model shown in Fig. 2.8(b) can be written with three state variables resulting in Eq. (2.75). Where T_{cA}, T_{cB} and T_h are states and $P_{Loss,A}$ and $P_{Loss,B}$ are inputs.

$$\frac{d}{dt}T_{cA} = -\frac{1}{R_{jh}C_{jc}}T_{cA} + \frac{1}{R_{jh}C_{jc}}T_h + \frac{1}{C_{jc}}P_{Loss,A} \tag{2.75a}$$

$$\frac{d}{dt}T_{cB} = -\frac{1}{R_{jh}C_{jc}}T_{cB} + \frac{1}{R_{jh}C_{jc}}T_h + \frac{1}{C_{jc}}P_{Loss,B} \tag{2.75b}$$

$$\frac{d}{dt}T_h = \frac{1}{R_{jh}C_h}T_{cA} + \frac{1}{R_{jh}C_h}T_{cB} - \frac{2R_h + R_{jh}}{R_{jh}R_hC_h}T_h \tag{2.75c}$$

In steady state the relationship of temperatures with power losses are:

$$T_h = T_a + R_h(P_{Loss,A} + P_{Loss,B}) \tag{2.76}$$

$$T_{cA} = T_h + R_{jh}P_{Loss,A} = T_a + (R_{jh} + R_h)P_{Loss,A} + R_hP_{Loss,B} \tag{2.77}$$

$$T_{cB} = T_h + R_{jh}P_{Loss,B} = T_a + R_hP_{Loss,A} + (R_{jh} + R_h)P_{Loss,B} \tag{2.78}$$

It is possible to relate the thermal resistances according to the following relationship of temperatures in steady state:

$$\frac{R_h}{R_{jh}} = \frac{T_h - T_a}{T_{cA} + T_{cB} - 2T_h} \tag{2.79}$$

And to estimate the power loss in each device with the difference in semiconductor temperature with the heatsink temperature such that:

$$P_{Loss,A} = \frac{T_{cA} - T_h}{R_{jh}} \qquad P_{Loss,B} = \frac{T_{cB} - T_h}{R_{jh}} \tag{2.80}$$

The power losses $P_{Loss,A}$ and $P_{Loss,B}$ in devices Q_A and Q_B can be estimated by neglecting the losses in the activation of the device by the gate driver system and by considering the drain-source voltage and current, such that $P_{Loss,A} = v_{DS,A} \cdot i_{DS,A}$ and $P_{Loss,B} = v_{DS,B} \cdot i_{DS,B}$. In Fig. 2.9, the power loss waveform for $P_{Loss,A}$ is analyzed, taking into account the turn-on and turn-off times of the GaN devices. According to the datasheet of the GS66516B [25], these turn-on t_{on} and turn-off t_{off} times are approximately 17ns and 37ns, respectively.

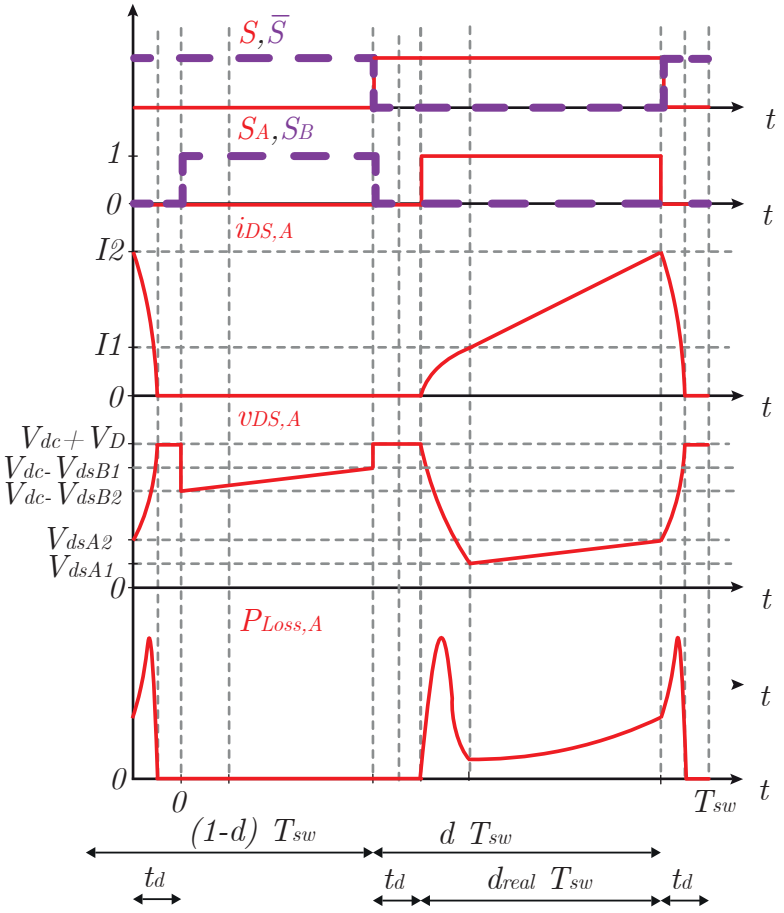

Figure 2.9: Power loss $P_{Loss,A}$ waveform signals.

In Fig. 2.10, the powe loss waveform for $P_{Loss,B}$ is analyzed, taking into account the turn-on and turn-off times of the GaN devices.

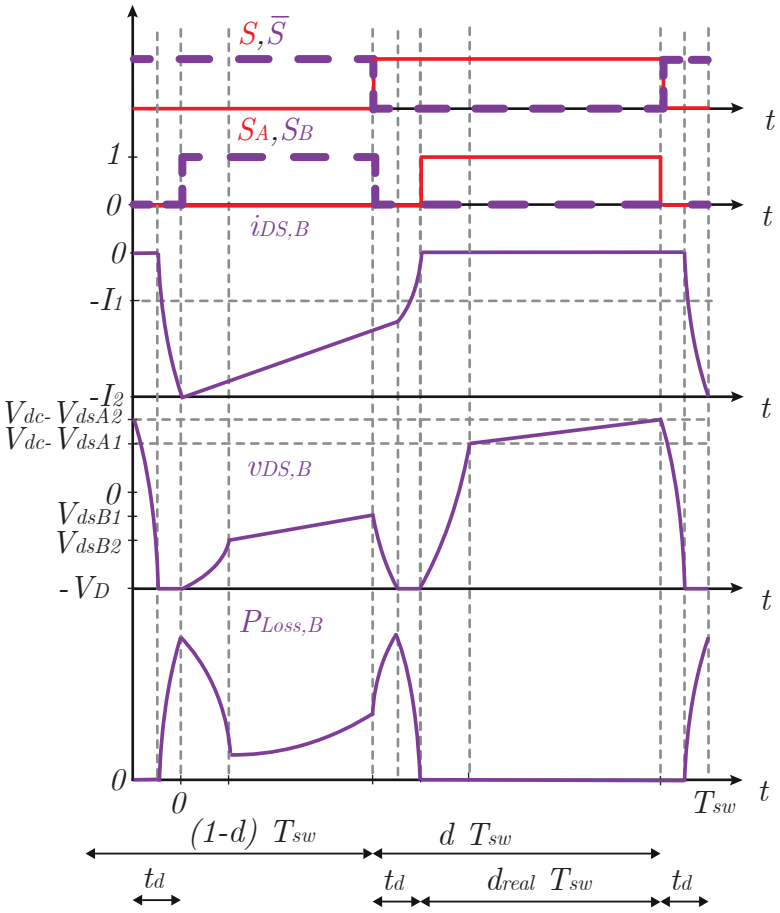

Figure 2.10: Power loss $P_{Loss,B}$ waveform signals.

Power losses can be categorized into conduction and switching losses. Table 2.2 presents the power losses, excluding turn-on and turn-off energy, demonstrating that conduction losses can be represented as $P_{Loss,1} = K_1 R_{on} I^2$. There are also losses dependent on the dead-time t_d and the diode's blocking voltage V_D. Moreover, these losses increase with the switching frequency f_{sw}, as the diode blocking loss power is proportional to $P_{Loss,2} = K_2 V_D I f_{sw} t_d$. Lastly, when considering turn-on and turn-off energy losses, which depend on the DC-link voltage V_{dc}, current I, and switching frequency f_{sw}, the power losses can be described by $P_{Loss,3} = K_3 V_{dc} I f_{sw}$. Therefore, the total loss powers P_{Loss} of GaN devices can be described as:

$$P_{Loss} = P_{Loss,A} + P_{Loss,B} = K_1 R_{on} I^2 + K_2 V_D I f_{sw} t_d + K_3 V_{dc} I f_{sw} \tag{2.81}$$

Finally, it should be considered that the conduction resistances R_{on} of GaN devices depend on the junction temperature. In Fig. 2.11 is illustrated the expected power loss variations with respect to current I, switching frequency f_{sw}, and junction temperature T_j.

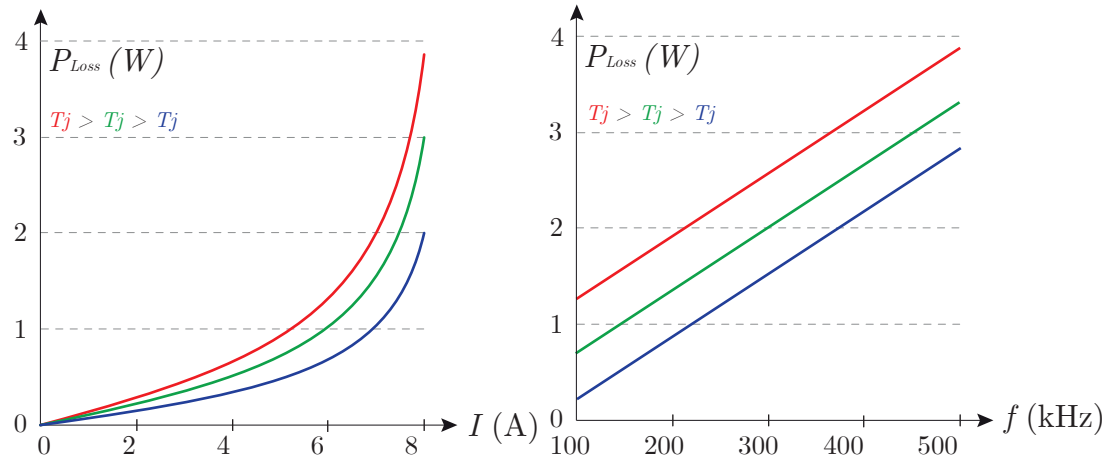

(a) Variation of I respect to T_j with fixed f_{sw} (b) Variation of f_{sw} respect to T_j with fixed I

Figure 2.11: Variation of Power Loss devices respect to current I and switching frequency f_{sw}.

2.5.3 Aproximation of thermal model

To avoid a complex mathematical analysis to obtain an expression for a complete thermal model of the system, fitting a first-order model as (2.84), based on a simulation step response as shown in Fig. 2.12 is an adequate first approximation and sufficient to achieve the objective of this work. Considering that T_{jA} and T_{jB} are the junction temperatures associated to Q_A and Q_B semiconductors, the measurement of the model temperature is made such that:

$$T(t) = \max\{T_{jA}(t), T_{jB}(t)\} \tag{2.82}$$

where the maximum value $T(t)$ is used as the relevant merit figure [76]. Since the temperature dynamics are slower than the electrical dynamics, that is, current and voltage dynamics, the temperature response is modeled as a first-order continuous model, yielding an approximate thermal model as follows:

$$G_t(s) = \frac{\Delta\hat{T}}{\Delta\hat{f}_{sw}} = \frac{K_{th}}{\tau_{th}s + 1} \tag{2.83}$$

And in continuous-time:

$$\frac{dT}{dt} = \frac{T_1 - T}{\tau_{th}} - \frac{K_{th}}{\tau_{th}}(f_{sw} - f_{sw1}) \tag{2.84}$$

where,

$$K_{th} = \frac{T_2 - T_1}{f_{sw2} - f_{sw1}} \qquad T_{4\tau} = T_1 + 0.98(T_2 - T_1) \qquad \tau_{th} = \frac{t_{4\tau} - t_0}{4} \tag{2.85}$$

This approximated first-order thermal model is discretized by ZOH method considering implementation delay which gives:

$$T(k+2) = b_1 T(k+1) + b_2 f_{sw}(k) + b_3, \tag{2.86}$$

with $T_{s,T}$ the temperature sampling time and coefficients:

$$b_1 = e^{-T_{s,T}/\tau_{th}} \qquad b_2 = K_{th}(1-b_1) \qquad b_3 = (1-b_1)T_1 - b_2 f_{sw1} \tag{2.87}$$

Since the temperature dynamics are much slower than those of the current control system, a lower sampling frequency $f_{s,T} = 1/T_{s,T}$ for ATC is established.

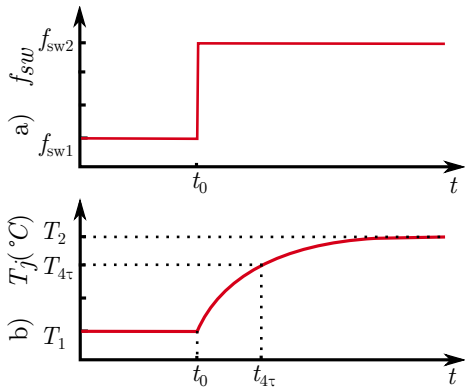

Figure 2.12: Waveform of signals for approximated thermal model. a) Switching frequency step at $t = t_o$. b) Junction temperature evolution

In this model, the effects of current I and ambient temperature T_a are not considered, making the approximate model subject to modeling errors and perturbations. Therefore, to improve the model it is necessary to consider that $b_2 = b_2(I)$ and $b_3 = b_3(I, T_a)$.

2.5.4 Summary

To model the TLBC, there are two systems. First, the discrete electrical system is represented as:

$$\begin{bmatrix} i_L(k+2) \\ v_o(k+2) \end{bmatrix} = \left(\begin{bmatrix} a_1 & a_2 \\ a_5 & a_6 \end{bmatrix} + \begin{bmatrix} a_3 & 0 \\ 0 & 0 \end{bmatrix} d(k) \right) \begin{bmatrix} i_L(k+1) \\ v_o(k+1) \end{bmatrix} + \begin{bmatrix} a_4 \\ 0 \end{bmatrix} d(k) \tag{2.88}$$

where $0 \leq d(k) \leq 1$. Secondly, the thermal system is described by:

$$T(k+2) = b_1 T(k+1) + b_2 f_{sw}(k) + b_3, \tag{2.89}$$

where $f_{sw.min} \leq f_{sw}(k) \leq f_{sw.max}$, and $f_{sw.min}$ and $f_{sw.max}$ represent the minimum and maximum switching frequencies at which the converter can operate, respectively.

In the subsequent chapter, both systems can be effectively controlled using CCS-MPC by solving an Optimal Control Problem (OCP) tailored to each system's dynamics.

Chapter 3

CCS-MPC IN DC-DC POWER CONVERTERS

LINEAR control, particularly with Proportional-Integral (PI) controllers, stands as a fundamental approach in the control of power converters. This introduction provides a foundational understanding of the basic operation, advantages, disadvantages, and limitations inherent in continuous and discrete PI controllers. The continuous and discrete PI controllers are represented in Eq. (3.1):

$$C_c(s) = \frac{K_{pc}s + K_{ic}}{s} \qquad\qquad C_d(z) = \frac{K_{pd} \cdot z - K_{id}}{z - 1} \tag{3.1}$$

These controllers play a critical role in regulating the system by modifying the input based on the error signal, effectively minimizing discrepancies between the desired and actual outputs. While continuous PI controllers are implemented in the Laplace domain (s), their discrete counterparts operate in the Z domain (z), taking into account the digital nature of many control systems.

To mitigate the challenges associated with integral windup, an anti-windup structure, illustrated in Fig. 3.1, can be incorporated. This mechanism restricts the actuation, preventing the integral term from causing overshoots or instability during saturation conditions.

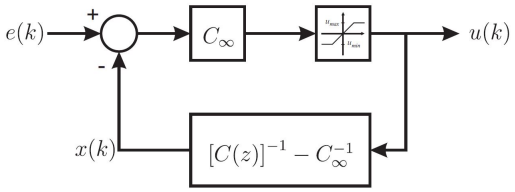

Figure 3.1: Anti-windup block diagram.

The incorporation of PI controllers in power converter control schemes offers significant advantages, such as simplicity, ease of implementation, and zero steady-state error. However, they are not exempt from limitations, including sensitivity to parameter variations and their inherent inability to manage systems with long time delays or those demonstrating significant nonlinearity, as well as a slow response to disturbances.

Building upon this discussion of PI controllers, the subsequent sections delve into the description and implementation of Model Predictive Control (MPC), providing a comprehensive foundation for understanding the control strategies applied in the following chapters.

3.1 Optimal Control

The content of this section is based on [87] and [88]. Notations and definitions are presented to facilitate the understanding of Model Predictive Control (MPC), which is considered an Optimal Control Problem (OCP).

3.1.1 Concepts

An OCP involves several key concepts, including system class, cost function, prediction horizon, and constraints.

3.1.1.1 System Class

Various system classes exist. The most realistic models are continuous time-varying systems:

$$\dot{x}(t) = f(t, x(t), u(t)) \ , \ x(0) = x_0 \tag{3.2}$$

Here, x represents the states in $\mathbb{R}^n$, $x(0)$ denotes the initial condition of the system, and u represents the control inputs in $\mathbb{R}^m$. However, for most cases, it is assumed that these systems are continuous and time-invariant:

$$\dot{x}(t) = f(x(t), u(t)) \ , \ x(0) = x_0 \tag{3.3}$$

A special case are Linear Systems:

$$\dot{x}(t) = Ax(t) + Bu(t) \ , \ x(0) = x_0 \tag{3.4}$$

However, these systems must be discretized in order to perform optimal control. In general, can be obtained discrete time-varying systems:

$$x(k+1) = f(k, x(k), u(k)) \ , \ x(0) = x_0 \tag{3.5}$$

However, time-invariant discrete-time nonlinear system are the focus of study, expressed as:

$$x(k+1) = f(x(k), u(k)) \tag{3.6}$$
$$x(0) = x_0 \tag{3.7}$$
$$k \in \mathbb{N}_0 \tag{3.8}$$

The notation for sequences are defined as:

$$\underline{u}^N = \{u(0), u(1), ..., u(N-1)\} \tag{3.9}$$
$$\underline{u}^\infty = \{u(0), u(1), ...\} \tag{3.10}$$
$$\underline{x}^N = \{x(0), x(1), ..., x(N)\} \tag{3.11}$$
$$\underline{x}_{\underline{u}}^N(x_0) = \{x_{\underline{u}}(0, x_0), x_{\underline{u}}(1, x_0), ..., x_{\underline{u}}(N, x_0)\} \tag{3.12}$$

A simple example is given with the system in Equation (3.13) that requires initial conditions:

$$x(k+1) = x(k) + u(k) \tag{3.13}$$

Two cases, illustrated in Fig. 3.2, are analyzed.

- Case 1: $x(0) = 0$, $u(k) = 1$, $\forall k \in \mathbb{N}_0$
- Case 2: $x(0) = 1$, $u(k) = 1$, $\forall k \in \mathbb{N}_0$

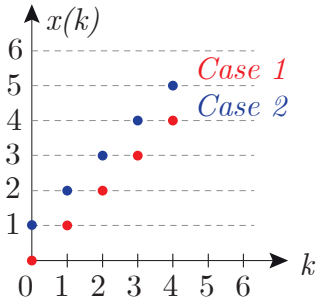

Figure 3.2: Example cases illustrating the influence of initial conditions

Therefore, predictive control systems depend closely on initial conditions [89, 90].

3.1.1.2 Cost Function

A cost function specifies the control target, such as regulation, tracking, or energy minimization, depending on the prediction horizon N_p (Finite or Infinite).

Infinite Horizon:

$$J_\infty(x_0, \underline{u}^\infty) = \sum_{k=0}^{\infty} l(x_{\underline{u}}(k, x_0), u(k)) \tag{3.14}$$

Here, $J_\infty(x_0, \underline{u})$ is the cost function to minimize or the reward to maximize, and $l(x_{\underline{u}}(k, x_0), u(k))$ represents the stage cost.

Finite Horizon:

$$J_N(x_0, \underline{u}^N) = J_f(x_{\underline{u}}(N, x_0)) + \sum_{k=0}^{N-1} l(x_{\underline{u}}(k, x_0), u(k)) \tag{3.15}$$

Where $J_f(x_{\underline{u}}(N, x_0))$ is the terminal or target cost. The ultimate goal is to find a minimizing trajectory $\underline{u}$ for the cost function, where:

$$\underline{u} = \{u(0), ..., u(N-1)\} \tag{3.16}$$

Regulation involves the asymptotic stabilization of equilibrium $x_{eq} = 0$. For discrete-time systems, $x^+ = f(x, u)$ e.g., $u_{eq} = 0$ implies $x_{eq} = f(x_{eq}, 0)$. For continuous-time systems, $\dot{x} = f(x, u)$ e.g., $u_{eq} = 0$ implies $0 = f(x_{eq}, 0)$.

To clarify two examples are analyzed:

- System 1: $x^+ = x + u$
  Case 1: If $u_{eq} = 1$ then $x_{eq} = x_{eq} + 1$ and there is no equilibrium point.
  Case 2: If $u_{eq} = 0$ then $x_{eq} = x_{eq}$ and any state is an equilibrium point.
- System 2: $x^+ = -\frac{1}{2}(x^2 + 1)$ then there is only one equilibrium point such that $x_{eq} = -1$.

An example of cost function for regulation is:

$$J = \frac{1}{2} \sum_{k=0}^{\infty} \left(||x(k)||_Q^2 + ||u(k)||_R^2 \right) \tag{3.17}$$

$$J = \frac{1}{2} \sum_{k=0}^{\infty} \left(x^T(k) Q x(k) + u^T(k) R u(k) \right) \tag{3.18}$$

where Q and R are positive (semi-) definite matrices and Q is a diagonal matrix. This cost function is minimized by regulating $x(k)$ and $u(k)$ to 0. Then, an example of cost function to stabilize the system with a reference trajectory is:

$$J = \frac{1}{2} \sum_{k=0}^{\infty} \left(||x(k) - x^{ref}(k)||_Q^2 + ||u(k) - u^{ref}(k)||_R^2 \right) \tag{3.19}$$

This minimization problem is known as unconstrained OCP which becomes Nonlinear Programming (NLP):

$$\min_{\underline{u}} \; J_N(x_o, \underline{u}) \tag{3.20}$$

Where $\underline{u}^*$ is the optimal control input trajectory:

$$\underline{u}^* = u^*(0, x_0), u^*(1, x_0), ... \tag{3.21}$$

And the optimal cost value function is:

$$J_N(x_0, \underline{u}^*) = J_N^*(x_0) \tag{3.22}$$

3.1.1.3 Constraints

However, it's important to acknowledge that all systems come with constraints, whether imposed on states or input control signals. These restrictions may manifest as hard constraints, where strict adherence is mandatory, or soft constraints, allowing for a degree of permissiveness within predefined bounds. While it's desirable for constraints to be met, soft constraints offer some flexibility within a permissible range, whereas hard constraints must unequivocally be satisfied. Input constraints on $u(k)$ due to physical limitations of actuators can be written for example as:

$$u_{min} \leq u(k) \leq u_{max} \tag{3.23}$$

However, the general notation is:

$$h(u(k)) = 0 \qquad\qquad g(u(k)) \leq 0 \tag{3.24}$$

A more convenient notation is done with a set $\mathbb{U}$ where:

$$u(k) \in \mathbb{U} = \{u : h(u) = 0 \wedge g(u) \leq 0\}, \forall k \tag{3.25}$$

An example is illustrated in Fig. 3.3, where $\mathbb{U}$ is defined as:

$$\mathbb{U} = \{u_1, u_2 \in \mathbb{R}^+ : u_1 + u_2 \leq 5\} \tag{3.26}$$

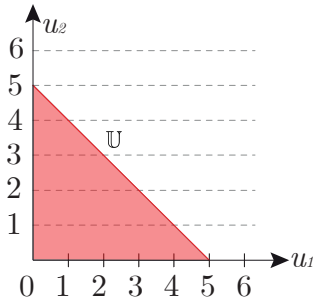

Figure 3.3: Example case of Input Constraints

Similarly, there are state constraints that generally define the controller specifications such that the set $\mathbb{X}$ is the constraints for all states except the last state N that is considered in the set $\mathbb{X}_f$ such that:

$$x(k) \in \mathbb{X} \ , \ x(N) \in \mathbb{X}_f \ , \ k \in \mathbb{N}_o \tag{3.27}$$

Additionally, combinations of state and input constraints are considered. For example, the system defined in Eq. (3.13) is analyzed with input and state constraints as defined in Eq. (3.28).

$$x(k+1) = x(k) + u(k) \tag{3.28a}$$
$$x(0) = 3 \tag{3.28b}$$
$$\mathbb{X} = \{x(k) \in \mathbb{R} : x(k) \leq 5\} \tag{3.28c}$$
$$\mathbb{U} = \{-1, 1, 3\} \tag{3.28d}$$

In Fig. 3.4 is shown that for given x_0, not all $u \in \mathbb{U}$ are admissible and not all x_0 are feasible.

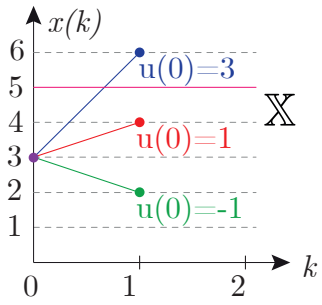

Figure 3.4: Example case of Input and State Constraints

The set with all admissible control input sequences is $\mathcal{U}_N(x_0)$ defined as:

$$\mathcal{U}_N(x_0) := \{\underline{u} : u(k) \in \mathbb{U}, x_{\underline{u}}(k, x_0) \in \mathbb{X}, x_{\underline{u}}(N, x_0) \in \mathbb{X}_f\} \tag{3.29}$$

And the set with feasible initial values for a horizon of length N is $\mathcal{X}_N$ defined as:

$$\mathcal{X}_N := \{x_0 \in \mathbb{X} : \mathcal{U}_N(x_0) \neq \emptyset\} \tag{3.30}$$

In the above example these sets are $\mathcal{U}_1(3) = \{1, -1\}$ and $\mathcal{X}_1 = \{x_0 \in \mathbb{R} : x_0 \leq 4\}$.

Finally a constrained OCP is defined such that

$$\mathbb{P}_N(x_0) : J_N^*(x_0) = \min_{\underline{u}} \{J_N(x_0, \underline{u}) : \underline{u} \in \mathcal{U}_N(x_0)\} \tag{3.31}$$

That is

$$\min_{\underline{u}} \; J_N(x_o, \underline{u}) = J_f(x(N)) + \sum_{k=0}^{N-1} l(x(k), u(k)) \tag{3.32}$$
$$\text{s.t. } x(k+1) = f(x(k), u(k)) \;,\; k \in [0, N-1] \tag{3.33}$$
$$x(k) \in \mathbb{X} \tag{3.34}$$
$$u(k) \in \mathbb{U} \tag{3.35}$$

A solution to $\mathbb{P}_N(x_0)$ exists for all $x_0 \in \mathcal{X}_N$ if Assump. 1 and 2 are fulfilled.

Assumption 1. *The functions f, l and J_f are continuous.*
For regulation if $f(0,0) = 0, l(0,0) = 0, J_f(0) = 0$ then $J_N(x_0, \underline{u})$ is continuous in $\underline{U}$.

Assumption 2. *The set $\mathbb{X}$ is closed, and the sets $\mathbb{X}_f$ and $\mathbb{U}$ are compact.*
For regulation if $\mathbb{X}, \mathbb{X}_f, \mathbb{U}$ contain the origin then $\mathcal{U}_N(x_0)$ is compact.

Also, the Weierstrass Theorem [91] is helpful since it proves that there is always an optimal solution under certain conditions.

Theorem 1. *Weierstraβ Theorem: Existence of a Global Minimum. If f(x) is continuous on a nonempty feasible set S that is closed and bounded, then f(x) has a global minimum in S.*

To solve this NLP, Lagrange multipliers λ and μ are used such that $F(\underline{u}) = J_N(x_0, \underline{u})$ and the lagrangian function $\mathcal{L}$ is:

$$\mathcal{L}(\underline{u}) = F(\underline{u}) + \mu^T g(\underline{u}) + \lambda^T h(\underline{u}) \tag{3.36}$$

To solve a general optimization problem Karush–Kuhn–Tucker (KKT) conditions are used [57] such that:

$$\begin{aligned}
&I) \;\; g_i(\underline{u}) \leq 0 \;,\; i = 1, ..., m \\
&II) \;\; h_j(\underline{u}) = 0 \;,\; j = 1, ..., p \\
&III) \;\; \mu_i \geq 0 \\
&IV) \;\; \mu_i \cdot g_i(\underline{u}) = 0 \\
&V) \;\; \nabla_{\underline{u}} \mathcal{L}(\underline{u}) = \nabla_{\underline{u}} F(\underline{u}) + \sum_{i=1}^{m} \mu_i \cdot \nabla_{\underline{u}} g_i(\underline{u}) + \sum_{j=1}^{p} \lambda_i \cdot \nabla_{\underline{u}} h_j(\underline{u}) = 0
\end{aligned} \tag{3.37}$$

Where,

$$g(\underline{u}) = \begin{bmatrix} g_1(\underline{u}) \\ \vdots \\ g_i(\underline{u}) \end{bmatrix} \qquad h(\underline{u}) = \begin{bmatrix} h_1(\underline{u}) \\ \vdots \\ g_j(\underline{u}) \end{bmatrix} \qquad \mu = \begin{bmatrix} \mu_1 \\ \vdots \\ \mu_i \end{bmatrix} \qquad \lambda = \begin{bmatrix} \lambda_1 \\ \vdots \\ \lambda_j \end{bmatrix} \tag{3.38}$$

3.1.1.4 Fixed Horizon and Receding Horizon

In open-loop control, the objective is to determine $\underline{u}^*$ in advance based on the model. However, due to uncertainties and disturbances, as illustrated in Figure 3.5, all systems must operate in closed-loop control. In closed-loop control, the goal is to find $u^*(k)$ at each time step using the measured state $x(k)$, such that $u^*(k) = \kappa_N(x(k))$. Nonetheless, prediction becomes essential for decision-making. Generally, solving the optimal control problem at each time step to determine the current optimal control can be time-consuming, particularly when $\underline{u} \in \mathbb{R}^m$, where m corresponds to the number of control inputs considered in the prediction in both FCS and CCS.

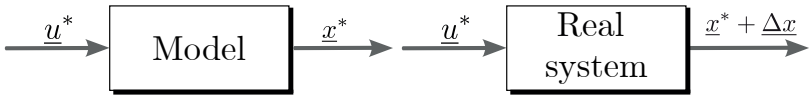

(a) Ideal open loop control with model (b) Real open loop control in system

Figure 3.5: Feedforward optimal control

There two approaches for prediction, Fixed horizon strategy and Receding horizon strategy. These approaches are ilustrated in Fig. 3.6.

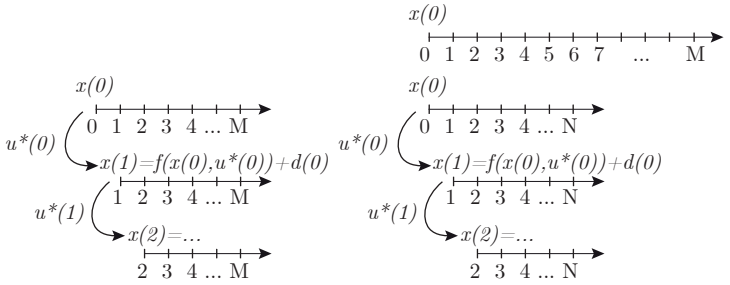

(a) Fixed horizon strategy (b) Receding Horizon Strategy

Figure 3.6: Horizon prediction approaches

The challenge with a fixed horizon strategy lies in the computational effort required to compute every prediction step until reaching the designated horizon M. If the system class, cost, and constraints are simple enough, analytical solutions for the control law are feasible. For example:

- LQ control: $u^*(k) = \kappa(k)\ x(k)$
- Dynamic Programming: $u^*(k) = \mu_\kappa(x(k))$

On the other hand, the receding horizon strategy delivers an approximated optimal solution within a smaller prediction horizon N and is commonly used in Model Predictive Control. In each iteration, an optimal control input set is obtained as $u^*(x(k)) = \{u^*(k, x(k)), u^*(k+1, x(k)), ...\}$. However, only the first entry is applied to the system, resulting in to the system such that:

$$u^*(k) = \kappa_k(x(k)) = u^*(k, x(k)) \tag{3.39}$$

For time-invariant systems, the current state is always $x(0) = x$. Thus, every prediction delivers $u^*(x) = \{u^*(k, x), u^*(k+1, x), ...\}$, and only $u^*(0)$ is applied to the system. Consequently, the controller can be expressed as:

$$u^*(0, x_0) = \kappa_N(x_0) \tag{3.40}$$

with $u^*(0, x_0)$ from $\underline{u}^* = \{u^*(0, x_0), u^*(1, x_0), ..., u^*(N-1, x_0), \}$ as solution of $\mathbb{P}_N(x_0)$.

3.1.2 Model Predictive Control

The general problem is time-invariant where

$$\text{System: } x(k+1) = f(x(k), u(k)) \tag{3.41}$$
$$x(0) = x_0 \tag{3.42}$$
$$\text{Cost: } J_M = J_f(x(M)) + \sum_{k=0}^{M-1} l(x(k), u(k)) \tag{3.43}$$
$$\text{Constraints: } x(k) \in \mathbb{X} \tag{3.44}$$
$$x(M) \in \mathbb{X}_f \tag{3.45}$$
$$u(k) \in \mathbb{U} \tag{3.46}$$
$$\tag{3.47}$$

The primary objective is to determine the optimal feedback control strategy. The concept of Model Predictive Control (MPC) involves solving the Optimal Control Problem (OCP) on a short horizon N where $N << M$ only for a specific $x \in \mathcal{X}_N$. This solution is computed in a forward direction, employing a receding horizon strategy. As illustrated in Fig. 3.7, an optimal solution is obtained in each MPC iteration, allowing for a limited time for solution. The receding horizon has a length of N sufficient to appropriately consider constraints and minimize costs.

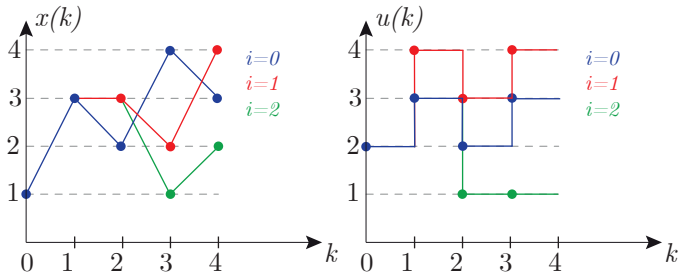

(a) State (b) Input

Figure 3.7: Receding Horizon in MPC

Formally the first MPC optimal control problem is

$$\text{Minimize cost: } J_N(x_0, \underline{u}) = J_{0\to N}(x_0, \underline{u}) = J_f(x(N) + \sum_{k=0}^{N-1} l(x(k), u(k))$$
$$\text{for control inputs: } \underline{u} = \{u(0), u(1), ..., u(N-1)\}$$
$$\text{with constraints: } \underline{u} \in \mathcal{U}_N(x_0) = \mathcal{U}_{0\to N}(x_0)$$
$$\text{set current control input: } u(0) = \kappa_N(x_0) = \kappa_{0\to N}(x_0) = u^*(0)$$
$$\text{apply control and obtain: } x(1) = f(x_0, \kappa_N(x_0)) + d$$

MPC solves full problem in a sub-optimal way by iteratively solving an OCP on a receding horizon N. MPC delivers control action u for one specific realization of x and for a time-invariant close-loop system such that $x^+ = f(x, \kappa_N(x))$.

An example of stability of MPC (Exercise 6.1, pp. 185-186 [92]) is presented. The system is defined as:

$$x^+ = \begin{bmatrix} 0 & 0 \\ 1 & 0 \end{bmatrix} x + \begin{bmatrix} 1 \\ 0 \end{bmatrix} u \qquad\qquad x = \begin{bmatrix} x_1 \\ x_2 \end{bmatrix} \tag{3.48}$$

With the prediction horizon N and the cost function J_N:

$$J_N = \sum_{k=1}^{N-1} x(k)^T \begin{bmatrix} 1 & 2 \\ 2 & 6 \end{bmatrix} x(k) \tag{3.49}$$

If $N = 1$ then $x_1(1) = u(0)$ and $x_2(1) = x_1(0)$, and the cost function J_1 is:

$$J_1 = x_1(1)^2 + 4x_1(1)x_2(1) + 6x_2(1)^2 = u(0)^2 + 4u(0)x_1(0) + 6x_2(0)^2 \tag{3.50}$$

To solve this OCP the derivate of J_1 is obtained and equal to zero.

$$\frac{dJ_1}{du(0)} = 2u(0) + 4x_1(0) = 0 \qquad \longrightarrow \qquad u(0) = -2x_1(0) = \begin{bmatrix} -2 & 0 \end{bmatrix} x(0) \tag{3.51}$$

Therefore, the ideal closed-loop system is:

$$x^+ = \begin{bmatrix} 0 & 0 \\ 1 & 0 \end{bmatrix} x + \begin{bmatrix} 1 \\ 0 \end{bmatrix} \begin{bmatrix} -2 & 0 \end{bmatrix} x = \begin{bmatrix} -2 & 0 \\ 1 & 0 \end{bmatrix} x \tag{3.52}$$

The closed-loop stability can be determined by obtaining the eigenvalues of A_{cl} such that:

$$A_{cl} = \begin{bmatrix} -2 & 0 \\ 1 & 0 \end{bmatrix} \qquad\qquad |A_{cl} - \lambda I_2| = \begin{vmatrix} -2-\lambda & 0 \\ 1 & -\lambda \end{vmatrix} = \lambda(\lambda + 2) = 0 \tag{3.53}$$

The eigenvalues of the closed-loop system are $\lambda \in \{0, -2\}$ and since one of them has a modulus greater than 1 then the system is unstable. However, if $N = 2$ then $x_1(1) = u(0)$, $x_2(1) = x_1(0)$, $x_1(2) = u(1)$ and $x_2(2) = x_1(1) = u(0)$, and the cost function J_2 is

$$J_2 = x_1(1)^2 + 4x_1(1)x_2(1) + 6x_2(1)^2 + x_1(2)^2 + 4x_1(2)x_2(2) + 6x_2(2)^2 \tag{3.54}$$

$$J_2 = 7u(0)^2 + 4u(0)x_1(0) + 4u(0)u(1) + u(1)^2 + 6x_1(0)^2 \tag{3.55}$$

This OCP is solved calculating the gradient of J_2 and equaling to zero

$$\nabla J_2 = \left(\frac{dJ_2}{du(0)}, \frac{dJ_2}{du(1)} \right)^T = (14u(0) + 4x_1(0) + 4u(1), 4u(0) + 2u(1))^T = (0, 0)^T \tag{3.56}$$

Solving this system of equations

$$u(1) = -2u(0) \qquad\qquad u(0) = -\frac{2}{3}x_1(0) = \begin{bmatrix} -\frac{2}{3} & 0 \end{bmatrix} x(0) \tag{3.57}$$

Therefore, the ideal closed-loop system is

$$x^+ = \begin{bmatrix} 0 & 0 \\ 1 & 0 \end{bmatrix} x + \begin{bmatrix} 1 \\ 0 \end{bmatrix} \begin{bmatrix} -\frac{2}{3} & 0 \end{bmatrix} x = \begin{bmatrix} -\frac{2}{3} & 0 \\ 1 & 0 \end{bmatrix} x \tag{3.58}$$

The closed-loop stability can be determined by obtaining the eigenvalues of A_{cl} such that

$$A_{cl} = \begin{bmatrix} -\frac{2}{3} & 0 \\ 1 & 0 \end{bmatrix} \qquad |A_{cl} - \lambda I_2| = \begin{vmatrix} -\frac{2}{3} - \lambda & 0 \\ 1 & -\lambda \end{vmatrix} = \lambda\left(\lambda + \frac{2}{3}\right) = 0 \tag{3.59}$$

The eigenvalues of the closed-loop system are $\lambda \in \{0, -2/3\}$ and since all of them have modulus less than 1 then the system is stable. Therefore, there is a minimum horizon prediction to achieve stability. However, not all systems can be stabilized even if horizon prediction is infinite. MPC Stability is explained in detail in [87], Chapter 2, Section 2.4. The stability of MPC is proven by the Lyapunov theorem using the cost function as the Lyapunov function.

3.1.3 Linear Optimal Control

The following strategies are used when the system has a linear structure as Eq. (3.60).

$$x^+ = f(x,u) = Ax + Bu \tag{3.60}$$

with $x \in \mathbb{R}^n$, $u \in \mathbb{R}^m$ and $x(0) = x$. The cost function has a structure similar to (3.17) where:

$$J_N(x,\underline{u}) = \frac{1}{2}||x(N)||_{P_f} + \frac{1}{2}\sum_{k=0}^{N-1}\left(||x(k)||_Q^2 + ||u(k)||_R^2\right) \tag{3.61}$$

And the constraints are linear such that $x(k) \in \mathbb{X}$, $u(k) \in \mathbb{U}$ and $x(N) \in \mathbb{X}_f$. Where $\mathbb{X}, \mathbb{U}, \mathbb{X}_f$ are convex polytopes, see Fig. 3.3.

3.1.3.1 LQ Control

Linear Quadratic (LQ) control strategy does not contain constraints and optimal control law $u(k)$ is explicitly calculated applying Bellman Recursion with Eq. (3.62).

$$u(k) = \kappa(k)x(k) \tag{3.62a}$$
$$\kappa(k) = -(B^TP(k+1)B + R)^{-1}B^TP(k+1)A \tag{3.62b}$$
$$P(k) = A^TP(k+1)A + Q - A^TP(k+1)B(B^TP(k+1)B + R)^{-1}B^TP(k+1)A \tag{3.62c}$$
$$P(N) = P_f \tag{3.62d}$$

It is possible to extend this strategy to infinite horizon ($N \to \infty$) such that:

$$J_\infty(x,\underline{u}) = \frac{1}{2}\sum_{k=0}^{\infty}\left(||x(k)||_Q^2 + ||u(k)||_R^2\right) \tag{3.63}$$

The solution is the stationary Riccatti Matrix P_∞ calculated by iteration with Eq. (3.64).

$$\kappa_\infty = -(B^TP_\infty B + R)^{-1}B^TP_\infty A \qquad P_\infty = A^TP_\infty A + Q + \kappa_\infty^T B^TP_\infty A \tag{3.64}$$

Starting with $P_\infty = 0$ till convergence, finally $u(k) = \kappa_\infty x(k)$. The stability of LQ control is proven with Theorem 2.

Theorem 2. *LQ Control Stability: If (A, B) stabilizable/controllable then $x_{eq} = 0$ is asymptotically stable under LQ control.*

An interpretation can be done with eigenvalues, also known as the indirect method. Where:

$$x^+ = Ax + B(\kappa_\infty x) = (A + B\kappa_\infty)x \tag{3.65}$$

The eigenvalues of $A + B\kappa_\infty$ are strictly inside unit circle. However, if (A, B) not stabilizable or controllable there are states that cannot be controlled by u. Then they will not converge to 0 and the cost will be infinite.

An excellent LQ control example is from [93] Examples 13.2 and 13.3, where a simple linear discrete-time plant defined in Eq. (3.13) ($x(k+1) = x(k) + u(k)$). With $x(0) = x_0$ and optimal feedback control $u(k) = \kappa(k)x(k)$ that minimizes the cost J_N:

$$J_N = \frac{1}{2}Sx(N)^2 + \frac{1}{2}\sum_{k=0}^{N-1}(x(k)^2 + ru(k)^2)\ ,\ S \geq 0\ ,\ r \geq 0 \tag{3.66}$$

has to be designed in the framework of LQ control. Then:

$$P(N) = S \qquad P(k) = \frac{(r+1)P(k+1) + r}{P(k+1) + r} \qquad \kappa(k) = -\frac{P(k+1)}{P(k+1) + r} \tag{3.67}$$

If $N = 4$, $r = 1$, $x(0) = 2$ and the extrem values of S are evaluated in Tab. 3.1. It is possible to conclude that the cost function weights significantly affect the optimal solution. Conceptually, it gives more importance to their cost when their value is greater. For example, the final state $x(N)$ is stabilized at 0 because as S tends to infinity its cost when multiplied must be minimized. On the other hand, when S tends to 0, $x(N)$ tends to have a value close to 0 but since it does not have a significant weight in the cost, it is not given preference to minimize it.

Table 3.1: LQ control finite horizon example

S	x(0)	$\kappa(0)$	u(0)	x(1)	$\kappa(1)$	u(1)	x(2)	$\kappa(2)$	u(2)	x(3)	$\kappa(3)$	u(3)	x(4)
0	2	-8/13	-16/13	10/13	-3/5	-6/13	4/13	-1/2	-2/13	2/13	0	0	2/13
∞	2	-13/21	-26/21	16/21	-5/8	-10/21	6/21	-2/3	-4/21	2/21	-1	-2/21	0

For the same system where $A = 1$, $B = 1$, $P_f = S$, $Q = 1$, $R = r$ the stationary Riccatti Matrix P_∞ is calculated with Eq. (3.64) as follows:

$$\kappa_\infty = -\frac{P_\infty}{P_\infty + r} \qquad P_\infty = P_\infty + 1 - \kappa_\infty P_\infty \tag{3.68}$$

where a quadratic equation is obtained and solved such that:

$$0 = P_\infty^2 - P_\infty - r \qquad \longrightarrow \qquad P_\infty = \frac{1 + \sqrt{1+4r}}{2} \qquad \kappa_\infty = -\frac{1 + \sqrt{1+4r}}{1 + \sqrt{1+4r} + 2r} \tag{3.69}$$

Then the closed-loop system is:

$$x(k+1) = (1 + \kappa_\infty)x(k) = \frac{2r}{1 + \sqrt{1+4r} + 2r}x(k) \tag{3.70}$$

And it is stable if:

$$\left|\frac{2r}{1+\sqrt{1+4r}+2r}\right| < 1 \tag{3.71}$$

Which is true if $r \geq 0$. Furthermore, in the extrem values

- When $r = 0$ then $u(k) = -x(k)$ and $x(k+1) = 0$
- When $r \to \infty$ then $u(k) = 0$ and $x(k+1) = x(k)$

An advantage of LQ control is that all intensive calculations are stored offline. However, it does not consider constraints. A common issue in linear optimal control is the challenge of choosing the weighting factors for the cost function (P_f, Q, R). An alternative strategy is Linear Model Predictive Control (MPC), which incorporates constraints but does not necessarily guarantee the stabilization of the origin.

The stability of Linear Systems via Lyapunov Equation has underlying theory [94] such that:

- If equilibrium is stable then a Lyapunov function exists.
- If equilibrium of linear system is stable then a Lyapunov function exists and it is quadratic.

Considering a linear system $x^+ = \tilde{A}x$ with $x = 0$ asymptotically stable, a Lyapunov function candidate is:

$$V(x) = x^T P x \tag{3.72}$$

with $P > 0$. The descent condition is a Linear Matrix Inequation (LMI) such that:

$$V(x^+) - V(x) = (x^+)^T P(x^+) - x^T P x = x^T \tilde{A}^T P \tilde{A} x - x^T P x = x^T(\tilde{A}^T P \tilde{A} - P)x < 0 \tag{3.73}$$

A suitable P fulfills $\tilde{A}^T P \tilde{A} - P < 0$ e.g. set $\tilde{Q}$ postive definite ($\tilde{Q} > 0$) and solve the Lyapunov Equation (LE):

$$\tilde{A}^T P \tilde{A} - P = -\tilde{Q} \tag{3.74}$$

If P that solves LE for some $\tilde{Q} > 0$ is positive define then $x_{eq} = 0$ is asymptotically stable.

For example in LQ control $\tilde{A} = A + B\kappa$ and the LE is

$$(A + B\kappa)^T P(A + B\kappa) - P = -\tilde{Q} \tag{3.75}$$

e.g. $\tilde{Q} = Q + \kappa_\infty^T R \kappa_\infty$ then $P = P_\infty$ is the Riccati Matrix. Riccati equation is a LE and $V_{LQ} = \frac{1}{2}x^T P_\infty x$ is Lyapunov function of LQ control [95].

3.1.3.2 QP Problems as underlying NLP problems of linear MPC

Consider MPC with prediction horizon N and a cost function J_N given by:

$$\min_{\underline{u}} \; J_N(x, \underline{u}) = \frac{1}{2}P_f x(N)^T P_f x(N) + \frac{1}{2}\sum_{k=0}^{N-1}(x(k)^T Q x(k) + u(k)^T R u(k)) \tag{3.76}$$

$$\text{s.t. } x^+ = Ax + Bu \;,\; k \in [0, N-1] \tag{3.77}$$

$$x(k) \in \mathbb{X} \;,\; u(k) \in \mathbb{U} \;,\; x(N) \in \mathbb{X}_f \tag{3.78}$$

By recursive elimination or prediction of system $x(k+1) = Ax(k) + Bu(k)$ such that:

$$x(1) = Ax_0 + Bu(0) \tag{3.79}$$
$$x(2) = Ax(1) + Bu(1) = A(Ax_0 + Bu(0)) + Bu(1) \tag{3.80}$$
$$... \tag{3.81}$$
$$x(k) = A^k x_0 + A^{k-1}Bu(0) + ... + ABu(k-2)Bu(k-1) \tag{3.82}$$

It is possible to replace $x(1)$, $x(2)$, ..., $x(N)$ in cost function:

$$J_N(x, \underline{u}) = ... + x(1)^T Q x(1) + x(2)^T Q x(2) + ... + x(N-1)^T Q x(N-1) + ... \tag{3.83}$$

This allows to rewrite cost function as:

$$J_N(x, \underline{u}) = \frac{1}{2}\underline{u}^T H \underline{u} + c(x_0)^T \underline{u} + d(x_0) \tag{3.84}$$
$$\underline{u} = \{u(0), ..., u(N-1)\} \in \mathcal{U}_N(x_0) \tag{3.85}$$

To solve Quadratic Problems (QPs), the approach depends on whether it is constrained or not. In each case, the solution is obtained as:

- Unconstrained: Explicit solution $\underline{u} = -H^{-1}c(x_0)$.
- Constrained: Numerical methods are typically employed, although for a few constraints and small dimensions of x, an explicit solution can be found. It is possible to determine explicit control laws offline in such cases.

For example, consider again the system defined in Eq. (3.13) ($x(k+1) = x(k) + u(k)$), the cost function J_N with horizon N and input constraints such that:

$$J_N(x, \underline{u}) = \frac{1}{2}x(N)^2 + \frac{1}{2}\sum_{k=0}^{N-1}(x(k)^2 + u(k)^2) \qquad u(k) \in [-1, 1] \tag{3.86}$$

Assuming a horizon $N = 2$, then:

$$J_2(x, \underline{u}) = \frac{1}{2}(x(2)^2 + x(1)^2 + u(1)^2 + x_0^2 + u(0)^2) \tag{3.87}$$

Using the model dynamics, $x(1)$ and $x(2)$ can be written in terms of $u(0)$, $u(1)$ and x_0 such that:

$$x(1) = x_0 + u(0) \qquad x(2) = x(1) + u(1) = x_0 + u(0) + u(1) \tag{3.88}$$

The cost function can be written as:

$$J_2(x, \underline{u}) = \frac{1}{2}\left(3u(0)^2 + 2u(0)u(1) + 2u(1)^2 + 4x_0u(0) + 2x_0u(1) + 3x_0^2\right) \tag{3.89}$$
$$J_2(x, u) = \frac{1}{2}\begin{bmatrix} u(0) \\ u(1) \end{bmatrix}^T \begin{bmatrix} 3 & 1 \\ 1 & 2 \end{bmatrix} \begin{bmatrix} u(0) \\ u(1) \end{bmatrix} + \begin{bmatrix} 2x_0 \\ x_0 \end{bmatrix}^T \begin{bmatrix} u(0) \\ u(1) \end{bmatrix} + \frac{3}{2}x_0^2 \tag{3.90}$$

The unconstrained solution is obtained with the gradient and equaling it to zero such that:

$$\nabla_{\underline{u}} J_2(x,\underline{u}) = H\underline{u} + c(x_0) = 0 \qquad \longrightarrow \qquad \underline{u} = -H^{-1}c(x_0) = -\frac{1}{5}\begin{bmatrix}3\\1\end{bmatrix}x_0 \tag{3.91}$$

And as MPC only applies the first control input, then:

$$u(k) = -\frac{3}{5}x(k) \tag{3.92}$$

The closed-loop stability of unconstrained problem is checked with the eigenvalues

$$x(k+1) = x(k) - \frac{3}{5}x(k) = \frac{2}{5}x(k) \tag{3.93}$$

As $|\frac{2}{5}| < 1$ the unconstrained closed-loop system is stable. However, considering input constraints (3.86) this solution is only feasible for some x_0, this is:

$$-1 \leq -\frac{3}{5}x_0 \leq 1 \;\longrightarrow\; -\frac{5}{3} \leq x_0 \leq \frac{5}{3} \tag{3.94}$$

A Lagrangian function as in (3.36) is proposed to solve the constrained problem such that:

$$\mathcal{L}(x,\underline{u}) = J_2(x,\underline{u}) + \mu^T g(\underline{u}) \tag{3.95}$$

Where $g(\underline{u})$ and μ are defined as:

$$g(\underline{u}) = \begin{bmatrix} g_1(\underline{u}) \\ g_2(\underline{u}) \\ g_3(\underline{u}) \\ g_4(\underline{u}) \end{bmatrix} = \begin{bmatrix} u(0) - 1 \\ -1 - u(0) \\ u(1) - 1 \\ -1 - u(1) \end{bmatrix} \leq 0 \qquad\qquad \mu = \begin{bmatrix} \mu_1 \\ \mu_2 \\ \mu_3 \\ \mu_4 \end{bmatrix} \tag{3.96}$$

The KKT conditions from (3.37) are shown below for this problem.

$$\begin{aligned} \frac{\partial J_2(x,\underline{u})}{\partial u(0)} + \mu_1 - \mu_2 &= 0 & \qquad \frac{\partial J_2(x,\underline{u})}{\partial u(1)} + \mu_3 - \mu_4 &= 0 \\ \mu_1(u(0) - 1) &= 0 & \qquad \mu_3(u(1) - 1) &= 0 \\ \mu_2(-1 - u(0)) &= 0 & \qquad \mu_4(-1 - u(1)) &= 0 \end{aligned} \tag{3.97}$$

Since μ_1, μ_2 and μ_3, μ_4 cannot be activated at the same time, it is simple to solve the equations for each case. For example, when activating the constraint μ_1, its value must be calculated (μ_1^*) and evaluated to be positive, while μ_2 is 0. Hence,

$$\mu_1^* = \frac{\partial J_2(x,\underline{u})}{\partial u(0)} \qquad \mu_2^* = -\frac{\partial J_2(x,\underline{u})}{\partial u(0)} \qquad \mu_3^* = \frac{\partial J_2(x,\underline{u})}{\partial u(1)} \qquad \mu_4^* = -\frac{\partial J_2(x,\underline{u})}{\partial u(1)} \tag{3.98}$$

After calculating the input control signals $u(0)$ and $u(1)$ in each case, the KKT conditions must be evaluated. For this, it is necessary to evaluate the derivatives of the cost function $J_2(x, \underline{u})$, thus:

$$\nabla_{\underline{u}} J_2(x, \underline{u}) = \begin{bmatrix} \frac{\partial J_2(x,\underline{u})}{\partial u(0)} \\ \frac{\partial J_2(x,\underline{u})}{\partial u(1)} \end{bmatrix} = \begin{bmatrix} 3u(0) + u(1) + 2x_0 \\ u(0) + 2u(1) + x_0 \end{bmatrix} \tag{3.99}$$

It is important to note that in nonlinear restrictions the derivatives of the $g_i(\underline{u})$ depends on $\underline{u}$. However, in this case are constant that is:

$$\nabla_{\underline{u}} g_1(\underline{u}) = \begin{bmatrix} 1 \\ 0 \end{bmatrix} \qquad \nabla_{\underline{u}} g_2(\underline{u}) = \begin{bmatrix} -1 \\ 0 \end{bmatrix} \qquad \nabla_{\underline{u}} g_3(\underline{u}) = \begin{bmatrix} 0 \\ 1 \end{bmatrix} \qquad \nabla_{\underline{u}} g_4(\underline{u}) = \begin{bmatrix} 0 \\ -1 \end{bmatrix} \tag{3.100}$$

With KKT conditions there are $2^4 = 16$ possible cases, these are shown in Tab. 3.2. However, not all cases are feasible due to input restrictions, where u cannot be -1 and 1 at the same time, as in cases 4, 8 and 12-16.

Table 3.2: Possible cases with KKT conditions with $N = 2$ for (3.95)

Case	μ_1	μ_2	μ_3	μ_4	$u(0)$	$u(1)$
1	0	0	0	0	$u_1(0)$	$u_1(1)$
2	μ_1^*	0	0	0	1	$u_2(1)$
3	0	μ_2^*	0	0	-1	$u_3(1)$
4	μ_1^*	μ_2^*	0	0	–	$u_4(1)$
5	0	0	μ_3^*	0	$u_5(0)$	1
6	μ_1^*	0	μ_3^*	0	1	1
7	0	μ_2^*	μ_3^*	0	-1	1
8	μ_1^*	μ_2^*	μ_3^*	0	–	1
9	0	0	0	μ_4^*	$u_9(0)$	-1
10	μ_1^*	0	0	μ_4^*	1	-1
11	0	μ_2^*	0	μ_4^*	-1	-1
12	μ_1^*	μ_2^*	0	μ_4^*	–	-1
13	0	0	μ_3^*	μ_4^*	–	–
14	μ_1^*	0	μ_3^*	μ_4^*	1	–
15	0	μ_2^*	μ_3^*	μ_4^*	1	–
16	μ_1^*	μ_2^*	μ_3^*	μ_4^*	–	–

In Tab. 3.3, only the feasible cases are detailed. These cases has to be tested to find the optimal solution that fullfils KKT conditions.

Table 3.3: Feasible cases with KKT conditions with $N = 2$ for (3.95)

Case	μ_1	μ_2	μ_3	μ_4	$u(0)$	$u(1)$
1	0	0	0	0	$u_1(0)$	$u_1(1)$
2	μ_1^*	0	0	0	1	$u_2(1)$
3	0	μ_2^*	0	0	-1	$u_3(1)$
4	0	0	μ_3^*	0	$u_4(0)$	1
5	μ_1^*	0	μ_3^*	0	1	1
6	0	μ_2^*	μ_3^*	0	-1	1
7	0	0	0	μ_4^*	$u_7(0)$	-1
8	μ_1^*	0	0	μ_4^*	1	-1
9	0	μ_2^*	0	μ_4^*	-1	-1

To find the optimal control constrained solutions the following system equation must be solved activating the restrictions and calculating the values of μ and checking if the KKT conditions are fullfield.

$$\begin{bmatrix} 3u(0) + u(1) + 2x_0 + \mu_1 - \mu_2 \\ u(0) + 2u(1) + x_0 + \mu_3 - \mu_4 \end{bmatrix} = \begin{bmatrix} 0 \\ 0 \end{bmatrix} \qquad -1 \leq \underline{u} \leq 1 \qquad \mu \geq 0 \tag{3.101}$$

- **Case 1:** It is the unrestricted control which was previously obtained in (3.91) that is only admissible for some x_0 such that:

$$\begin{bmatrix} u(0) \\ u(1) \end{bmatrix} = -\frac{1}{5} \begin{bmatrix} 3 \\ 1 \end{bmatrix} x_0 \qquad -\frac{5}{3} \leq x_0 \leq \frac{5}{3} \tag{3.102}$$

- **Case 2:** It is activated the restriction on control input $u(0) = 1$ and $\mu_1 = \mu_1^*$. Therefore, $u(1)$ can be solved such that:

$$\begin{bmatrix} u(0) \\ u(1) \end{bmatrix} = \begin{bmatrix} 1 \\ -\frac{1+x_0}{2} \end{bmatrix} \qquad \mu_1 = -\frac{5 + 3x_0}{2} \tag{3.103}$$

This case is valid if:

$$\begin{aligned} -1 \leq -\frac{1+x_0}{2} \leq 1 \qquad & \mu_1 \geq 0 \\ -3 \leq x_0 \leq 1 \qquad & x_0 \leq -\frac{5}{3} \end{aligned} \tag{3.104}$$

Then this case is only admissible for some x_0 such that $-3 \leq x_0 \leq -\frac{5}{3}$.

- **Case 3:** It is activated the restriction on control input $u(0) = -1$ and $\mu_2 = \mu_2^*$. Therefore, $u(1)$ can be solved such that:

$$\begin{bmatrix} u(0) \\ u(1) \end{bmatrix} = \begin{bmatrix} -1 \\ \frac{1-x_0}{2} \end{bmatrix} \qquad \mu_2 = -\frac{5 - 3x_0}{2} \tag{3.105}$$

This case is valid if:

$$\begin{aligned} -1 \leq \frac{1-x_0}{2} \leq 1 \qquad & \mu_2 \geq 0 \\ -1 \leq x_0 \leq 3 \qquad & x_0 \geq \frac{5}{3} \end{aligned} \tag{3.106}$$

Then this case is only admissible for some x_0 such that $\frac{5}{3} \leq x_0 \leq 3$.

- **Case 4:** It is activated the restriction on control input $u(1) = 1$ and $\mu_3 = \mu_3^*$. Therefore, $u(0)$ can be solved such that:

$$\begin{bmatrix} u(0) \\ u(1) \end{bmatrix} = \begin{bmatrix} -\frac{1+2x_0}{3} \\ 1 \end{bmatrix} \qquad \mu_3 = -\frac{5+x_0}{3} \tag{3.107}$$

This case is valid if:

$$\begin{aligned} -1 \leq -\frac{1+2x_0}{3} \leq 1 \qquad & \mu_3 \geq 0 \\ -2 \leq x_0 \leq 1 \qquad & x_0 \leq -5 \end{aligned} \tag{3.108}$$

Then, since there is no x_0 to satisfy the KKT conditions, this case is not admissible.

- **Case 5:** It is activated the restrictions on control inputs $u(0) = u(1) = 1$. Therefore, $\mu_1 = \mu_1^*$ and $\mu_3 = \mu_3^*$ are calculated to verify if the case is valid:

$$\begin{aligned} \mu_1 = -2x_0 - 4 \geq 0 \qquad & \mu_3 = -x_0 - 3 \geq 0 \\ x_0 \leq -2 \qquad & x_0 \leq -3 \end{aligned} \tag{3.109}$$

Then this case is only admissible for some x_0 such that $x_0 \leq -3$.

- **Case 6:** It is activated the restrictions on control inputs $u(0) = -1$ and $u(1) = 1$. Therefore, $\mu_2 = \mu_2^*$ and $\mu_3 = \mu_3^*$ are calculated to verify if the case is valid:

$$\begin{aligned} \mu_2 = 2x_0 - 2 \geq 0 \qquad & \mu_3 = -x_0 - 1 \geq 0 \\ x_0 \geq 1 \qquad & x_0 \leq -1 \end{aligned} \tag{3.110}$$

Then, since there is no x_0 to satisfy the KKT conditions, this case is not admissible.

- **Case 7:** It is activated the restrictions on control input $u(1) = -1$ and $\mu_4 = \mu_4^*$. Therefore, $u(0)$ can be solved such that:

$$\begin{bmatrix} u(0) \\ u(1) \end{bmatrix} = \begin{bmatrix} \frac{1-2x_0}{3} \\ -1 \end{bmatrix} \qquad \mu_4 = -\frac{5-x_0}{3} \tag{3.111}$$

This case is valid if:

$$\begin{aligned} -1 \leq \frac{1-2x_0}{3} \leq 1 \qquad & \mu_3 \geq 0 \\ -1 \leq x_0 \leq 2 \qquad & x_0 \geq 5 \end{aligned} \tag{3.112}$$

Then, since there is no x_0 to satisfy the KKT conditions, this case is not admissible.

- **Case 8:** It is activated the restrictions on control inputs $u(0) = 1$ and $u(1) = -1$. Therefore, $\mu_1 = \mu_1^*$ and $\mu_4 = \mu_4^*$ are calculated to verify if the case is valid:

$$\begin{aligned} &\mu_1 = -2 - 2x_0 \geq 0 && \mu_4 = x_0 - 1 \geq 0 \\ &x_0 \leq -1 && x_0 \geq 1 \end{aligned} \tag{3.113}$$

  Then, since there is no x_0 to satisfy the KKT conditions, this case is not admissible.

- **Case 9:** It is activated the restrictions on control inputs $u(0) = -1$ and $u(1) = -1$. Therefore, $\mu_2 = \mu_2^*$ and $\mu_4 = \mu_4^*$ are calculated to verify if the case is valid:

$$\begin{aligned} &\mu_2 = -4 + 2x_0 \geq 0 && \mu_4 = -3 + x_0 \geq 0 \\ &x_0 \geq 2 && x_0 \geq 3 \end{aligned} \tag{3.114}$$

  Then this case is only admissible for some x_0 such that $x_0 \geq 3$.

Finally, for this constrained Optimal Control Problem (OCP), only five cases are truly valid, as depicted in Table 3.4.

Table 3.4: Final valid cases with KKT conditions with $N = 2$ for (3.95)

Case	μ_1	μ_2	μ_3	μ_4	$u(0)$	$u(1)$
1	0	0	0	0	$-3x_0/5$	$-x_0/5$
2	μ_1^*	0	0	0	1	$(1 + x_0)/2$
3	0	μ_2^*	0	0	-1	$(1 - x_0)/2$
5	μ_1^*	0	μ_3^*	0	1	1
9	0	μ_2^*	0	μ_4^*	-1	-1

Furthermore, the control input depends on x_0 such that:

$$u(0) = \begin{cases} 1 & , \ x_0 < -\frac{5}{3} \\ -\frac{3}{5}x_0 & , \ -\frac{5}{3} \leq x_0 \leq \frac{5}{3} \\ -1 & , \ \frac{5}{3} < x_0 \end{cases} \qquad u(1) = \begin{cases} 1 & , \ x_0 < -3 \\ -\frac{1+x_0}{2} & , \ -3 \leq x_0 < -\frac{5}{3} \\ -\frac{1}{5}x_0 & , \ -\frac{5}{3} \leq x_0 < \frac{5}{3} \\ \frac{1-x_0}{2} & , \ \frac{5}{3} \leq x_0 \leq 3 \\ -1 & , \ 3 < x_0 \end{cases} \tag{3.115}$$

In Fig. 3.8, the control inputs are shown as functions of x_0. In this simple example, the dependence between the initial condition and the Model Predictive Control (MPC) control input $u(0)$ is evident. It can be observed that the relationship is initially linear and then saturates. However, for more complex problems, it may be necessary to control each interval of the initial condition differently, as observed in $u(1)$.

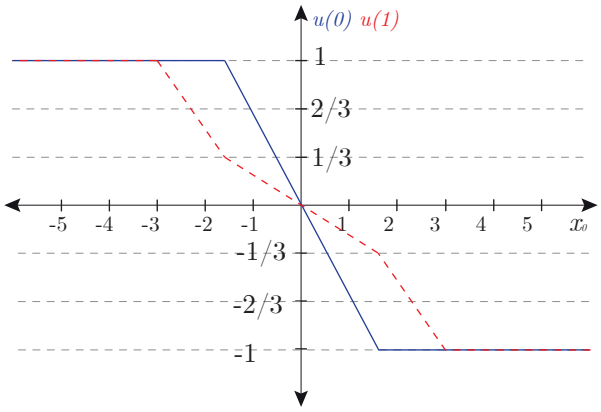

Figure 3.8: Optimal inputs depending on initial conditions for constrained OCP

By applying this MPC control law to the system with different initial conditions, it is possible to verify that after a certain number of steps, the state $x(k)$ can be regulated to 0. Fig. 3.9 illustrates the operation of the system with MPC control, with and without considering the input constraints for $x_0 = -5$ and $x_0 = 8$. Inputs u_1 and u_2 are limited between -1 and 1, and therefore it takes more steps for the state x to reach 0.

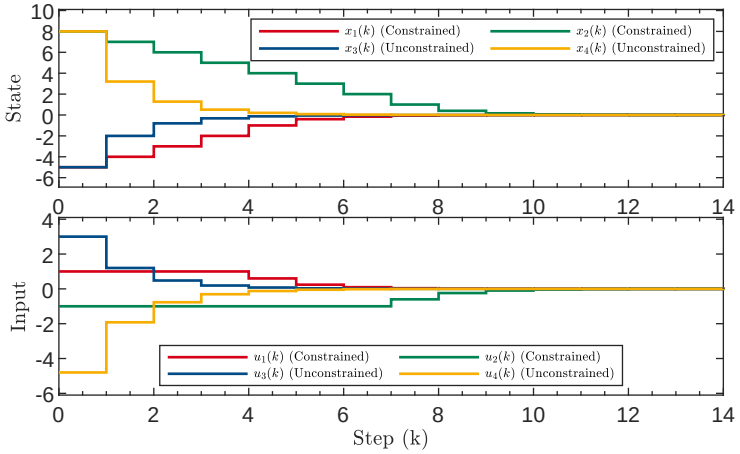

Figure 3.9: Comparison between unconstrained and constrained MPC.

In this example, the control law has been explicitly elucidated. Nonetheless, an alternative approach involves solving the problem through the inversion of matrices, which dynamically change based on the activation of constraints. Another numerical method is the utilization of Newton's method for nonlinear systems of equations. Therefore, the choice of the optimal solution-finding method must take into account the complexity of the OCP [96].

3.2 Simple MPC for DC-DC converters

As discussed in Chapter 2, converters can be modeled as Bilinear Systems with the structure from Eq. (2.2). Therefore, a simple MPC problem can be proposed with the structure of Eq. (3.116), such that state and input constraints are considered.

$$\min_{\underline{u}} \; J_N(x, \underline{u}) = J_f(x(N)) + \sum_{k=0}^{N-1} l(x(k), u(k)) \tag{3.116a}$$

$$\text{s.t. } x(k+1) = f(x(k), u(k)) \;,\; k \in [0, N-1] \tag{3.116b}$$

$$x(k) \in \mathbb{X} \tag{3.116c}$$

$$u(k) \in \mathbb{U} \tag{3.116d}$$

Here, the cost function J_N combines a terminal cost function $J_f(x(N))$ and a cumulative sum of stage costs $l(x(k), u(k))$ over the prediction horizon. The dynamics of the system are captured by the equality constraint $x(k+1) = f(x(k), u(k))$ for each time step within the horizon. The state $x(k)$ is constrained to the set $\mathbb{X}$, and the control input $u(k)$ is constrained to the set $\mathbb{U}$. This formulation represents a generic Model Predictive Control (MPC) optimization problem that seeks to minimize a predefined cost while satisfying the system dynamics and input constraints over a finite prediction horizon. A cost function defined to minimize the quadratic error between the states and their references and considering state restrictions such as current and duty cycle constraints is presented in Eq. (3.117).

$$\min_{u(k)} \; J_N(x(k), u(k)) = \frac{1}{2} \sum_{k=1}^{N} \left[(x(k) - x_{ref}(k))^T P (x(k) - x_{ref}(k)) \right] \tag{3.117a}$$

$$s.t. \; x(k+1) = f(x(k), u(k)) \tag{3.117b}$$

$$x_{min} \leq x(k) \leq x_{max} \tag{3.117c}$$

$$u_{min} \leq u(k) \leq u_{max} \tag{3.117d}$$

3.2.1 Optimization problems

A prediction horizon $N = 2$ is proposed for the electrical subsystem in (2.24a)-(2.24b) and the thermal subsystem in (2.86), where a cost function is defined to minimize the error between the states and their references. This controller allows to optimally consider the restrictions of the state variables and input signals duty cycle d for the electrical subsystem and the switching frequency f_{sw} for the thermal subsystem. In turn, it allows the control law to be explicitly derived by using the KKT conditions. If the prediction horizon was increased, the cases to be evaluated would increase exponentially as well as the mathematical complexity. Therefore, it is not necessary to use a solver for the optimization problem which would critically limit the maximum sampling frequency due to the computational burden.

Since there are two relevant subsystems, the electrical and the thermal ones, two separated optimization problems are considered. The two problems to be optimized have the following

structure: (i) the MPC optimization problem for electrical model is formulated as follows:

$$\min_{d(0),d(1)} \quad J_{I2} = \frac{1}{2}\left((i_L(2) - i_{L,ref})^2 + (i_L(3) - i_{L,ref})^2\right) \tag{3.118a}$$

$$s.t.\ i_L(k+2) = a_1 i_L(k+1) + a_2 v_o(k+1) + (a_3 i_L(k+1) + a_4) d(k) \tag{3.118b}$$

$$v_o(k+2) = a_5 i_L(k+1) + a_6 v_o(k+1) \tag{3.118c}$$

$$0 \leq d(k) \leq 1, \tag{3.118d}$$

and (ii) the MPC optimization problem for thermal model and ATC implementation is formulated by

$$\min_{f_{sw}(k)} \quad J_{T2} = \frac{1}{2}\left((T(2) - T_{ref})^2 + (T(3) - T_{ref})^2\right) \tag{3.119a}$$

$$s.t.\ T(k+2) = b_1 T(k+1) + b_2 f_{sw}(k) + b_3 \tag{3.119b}$$

$$f_{sw,min} \leq f_{sw}(k) = f_{s,i} \cdot \text{floor}\left(\frac{f_{sw}(k)}{f_{s,i}}\right) \leq f_{sw,max}, \tag{3.119c}$$

Where the temperature measurement is carried out as follows

$$T_m(k) = \max\{T_{j1}(k), T_{j2}(k)\} \tag{3.120a}$$

$$\omega(0) = T_m(0) - \ b_1 T_m(-1) - b_2 f_{sw}(-1) - b_3 \tag{3.120b}$$

$$T(0) = T_m(0) + 1.5\ \omega(0) \tag{3.120c}$$

By incorporating this adjustment into the measurement, certain steady-state errors due to perturbation, measurement noise, and modeling errors are concentrated in $\omega(k)$, and can be mitigated using prior measurements and model prediction. However, it is important to note that this compensation is limited and does not guarantee stability in all cases. This compensation is necessary because there are several uncertainties in the model, in addition there may be certain non-measurable disturbances. Note that, duty cycle and switching frequency actuation are limited to $[0, 1]$ and $[f_{min}, f_{min}]$, respectively. Then, a prediction horizon $N = 2$ is sufficient for the closed-loop system to be stable since the input is limited to values where the system is stable.

3.2.2 Evaluation of KKT conditions

To find the optimal solutions to the optimization problems (3.118)-(3.119), the following KKT conditions must be fulfilled, which are shown below for the electrical model

$$\begin{aligned} &\frac{\partial J_{I2}}{\partial d(0)} - \lambda_1 + \lambda_2 = 0 && \frac{\partial J_{I2}}{\partial d(1)} - \lambda_3 + \lambda_4 = 0 \\ &\lambda_1(d_{min} - d(0)) = 0 && \lambda_3(d_{min} - d(1)) = 0 \\ &\lambda_2(d(0) - d_{max}) = 0 && \lambda_4(d(1) - d_{max}) = 0 \end{aligned} \tag{3.121}$$

Since λ_1, λ_2 and λ_3, λ_4 cannot be activated at the same time, it is simple to solve the equations for each case. For example, when activating the constraint λ_1, its value must be calculated and evaluated to be positive, while λ_2 is 0. Hence,

$$\lambda_1^* = \frac{\partial J_{I2}}{\partial d(0)} \qquad \lambda_2^* = -\frac{\partial J_{I2}}{\partial d(0)} \qquad \lambda_3^* = \frac{\partial J_{I2}}{\partial d(1)} \qquad \lambda_4^* = -\frac{\partial J_{I2}}{\partial d(1)} \tag{3.122}$$

After calculating the duty cycles in each case, the KKT conditions must be evaluated. For this, it is necessary to evaluate the derivatives of the current cost function J_{I2} with respect to $d(1)$ and $d(0)$, thus:

$$\frac{\partial J_{I2}}{\partial d(0)} = (i_L(2) - i_{L,ref})(a_3 i_L(1) + a_4) + (i_L(3) - i_{L,ref})(a_3 i_L(1) + a_4)(a_1 + a_3 d(1)) \tag{3.123}$$

$$\frac{\partial J_{I2}}{\partial d(1)} = (i_L(3) - i_{L,ref})(a_3 i_L(2) + a_4) \tag{3.124}$$

And in the optimization problem the thermal model (3.119) the derivatives of J_{T2} with respect to $f_{sw}(1)$ and $f_{sw}(0)$ are:

$$\frac{\partial J_{T2}}{\partial f_{sw}(0)} = (T(2) - T_{ref})b_2 + (T(3) - T_{ref})b_1 b_2 \tag{3.125}$$

$$\frac{\partial J_{T2}}{\partial f_{sw}(1)} = (T(3) - T_{ref})b_2 \tag{3.126}$$

In addition, it must be verified that the calculated duty cycles satisfy the constraints in (3.118d) and the switching frequency satisfy the constraints in (3.119c). Since, in the proposed ATC loop, the resulting switching frequency reference f_{sw}^* is quantized as multiples of the current sampling frequency $f_{s,i} = 1/T_{s,i}$, the integers closest to the calculated switching frequency must be evaluated within the cost function J_{T2}. The one that generates the lowest value is applied. For instance, if the calculated switching frequency is 375.27kHz, the frequencies 370kHz and 380kHz are evaluated within the cost function.

With KKT conditions (3.121) there are $2^4 = 16$ cases, which are shown in Tab. 3.5.

Table 3.5: Possible cases of CCS-MPC with N=2 for (3.118)

Case	λ_1	λ_2	λ_3	λ_4	$d(0)$	$d(1)$
1	0	0	0	0	$d_1(0)$	$d_1(1)$
2	λ_1^*	0	0	0	d_{min}	$d_1(1)$
3	0	λ_2^*	0	0	d_{max}	$d_1(1)$
4	λ_1^*	λ_2^*	0	0	–	$d_1(1)$
5	0	0	λ_3^*	0	$d_2(0)$	d_{min}
6	λ_1^*	0	λ_3^*	0	d_{min}	d_{min}
7	0	λ_2^*	λ_3^*	0	d_{max}	d_{min}
8	λ_1^*	λ_2^*	λ_3^*	0	–	d_{min}
9	0	0	0	λ_4^*	$d_2(0)$	d_{max}
10	λ_1^*	0	0	λ_4^*	d_{min}	d_{min}
11	0	λ_2^*	0	λ_4^*	d_{max}	d_{min}
12	λ_1^*	λ_2^*	0	λ_4^*	–	d_{min}
13	0	0	λ_3^*	λ_4^*	–	–
14	λ_1^*	0	λ_3^*	λ_4^*	d_{min}	–
15	0	λ_2^*	λ_3^*	λ_4^*	d_{max}	–
16	λ_1^*	λ_2^*	λ_3^*	λ_4^*	–	–

However, not all cases are feasible due to input restrictions, where the duty cycle cannot be $d_{min} = 0$ and $d_{max} = 1$ at the same time, as in cases 4, 8 and 12-16 . In Tab. 3.6, only the feasible cases are detailed.

Table 3.6: Feasible cases of CCS-MPC with N=2 for (3.118)

Case	λ_1	λ_2	λ_3	λ_4	$d(0)$	$d(1)$
1	0	0	0	0	$d_1(0)$	$d_1(1)$
2	λ_1^*	0	0	0	d_{min}	$d_1(1)$
3	0	λ_2^*	0	0	d_{max}	$d_1(1)$
4	0	0	λ_3^*	0	$d_2(0)$	d_{min}
5	λ_1^*	0	λ_3^*	0	d_{min}	d_{min}
6	0	λ_2^*	λ_3^*	0	d_{max}	d_{min}
8	0	0	0	λ_4^*	$d_2(0)$	d_{max}
9	λ_1^*	0	0	λ_4^*	d_{min}	d_{max}
10	0	λ_2^*	0	λ_4^*	d_{max}	d_{max}

The duty cycles $d_1(0)$, $d_1(1)$ and $d_2(0)$, and frequencies $f_{sw,1}(0)$, $f_{sw,1}(1)$ and $f_{sw,2}(0)$ calculated explicitly from the predictions are shown in the next subsection.

3.2.3 Explicit control law

Tab. 3.6 details the KKT multipliers and the possible cases to be tested in the algorithm to find the optimal actuation solution. The unrestricted control input $d_1(k)$ for $k \in \{0,1\}$ in (3.118) is

$$d_1(k) = \frac{i_{L,ref} - a_1 i_L(k) - a_2 v_o(k)}{a_3 i_L(k) + a_4} \tag{3.127}$$

When the constraint of $d(1)$ is predicted to be used, the duty cycle $d(0)$ to be applied to the converter is calculated with $d_2(0)$

$$d_2(0) = \frac{i_{pred} - a_1 i_L(0) - a_2 v_o(0)}{a_3 i_L(0) + a_4} \tag{3.128}$$

with i_{pred} is defined as:

$$i_{pred} = \frac{i_{L,ref} + (i_{L,ref} - a_2 v_o(1) - a_4 d(1))(a_1 + a_3 d(1))}{(1 + a_1 + a_3 d(1))(a_1 + a_3 d(1))} \tag{3.129}$$

and $d(1)$ and $d(0)$ are defined in Tab. 3.6. In an analogous way the unrestricted control input $f_{sw,1}(k)$ for $k \in \{0,1\}$ in (3.119) is

$$f_{sw,1}(k) = \frac{T_{ref} - b_1 T(k) - b_3}{b_2} \tag{3.130}$$

When the constraint of $f_{sw}(1)$ is predicted to be used, the switching frequency $f_{sw}(0)$ to be applied to the converter is calculated with $f_{sw,2}(0)$

$$f_{sw,2}(0) = \frac{T_{pred} - b_1 T(0) - b_3}{b_2} \tag{3.131}$$

with T_{pred} is defined as:

$$T_{pred} = \frac{T_{ref} + (T_{ref} - b_2 f_{sw}(1) - b_3) b_1}{1 + b_1^2} \tag{3.132}$$

3.3 Proposed control strategy

The proposed algorithm is executed as shown in Fig. 3.10. First with the measurements the parameters of the model are calculated. Then, case 1 is evaluated where input control signals must fullfield their constraints to be valid. If they are not valid then next case is evaluated activating the restrictions of input control signals and cost function derivatives are evaluated to check if KKT conditions are fulfilled. Since the proposed problems are QP there is always an optimal solution.

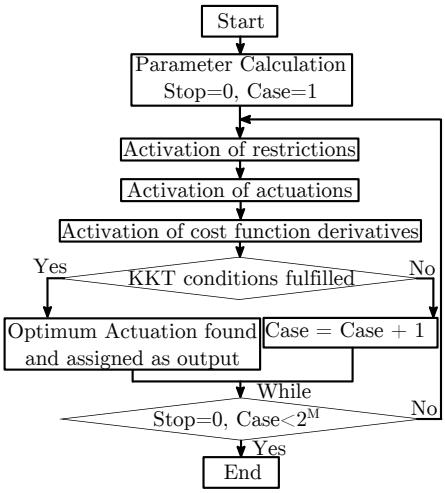

Figure 3.10: Optimization based on KKT conditions.

The comprehensive control scheme is depicted in Fig. 3.11, where the control loops for junction temperature and current are designed to be dynamically decoupled. Temperature control is achieved through the switching frequency f_{sw}, while current is controlled by adjusting the duty cycle d of the switching signal S.

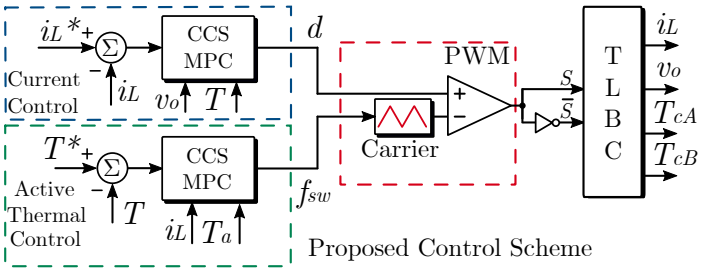

Figure 3.11: Proposed control scheme based on CCS-MPC controllers with ATC for a Two-Level Buck Converter (TLBC).

During simulations, the junction temperature is computed using the loss model based on datasheet information. However, in practical experimental scenarios, this temperature is approximated with the case temperature measured directly.

3.3.1 PI controller design

Properly tuned PI controllers with anti-windup give very similar current control responses as MPC controllers. However, dynamic response can be optimally improved with CCS-MPC. To compare the proposed designed CCS-MPC control law, the following PI controller designs are briefly included. To design the current controller, the transfer function $G_i(s)$ between the current i_L and the duty cycle d is considered such that the conduction resistances are equal, that is, $R_{DS,A} = R_{DS,B} = R_{on}$.

$$G_i(s) = V_{dc}\frac{sR_oC + 1}{s^2LCR_o + s(L + R_oC(R_{on} + r_L)) + R_o + R_{on} + r_L} \tag{3.133}$$

However, there is a better way to control the inductor current using feedforward such that from LVK equation:

$$L\frac{d}{dt}i_L = -(R_{on} + r_L)i_L - V_o + V_c \tag{3.134}$$

The converter voltage V_c applied can be separated in two terms such that:

$$V_c = V_{c,PI} + V_o \tag{3.135}$$

Subsequently, the transfer function $H_i(s)$ can be employed to adjust the PI controller.

$$L\frac{d}{dt}i_L + (R_{on} + r_L)i_L = V_{c,PI} \qquad \longrightarrow \qquad H_i(s) = \frac{1}{sL + R_{on} + r_L} \tag{3.136}$$

The duty cycle can be calculated such that:

$$d = \frac{V_{c,PI} + V_o}{V_{dc}} \tag{3.137}$$

For the voltage control LCK equation is considered assuming that inductor current i_L can be controlled faster than voltage such that v_o can be controlled with the reference i_L^* and the measurement or estimation of i_o such that:

$$C\frac{d}{dt}v_o = i_L^* - i_o \qquad \rightarrow \qquad H_v(s) = \frac{1}{sC} \tag{3.138}$$

The various control structures described above are depicted in Fig. 3.12. To fine-tune the PI temperature controller, the transfer function $G_t(s)$ in Eq. 2.83 is utilized.

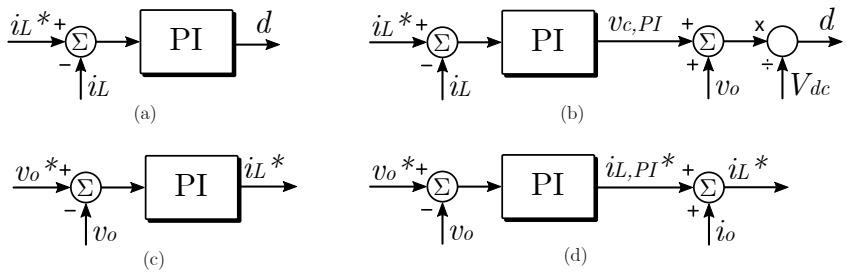

Figure 3.12: Control structures with PI controllers for (a) current control without feedforward, (b) current control with feedforward, (c) voltage control without feedforward and (d) voltage control with feedforward.

Finally, an anti-windup scheme shown in Fig. 3.1 from [97] is implemented to limit the duty cycle and switching frequency. Fig. 3.13 illustrates the conventional cascade control scheme, where either current or voltage control can be implemented.

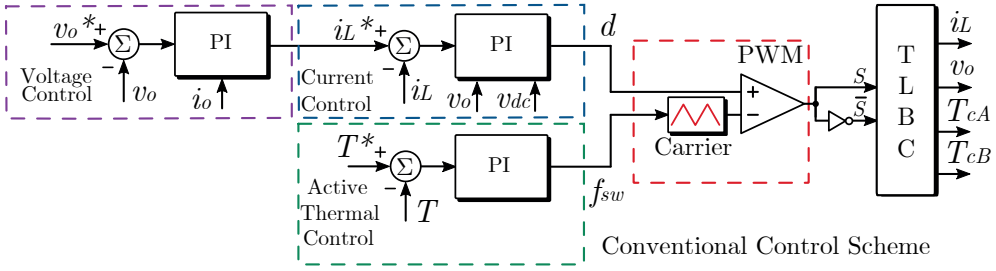

Figure 3.13: Conventional cascade control scheme based on PI controllers with ATC for a Two-Level Buck Converter (TLBC).

3.3.2 Summary

This chapter introduces both basic and advanced concepts of predictive control, proposing a control strategy to regulate the inductor current and temperature of GaN devices. In the subsequent chapter, the system response with conventional PI controllers is simulated and compared to the proposed control strategy based on CCS-MPC. It is anticipated that the CCS-MPC approach will exhibit a faster dynamic response.

Chapter 4

SIMULATION RESULTS

4.1 Introduction

THE implmentation of proposed control in simulation it is shown in the following chapter. An EV powertrain system is initially simulated to showcase the practical application of the research. Subsequently, the experimental setup system is presented, allowing simulations to run concurrently with experiments for validation purposes.

4.2 EV Powertrain system

The TLBC DC-DC converter and the proposed control system are simulated in PLECS 4.7.3. The system is simulated by using the parameters listed in Tab. 4.1. The PI current controller is designed without feedforward structure, see Fig. 3.12, where the expected overshoot is 1% and the bandwidth BW is 2 kHz which yields the discrete gains $K_{pi} = 4.0897 \cdot 10^{-3}$ and $K_{ii} = 2.2281 \cdot 10^{-3}$. The PI thermal controller is designed with an overshoot of 5% and 50Hz bandwidth using the transfer function $G_t(s)$ obtaining $K_{pt} = 10027.18$ and $K_{it} = 6116.82$.

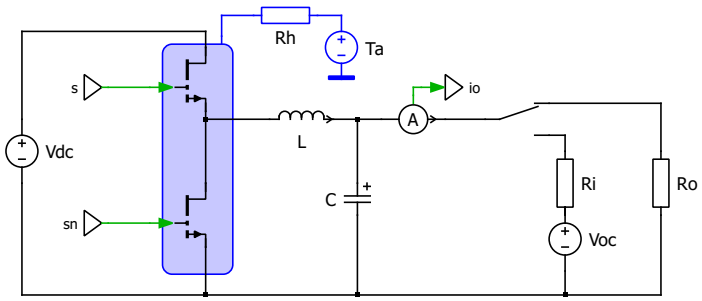

Figure 4.1: EV powertrain system in PLECS.

To simulate the constant-current charging (CCC) of a battery, an internal resistance R_i and an ideal voltage source with open circuit voltage v_{oc} parameters in Tab. 4.1 are used.

Table 4.1: Main parameters of simulated EV powertrain system.

Symbol	Parameter	Value
V_{dc}	DC link voltage	600 V
L	Converter Inductance	1 mH
C	Converter Capacitance	100 μF
R_o	Load resistance	10 Ω
v_{oc}	Open circuit voltage of battery	100 V
R_i	Internal resistance of battery	1 $m\Omega$
$f_{s,i}$	Sampling frequency for current	10 kHz
$f_{s,T}$	Sampling frequency for temperature	100 Hz
R_h	Heatsink thermal resistance	1 $°C/W$
C_h	Heatsink thermal capacitance	10m$Ws/°C$
K_{th}	Thermal gain of model	$2.6212 \cdot 10^{-4}$ $°Cs$
τ_{th}	Thermal time constant of model	0.0252 s
T_1	Temperature of model	39.4965$°C$
f_{sw1}	Switching frequency of model	50 kHz
$f_{sw,min}$	Minimum switching frequency	50 kHz
$f_{sw,max}$	Maximum switching frequency	500 kHz
$f_{sw,nom}$	Nominal switching frequency	200 kHz

Fig. 4.2 illustrate different scenarios for the approximate thermal system (2.84), categorized as follows:

- Case 1: System without disturbance and no modeling errors.
- Case 2: System with a constant disturbance at the junction temperature of 20°C and no modeling errors.
- Case 3: System with a constant disturbance in the junction temperature of −20°C and no modeling errors.
- Case 4: System without perturbation and with modeling error $K_{th}^{real} = 1.5K_{th}$ and $\tau_{th}^{real} = 1.4\tau_{th}$.
- Case 5: System without perturbation and with modeling error $K_{th}^{real} = 1.1K_{th}$ and $\tau_{th}^{real} = 0.9\tau_{th}$.

Where the junction temperature and switching frequency for case n is $T_{j,n}$ and $f_{sw,n}$. In Fig. 4.2.a the compensation proposed in equation (3.120) is not used, showing that the junction temperature does not correctly reach the reference $T_{ref} = 70°C$ in any case due to stationary errors. While in Fig. 4.2.b compensation is applied, always managing to reach the reference temperature $T_{ref} = 70°C$. However, it is observed that having a considerable modeling error makes the transient dynamics of the MPC worse.

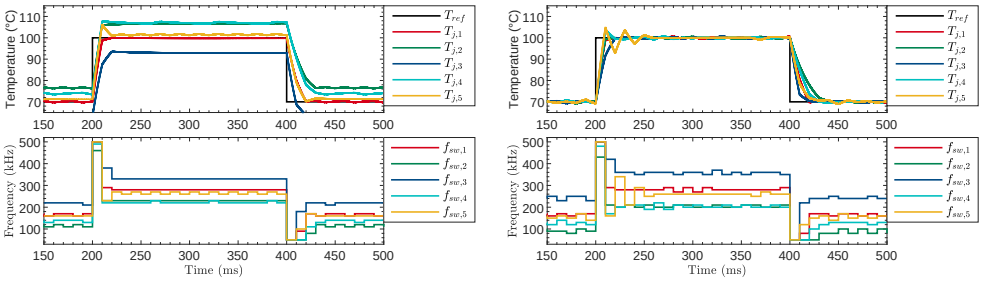

(a) Without compensation (b) With compensation

Figure 4.2: Simulation results of the proposed ATC loop with and without compensation from (3.120) for cases of modeling errors and disturbances.

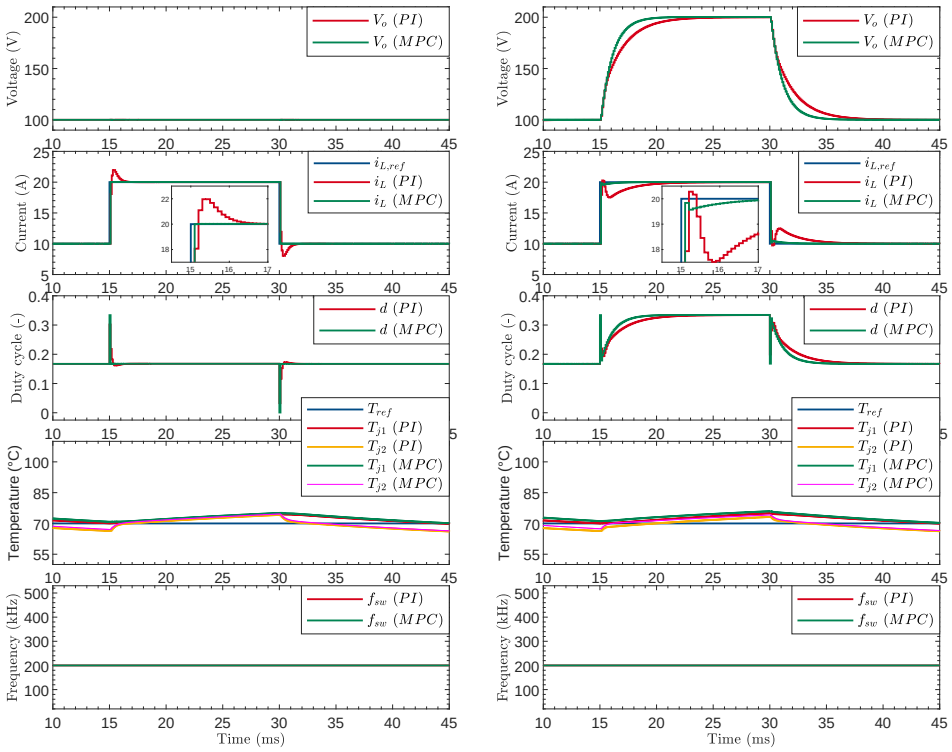

(a) Battery as load (b) R_o load

Figure 4.3: Simulation results of the proposed current control.

Dynamic simulation results are included in Fig. 4.3 with a comparison between conventional PI and CCS-MPC, where the current control loop has a good regulation decoupled from the

temperature reference at $T_{ref} = 70°C$. Thus, the switching frequency is fixed at $f_{sw,nom} = 200$kHz. It is shown in Fig. 4.3.a that the PI controller changes similar to the behavior of the CCS-MPC but it has a current overshoot.

In Fig. 4.3.b a simple R_o load is simulated to evaluate the load voltage dynamic. Here, the PI controller takes a longer time to reach its current reference and it has a current undershoot. CCS-MPC has a faster load voltage regulation and decoupled from $T_{ref} = 70°C$. Note that, both semiconductors have very similar temperatures and the switching frequency is still fixed and imposed at $f_{sw,nom} = 200$kHz.

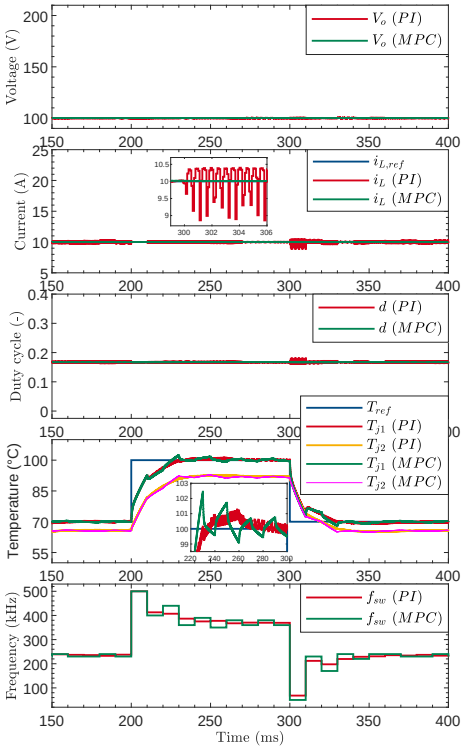

Figure 4.4: Simulation results of the proposed ATC loop with R_o load.

Finally, in Fig. 4.4 are presented ATC dynamic results with CCS-MPC and PI controllers under a fixed current reference of 10A, but by increasing the desired junction temperature reference from $T_{ref} = 70°C$ to $T_{ref} = 100°C$ and reducing then to $T_{ref} = 70°C$. The time scale is scaled down to milliseconds for computational efficiency but should be understood as representing minutes in practical terms. As a result, the temperature T_{j1} is superior than T_{j2} due to the buck operation. The PI controller saturates on maximum actuation similar to the behavior of the CCS-MPC. Note that, the current loop is quasi-decoupled from the temperature results and the switching frequency is adjusted to be quantized in multiples of sampling frequency from 220kHz to 360kHz and then to 220kHz according to T_{ref} steps. Hence, in experimental applications, it becomes imperative to quantize the frequencies produced by the PI controller to mitigate sampling errors.

4.3 Simulation with detailed experimental setup system

Figure 4.5 illustrates the schematic of the experimental system in PLECS, which will be used in parallel with the real system. In this simulation, factors such as implementation delay, dead time in switching signals, parasitic resistances, and the influence of temperature on the conduction resistances of GaN are taken into account. The parameters for the GaN electrical model are extracted from the datasheet. The diode's blocking voltage is configured at 4.6V, and the reverse conduction resistance is set to 92mΩ. The series resistance R_s of the DC source is approximated to 1 mΩ to prevent short circuits. The parasitic resistance of the inductor r_L is measured to be 140 mΩ, while the DC-link capacitance C_{dc} is set to 440 μF. The load resistance R_o is adjusted accordingly for each experiment.

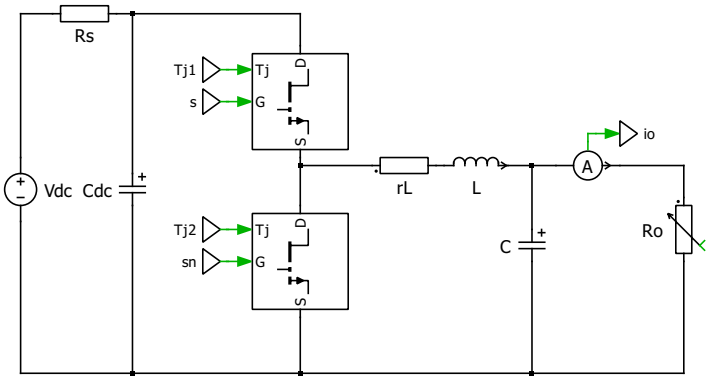

(a) TLBC schematic

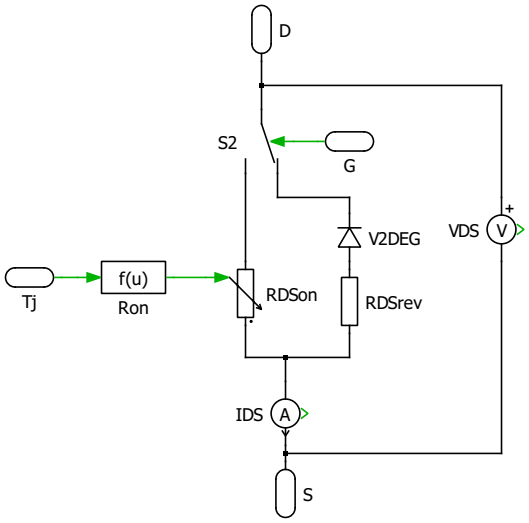

(b) GaN device model electrical schematic

Figure 4.5: Experimental setup system in PLECS.

Chapter 5

EXPERIMENTAL VERIFICATION

5.1 Introduction

APPLICATION of the CCS-MPC in Power Electronics has been tested and proven both theoretically and experimentally in the recent years. However, not for DC-DC GaN-based Converters with ATC scheme. The above chapters point out modeling and control along with simulations that verify proposed control, but experimental results are utilized to prove the effectiveness and usefulness of the proposed control strategy.

5.2 Set-Up

The proposed strategy has been tested on an experimental rig, composed by a GaN semiconductor halfbridge, a LC filter, a configurable load resistance and a bidirectional DC source power supply. The experimental setup diagram is presented in Fig. 5.1.a with Human Machine Interface (HMI) and their interaction with the MicroLabBox, while Fig. 5.1.b shows a photography of the mounted experimental rig. Basically, the experimental bench presented in Fig. 5.1.b is composed by

1. Oscilloscope InfiniiVision MSO-X-3024A
2. MicroLabBox dSPACE 1202 control plataform
3. DC Source Power Supply Rigol DP2031
4. Arduino UNO
5. Motherboard GaN Systems GSP65MB-EVB with IMS evaluation module GSP65R25HB-EVB
6. IR sensors GY-906
7. LC filter
8. Isolated Voltage and Current Sensing Module USM-3IV
9. DC Source Power Supply Chroma 62120D-1200

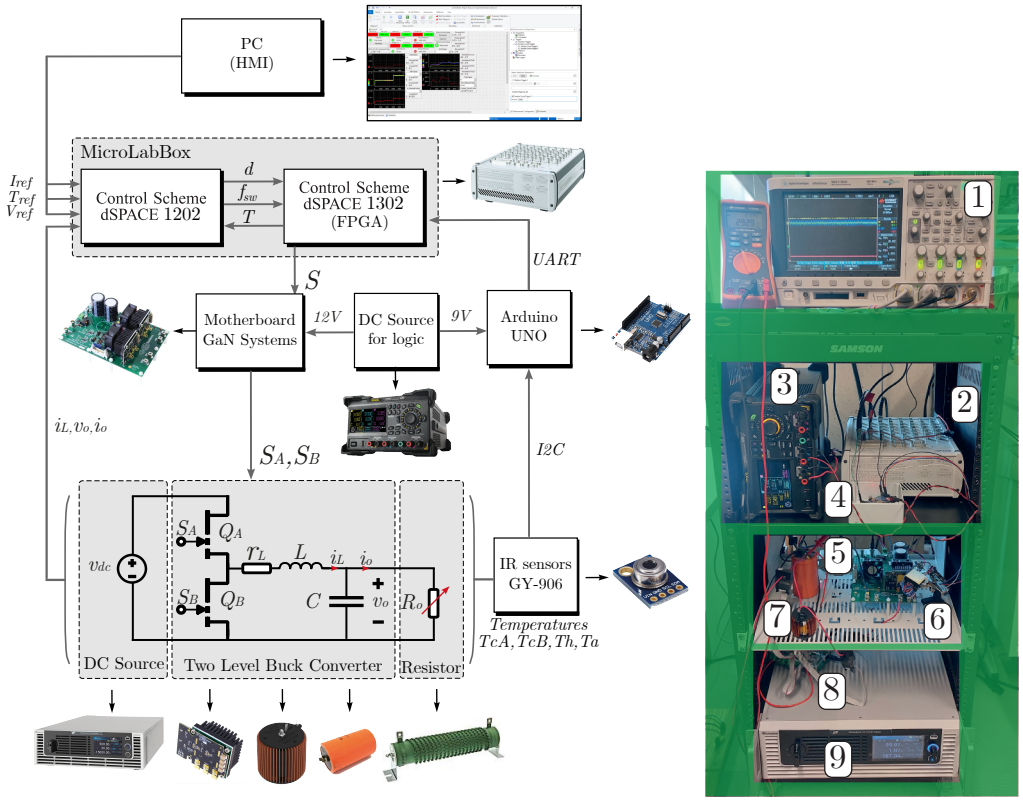

(a) Diagram

(b) Rig

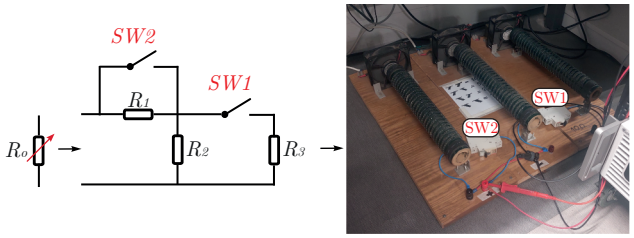

(c) Configurable load resistance

Figure 5.1: Experimental set-up.

In Fig. 5.1(c), a configurable load resistance is illustrated, consisting of three 10Ω resistances, each equipped with its respective fan for cooling, and two switches. The available configurable values for the resistive load are listed in Tab. 5.1.

Table 5.1: Configurable load resistance values

SW1	0	0	1	1
SW2	0	1	0	1
R_o	20 Ω	10 Ω	15 Ω	5 Ω

5.2.1 HMI

The implemented Human-Machine Interface (HMI) is developed using dSPACE ControlDesk software, as shown in Fig. 5.2. In the graphical area, various variables are plotted, including:

- In v, the output voltage v_o with its reference V_{ref}.
- In i, the inductor current i_L with its reference I_{ref}, output current i_o, and estimated inductor current i_{Lo}.
- In d, the duty cycle.
- In T, the case temperatures T_{cA} and T_{cB}, heatsink temperature T_h, ambient temperature T_a and temperature reference T_{ref}.
- In f_{sw}, the switching frequency.

In the button panel are implemented the software trips, manual trip, controller states and the references. There are six inputs, DC-Link voltage V_{DC}, voltage reference V_{ref}, current reference I_{ref}, manual duty cycle d_{manual}, manual switching frequency $f_{sw,manual}$ and temperature reference T_{ref}. The controller states are five: PI and MPC controller for current control, PI controller for voltage control and PI and MPC controller for temperature control. Finally, the trigger panel is used for synchronization with a determined variable and data capture settings. To save the measured data, the "Save Buffer" option is utilized, allowing the data displayed on the screen to be saved and exported in ".mat" files.

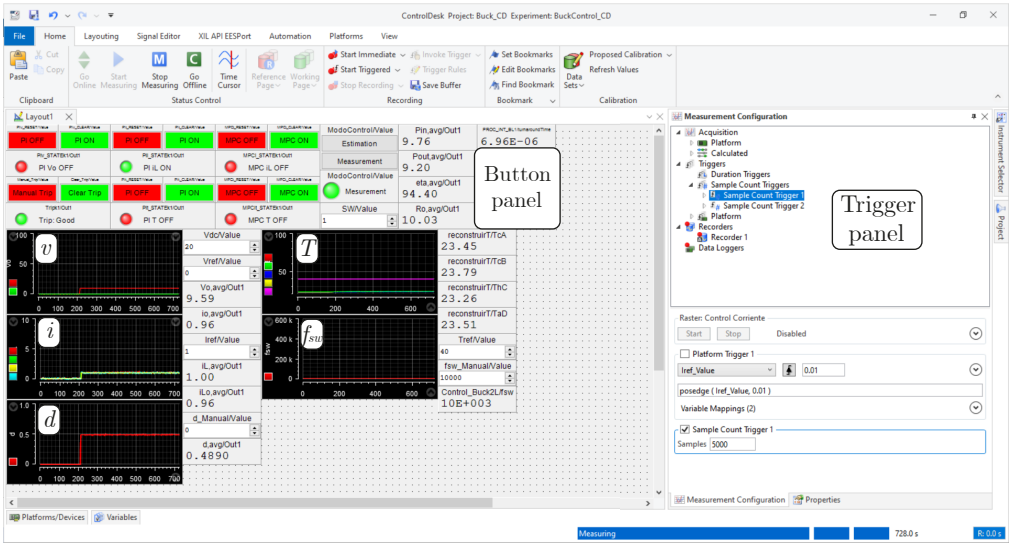

Figure 5.2: Human Machine Interface.

5.2.2 MicroLabBox dSPACE 1202

The control platform utilized is a dSPACE DS1202. Control strategies are implemented in Simulink/MATLAB, as depicted in Fig. 5.4. The Human-Machine Interface (HMI) is developed using ControlDesk software. The MicroLabBox (MLBX) is connected to a desktop computer through an Ethernet cable. The control panel unit facilitates the connection of input and output signals, both analog and digital.

Internally, the platform is partitioned into DS1202 modules, controlled by a Freescale QorIQ P5020 64-bit real-time processor (DualCore@2GHz), and DS1302, driven by a Xilinx Kintex-7 XC7K325T FPGA. Fig. 5.3(b) provides a diagram illustrating the internal structure, showcasing that both modules communicate through a 32-bit wide local bus.

(a) MicroLabBox platform

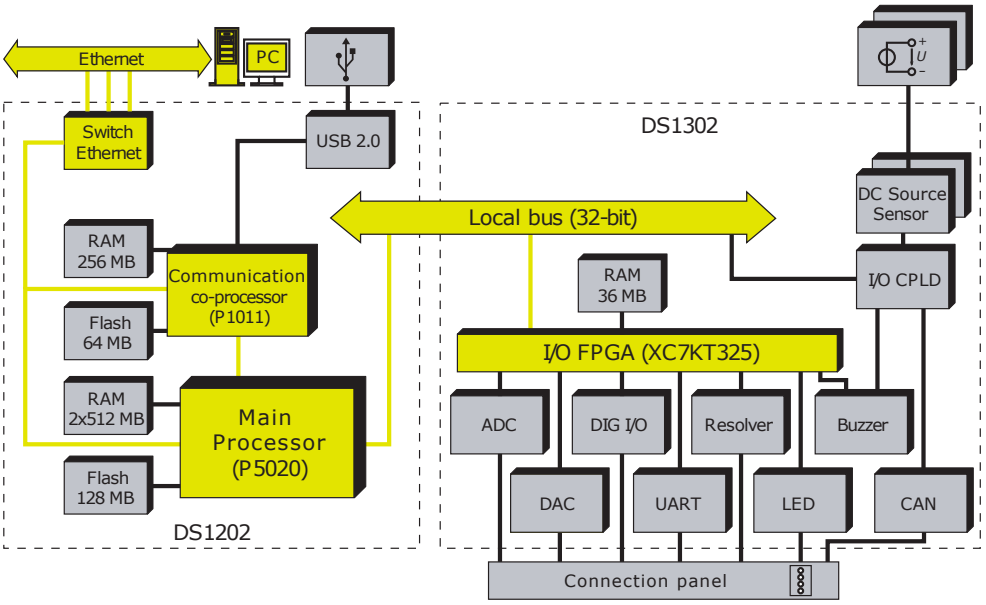

(b) MicroLabBox block diagram

Figure 5.3: MicroLabBox dSPACE 1202.

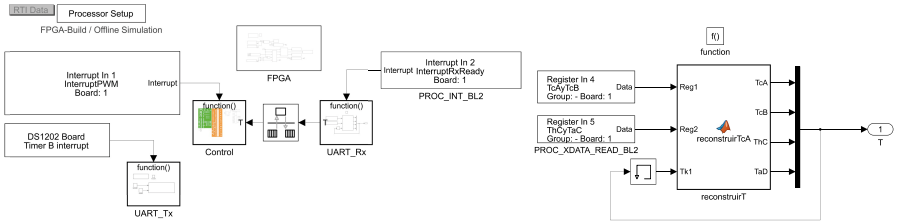

(a) Systems with interrupt and communication blocks

(b) Reconstruction of temperatures from FPGA registers.

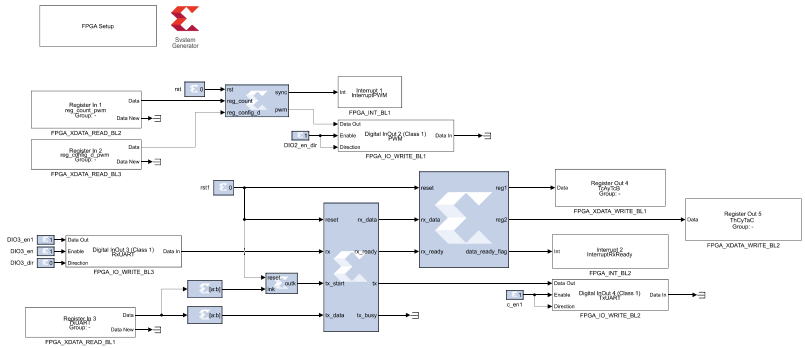

(c) FPGA programming with black box blocks

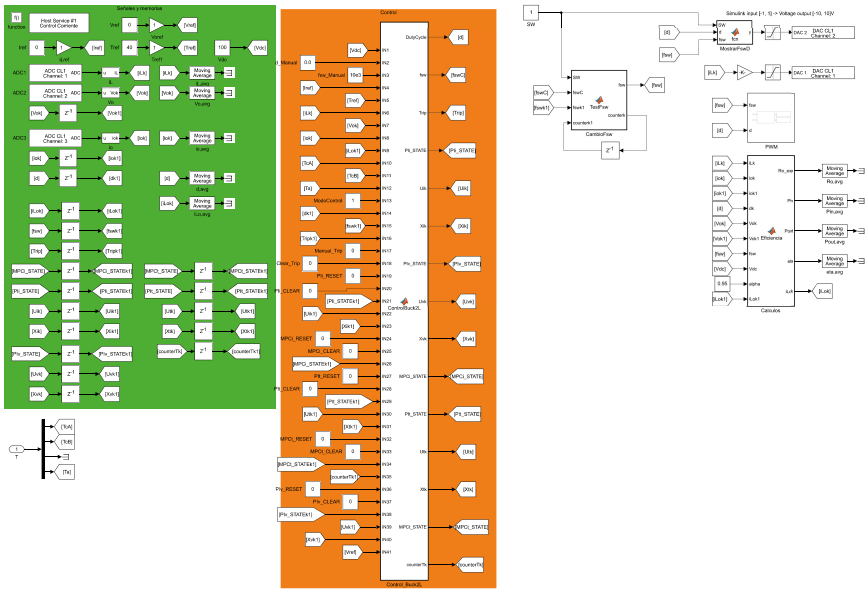

(d) Implementation of control algorithms and configuration of variables in HMI

Figure 5.4: Control system programmed in simulink with blocks.

Thanks to the flexibility of the Field Programmable Gate Array (FPGA), personalized control over the MLBX peripherals is achievable, allowing programming of the modules using various software. For the DS1202 module, Simulink or the C language can be employed, while for the DS1302 module, programming options include Simulink or Verilog.

In this work, a PWM generation module with a variable switching frequency was implemented on the FPGA using event counters, where a triangular signal resets to its minimum. This approach results in the generation of a triangular waveform with a switching frequency f_{sw} that is a multiple of 10 kHz, allowing synchronized sampling with a fixed frequency of 10 kHz. For instance, if the triangular waveform is set to 20 kHz, an interrupt signal is triggered every time the triangle reaches its minimum value for the second time. Similarly, with a switching frequency of 500 kHz, the interruption occurs on the fiftieth occurrence.

Additionally, a UART communication module was created in the FPGA to read temperatures sent by the Arduino UNO through UART. This was necessary because the UART port available in the MicroLabBox (MLBX) presented memory errors that prohibited its use. Consequently, a custom storage system was developed, where data of a specific size is received and stored in registers. These registers are then read by the processor, ensuring reliable communication and data handling.

On this platform, measurements of the inductor current i_L, output voltage v_o, and output current i_o are received through the ADC ports. The case temperatures T_{cA} and T_{cB}, heatsink temperature T_h, and ambient temperature T_a are obtained through the UART module in the FPGA. Based on the control algorithms, a switching signal S with a switching frequency f_{sw} and duty cycle d is then sent to the GaN Systems Motherboard.

5.2.3 Motherboard GaN Systems and IMS Evaluation Module

The High Power IMS Evaluation Platform used in the experiment is depicted in Fig. 5.5. It features a GaN Systems Motherboard to control the IMS Evaluation Module, which includes the GaN half-bridge. The motherboard is powered by a 12V supply for the internal logic signals of the gate driver and optional fan power. The PWM signal can be transmitted using either a BNC cable or through a direct connection. In this work, the signal S is sent from the MicroLabBox using a Digital Input/Output (DIO) port to the motherboard with a BNC cable. Internally, the complementary signal is generated with a fixed dead time of 100ns.

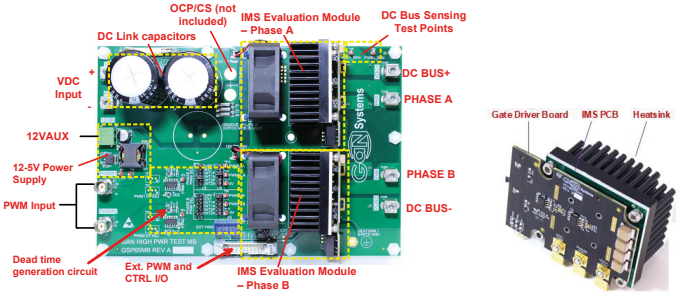

(a) Motherboard

(b) IMS Evaluation Module

Figure 5.5: High Power IMS Evaluation Platform [86].

5.2.4 DC Source Power Supply Chroma 62120D-1200

The programmable bidirectional DC power supply Chroma 62120D-1200, as shown in Fig. 5.6, provides both power source and load characteristics. The absorbed energy can feed back to the grid with a conversion efficiency of up to 93%, and the unit can operate in constant voltage, constant current, and constant power modes. It can function as a high-voltage battery capable of simulating operation at different capacities (State of Charge - SOC) or importing specific battery characteristics such as voltage-current (V-I) curves. The touch panel allows for configuration settings and monitoring of the power delivered or received. The maximum values for source/sink voltage, current, and power are 1200V, ±40A, and ±12kW, respectively.

Figure 5.6: DC Source Power Supply Chroma 62120D-1200.

5.2.5 Isolated Voltage and Current Sensing Module USM-3IV

The High-Performance Module USM-3IV is depicted in Fig. 5.7. It is fully isolated and features three channels for voltage and three channels for current sensing modules. The module has both unipolar and bipolar output IDCs, offering configurable 3V/5V unipolar output voltage, making it compatible with all types of DSP Controllers and dSPACE Controllers. The BNC output can be utilized for a direct interface with an oscilloscope as well. The current sensors are non-intrusive, allowing them to be used with bus bars. The voltage range can be selected with 10X or 100X attenuation. The frequency bandwidth of voltage and current is 100kHz and 200kHz, respectively. The range of measured current is ±100A, and the range of measured voltage is ±100V and ±1000V in 10X and 100X attenuation modes, respectively. In this work, measurements are conducted for the inductor current i_L, the output voltage v_o, and the output current i_o.

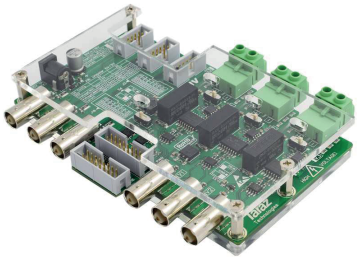

Figure 5.7: Isolated Voltage and Current Sensing Module USM-3IV.

5.2.6 IR Sensor GY-906

The IR Sensor GY-906, as shown in Fig. 5.8, is based on the MLX90614 family. It is controlled through I2C communication using the Signal Data (SDA) and Signal Clock (SCLK) pins. The voltage supply of 5V is obtained from the Arduino UNO. The sensor is calibrated in a wide temperature range from -40 to 125°C for sensor temperature T_a and from -70 to 380°C for object temperature T_o. Additionally, it undergoes high-accuracy calibration and has a measurement resolution of 0.02°C.

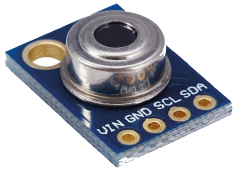

Figure 5.8: IR Sensor GY-906.

5.2.7 Arduino Uno

The Arduino UNO microcontroller is depicted in Fig. 5.9. In Fig. 5.9.a, the physical device is illustrated, and in Fig. 5.9.b, the connection diagram with the GY-906 sensors and the MicroLabBox is presented. Code A.1 demonstrates how to perform I2C communication with the GY-906 sensors and UART communication with the MicroLabBox. In Code A.2, the procedure for changing the I2C address of the GY-906 sensors is presented. The implemented code enables the retrieval of temperature readings from the sensors, followed by the transmission of these readings to the MicroLabBox. This transmission occurs synchronously, triggered by a signal sent from the MicroLabBox to request data at a user-specified frequency. In this work, the frequency is set to 10Hz to prevent reading errors and ensure accurate sampling at 1Hz.

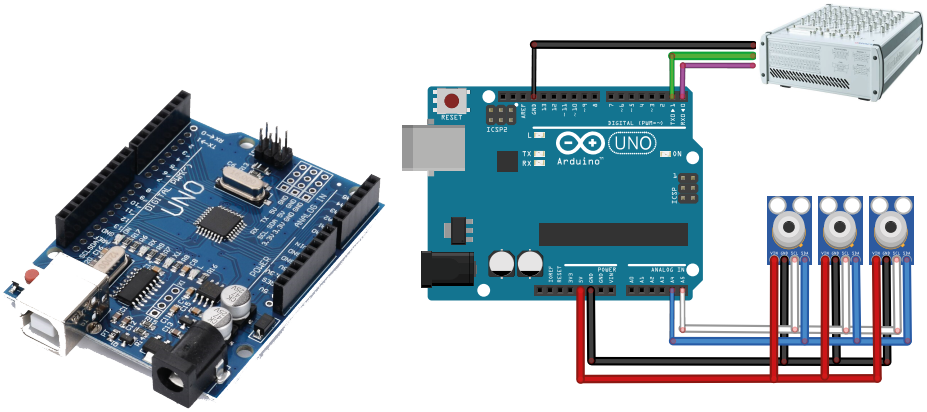

(a) Physical microcontroller (b) Connection diagram.

Figure 5.9: Arduino UNO.

5.3 Experimental Results

This section describes the most important aspects of the experimental implementation for each of the control strategies studied in the previous chapters. Experimental results are presented to verify and compare the performance of the strategies in different operating points. Four types of experiments are carried out, detailed below:

- Experiment 1: Measurements and calibration for control.
  In this experiment, currents and voltages are measured to ensure proper calibration and verify the waveforms.
- Experiment 2: Comparison current control between PI and CCS-MPC.
  In this experiment, currents and voltages are measured to compare the dynamic responses using the PI and MPC controllers.
- Experiment 3: Measurements and calibration for thermal control
  In this experiment, the case temperatures T_{cA} and T_{cB}, heatsink temperature T_h, and ambient temperature T_a are measured at different currents and switching frequencies. The data is analyzed, and a thermal model is fitted that relates temperatures to current and switching frequency dynamically and in steady state.
- Experiment 4: Comparison thermal control between PI and CCS-MPC
  In this experiment, the temperature response is compared between scenarios without using the ATC and when the ATC is employed, considering two types of control. First, temperature control is performed using the conventional PI controller, and then it is compared with the proposed CCS-SMPC based controller.

5.3.1 Experiment 1: Measurements and calibration for control

In this experiment, the parameters shown in Tab. 5.2 are used.

Table 5.2: Main parameters of current control experiments.

Symbol	Parameter	Value
V_{dc}	DC link voltage	$20V$
R_o	Load resistance	10Ω
L	Converter Inductance	$510\mu H$
C	Converter Capacitance	$4700\mu F$
$f_{s,i}$	Sampling frequency for current	10kHz
f_{sw}	Switching frequency	10kHz

Voltages and currents will be measured to verify the correct implementation of synchronized sampling and calibration. For this purpose, a low DC-Link voltage is employed. Additionally, the LC filter components are intentionally oversized for safety, as unconventional research tests will be conducted. The choice of high capacitance also emulates, to some extent, the slow dynamics of battery charging compared to current dynamics. The inductor used is a WE-TORPFC Toroidal PFC Choke, designed to operate at high frequencies while maintaining an inductance close to 510μH with a rated current of 9.8A. The parasitic resistance of the inductor, r_L, measured with a voltmeter, is close to $140\text{m}\Omega$.

Fig. 5.10 illustrates the correct synchronized sampling of the inductor current, represented by the triangular waveform (green signal) and its average value (blue signal). Fig. 5.10.a shows the simulation, while Fig. 5.10.b presents the experimental results. With a duty cycle of $d = 0.5$, a current close to 1A and an output voltage close to 10V are achieved.

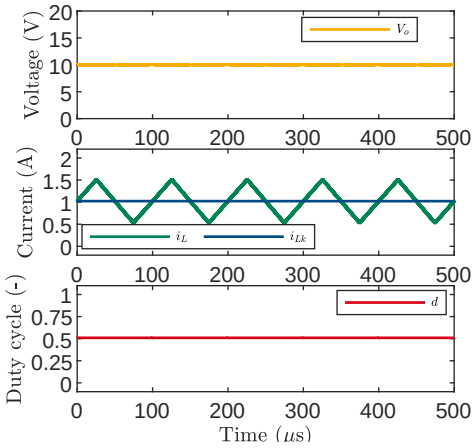

(a) Simulation Waveform.

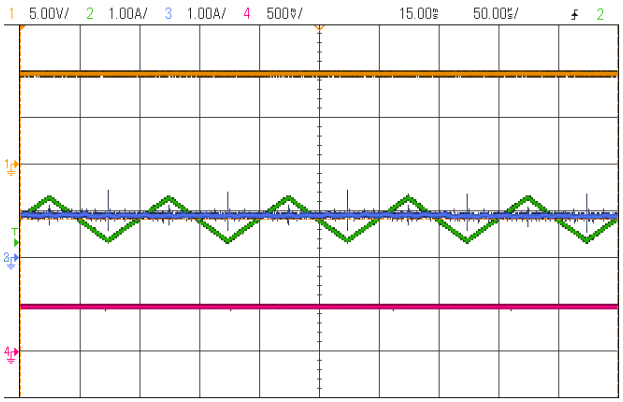

(b) Experiment Waveform in Oscilloscope.

Figure 5.10: Synchronized sampling.

Fig. 5.11 depicts the correct synchronized sampling of the inductor current in response to a step change in duty cycle from 0 to 0.1. Fig. 5.11.a shows the comparison between simulation and experiment, while Fig. 5.11.b presents the waveform experimental results captured with Oscilloscope. With a duty cycle step of $d = 0.1$, an overshoot of current close to 5A is achieved.

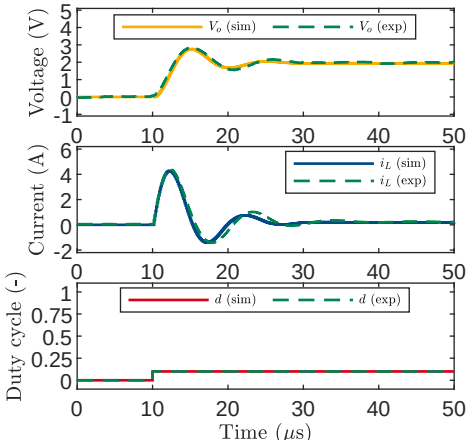

(a) Comparison of Simulation and Experiment.

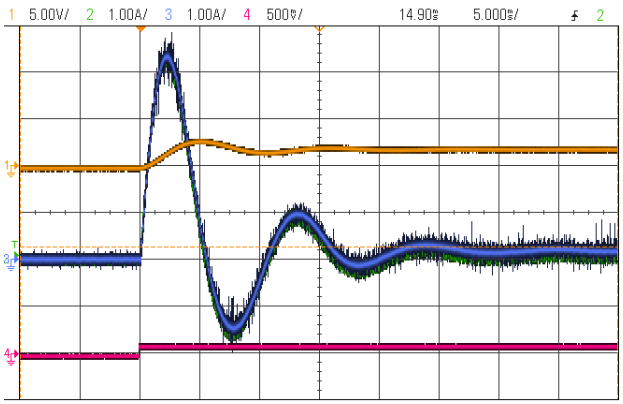

(b) Experiment Waveform in Oscilloscope.

Figure 5.11: Step response with duty cycle 10%.

Furthermore, in Fig. 5.11, it is possible to see that the converter is capable of operating with bidirectional power, as the current can be negative. Then, in Fig. 5.12, the waveforms of the drain-source voltage $V_{DS,B}$ of Q_B, the DC source current i_{dc} (almost equal to $i_{DS,A}$), the measured inductor current i_{Lk}, and the measured output voltage v_{ok} are shown both in simulation and experimentally. This verifies that when GaN devices operate in dead time, approximately 100ns in this case, they block a voltage close to 5V, similar to diodes. Additionally, it is observed that the signals exhibit ringing due to parasitic inductances and take times close to nanoseconds to turn on and off.

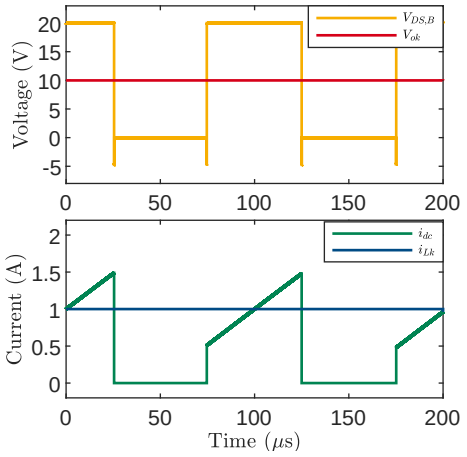

(a) Simulation waveforms

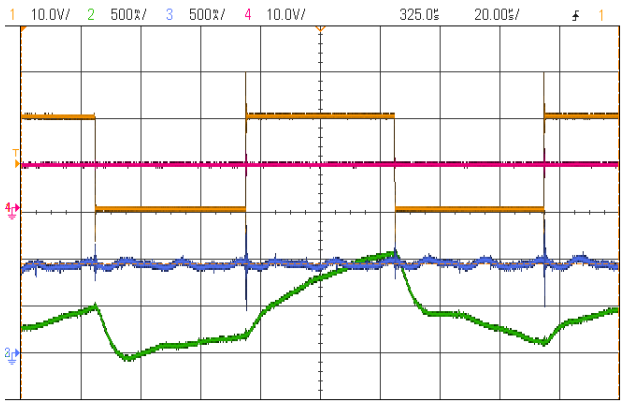

(b) Experimental waveforms

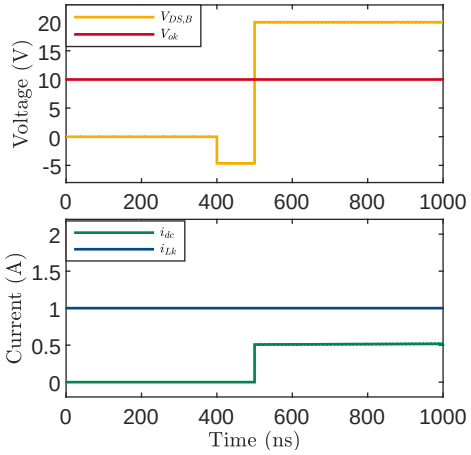

(c) Simulation waveforms with zoom

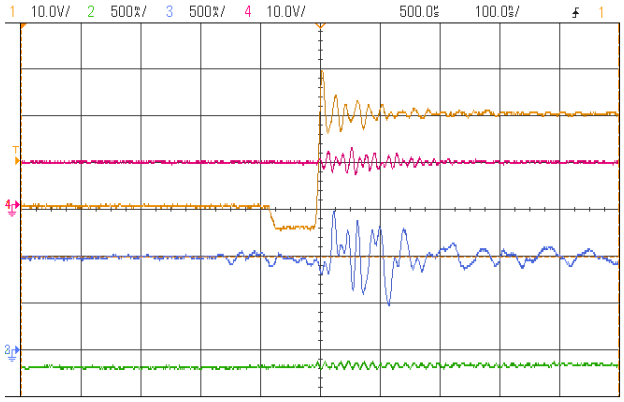

(d) Esperimental waveforms with zoom

Figure 5.12: Waveforms of $V_{DS,B}$, i_{DC}, i_{Lk} and v_o with dead-time.

5.3.2 Experiment 2: Comparison current control between PI and MPC

In this experiment, the parameters shown in Tab. 5.2 are used and the PI controller gains for current control are $K_{pi} = 0.85496$ and $K_{ii} = 0.82279$ with feedforward structure, see Fig. 3.12. Fig. 5.13 depicts the dynamic response of the current and voltage to a reference step from 0 to 1A using the conventional PI controller with feedforward.

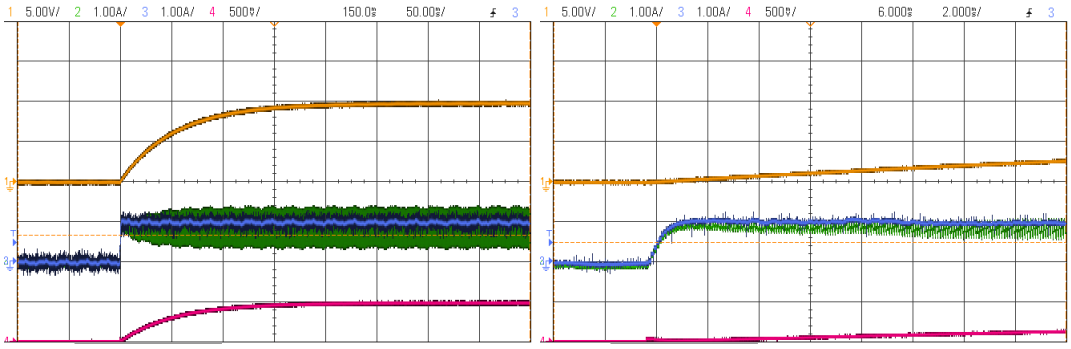

(a) Voltage's dynamic (b) Current's dynamic

Figure 5.13: Step response of PI with $I_{ref} = 1$A.

Fig. 5.14 depicts the dynamic response of the current and voltage to a reference step from 0 to 1A using the proposed MPC controller.

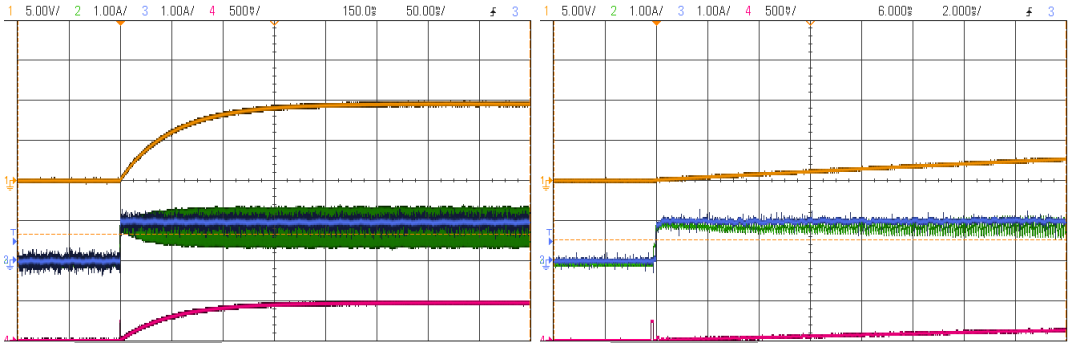

(a) Voltage's dynamic (b) Current's dynamic

Figure 5.14: Step response of MPC with $I_{ref} = 1$A.

In broad terms, there isn't much difference between the dynamic responses. However, it is noticeable that the current reaches the reference faster when using the MPC controller. The comparison of responses using the PI and MPC controllers is shown in Fig. 5.15, where it is observed that with MPC, the reference is reached faster than with the PI.

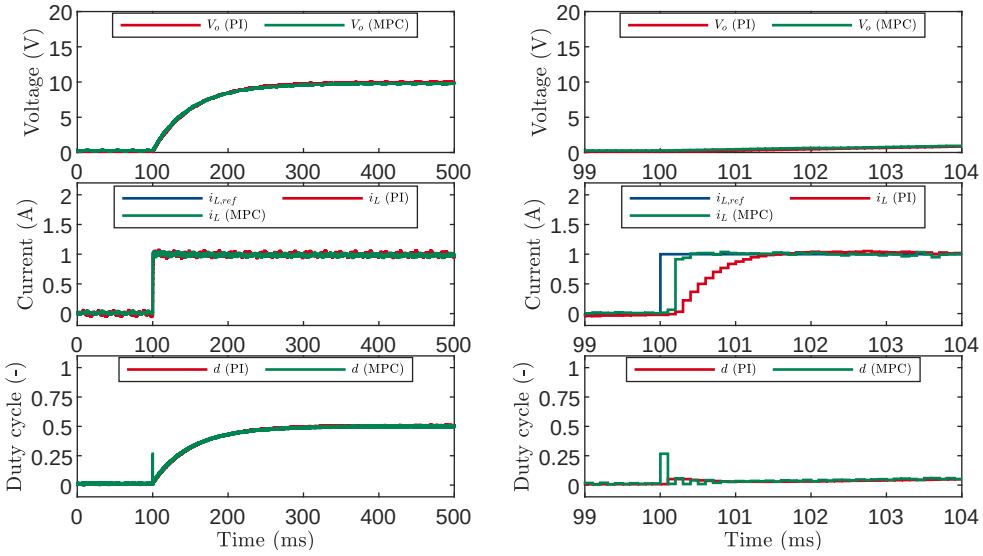

(a) Voltage's dynamic

(b) Current's dynamic

Figure 5.15: Comparison current control between PI and MPC with $I_{ref} = 1$A.

5.3.3 Experiment 3: Measurements and calibration for thermal control

In this experiment, the parameters shown in Tab. 5.3 are used. In the subsequent experiments, a higher DC-Link voltage is employed to achieve increased currents, and the load resistance is reduced to prevent excessive heating during prolonged tests. Furthermore, the switching frequency is varied across a wide range to allow for a more comprehensive modeling of the thermal behavior with a good margin.

Table 5.3: Main parameters of thermal control experiments.

Symbol	Parameter	Value
V_{dc}	DC link voltage	100 V
R_o	Load resistance	5 Ω
L	Converter Inductance	510 μH
C	Converter Capacitance	4700 μF
$f_{s,i}$	Sampling frequency for current	10 kHz
$f_{s,t}$	Sampling frequency for temperature	1 Hz
$f_{sw,min}$	Minimum switching frequency	10 kHZ
$f_{sw,max}$	Maximum switching frequency	500 kHZ

5.3.3.1 Measurements and calibration

First, it is verified in Fig. 5.16 that it is possible to change the switching frequency from 10kHz to 50kHz while maintaining the synchronized sampling of the current at 10kHz. Fig. 5.16.a shows the expected response in simulation, and Fig. 5.16.b displays the response obtained in the experiment.

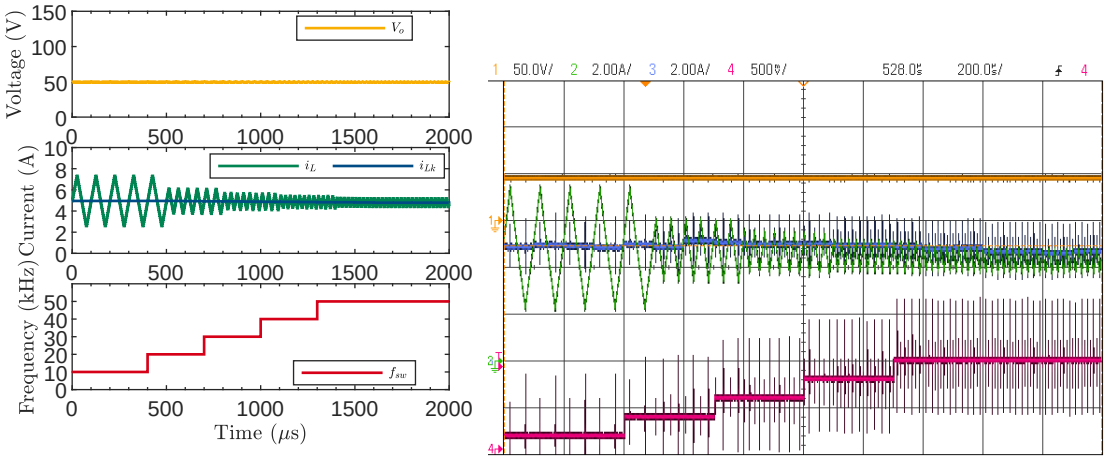

(a) Simulation (b) Experiment

Figure 5.16: Switching frequency step responses

In Fig. 5.16.b, the reduction in current ripple as the switching frequency is increased from 10 to 50kHz is clearly demonstrated. Additionally, it is evident that with an increase in switching frequency, the switching noise gets filtered into analog signals that do not undergo switching, such as the signal originating from the Digital-to-Analog Converter (DAC) of the MLBX. This constant signal exhibits peaks corresponding to the instances when the semiconductor switches.

Additionally, in Fig. 5.17.a, not only does it highlight the thermal response to changes in current reference from 1 to 8A and alterations in switching frequencies of 10, 400, and 500kHz, but it also reveals that the duty cycle increases when the frequency is changed from 10 to 500kHz. This observation verifies that the actual duty cycle is dependent on both the frequency and the dead time. Notably, variations in ambient temperature significantly influence the case and heatsink temperatures, with a marked shift observable at minute 450 in Fig. 5.17.a and minute 470 in Fig. 5.17.b. A steady state is achieved after 50 minutes, with the peak temperature reaching 87°C at 8A and 500kHz. Discontinuities in the measurements at approximately 200 and 460 minutes are attributed to a temporary loss of communication between the Arduino UNO and the MLBX. Following a restart of the Arduino, data collection resumed without further incidents.

In the experiments depicted in Fig. 5.17.b, the current was adjusted in increments of 2A, ranging from 2 to 8A, at switching frequencies of 350 and 450kHz. This setup not only further elucidates the impact of varying electrical stresses and operational conditions on thermal dynamics but also underscores the critical relationship between duty cycle adjustments, switching frequencies, and their combined effects on thermal behavior.

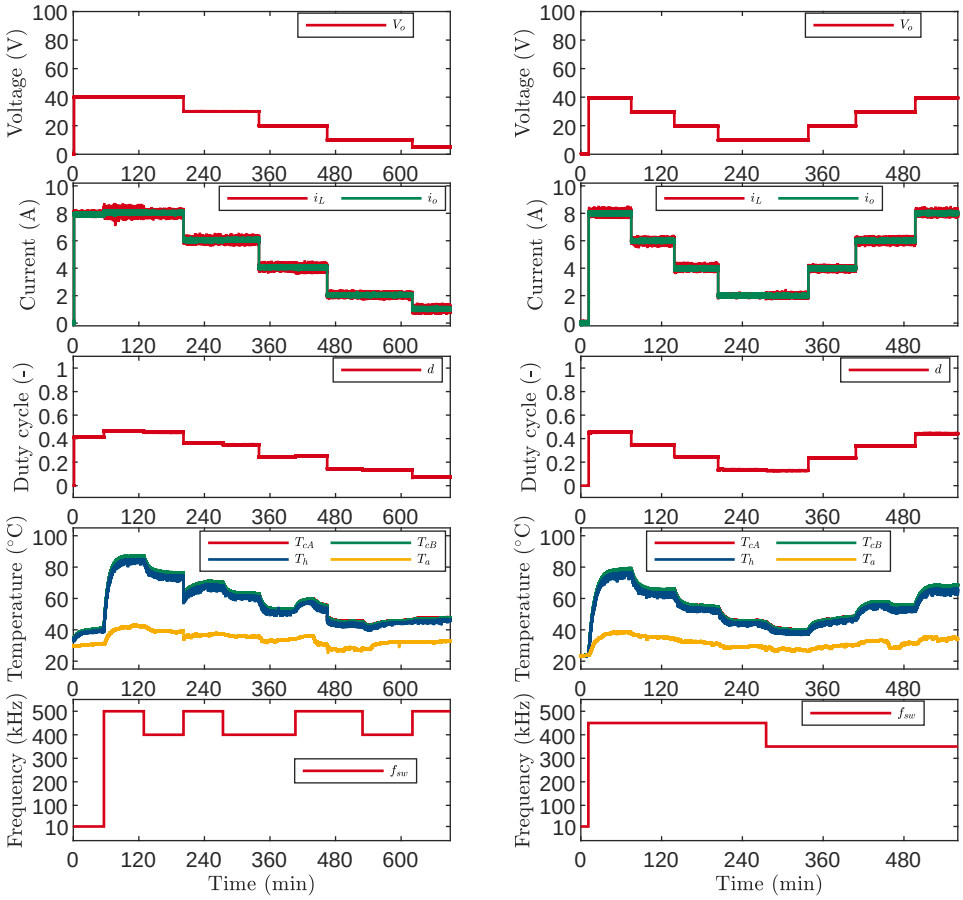

(a) $I \in \{1, 2, 4, 6, 8\}$A and $f_{sw} \in \{10, 400, 500\}$kHz (b) $I \in \{2, 4, 6, 8\}$A and $f_{sw} \in \{350, 450\}$kHz

Figure 5.17: Variation of T_j respect to current I with fixed switching frequency $f_{sw} \in \{10, 350, 400, 450, 500\}$kHz.

In Fig. 5.18.a, the current is varied in increments of 2A from 2 to 8A at frequencies of 200 and 300 kHz, and in Fig. 5.18.b, the current is varied in increments of 2A from 2 to 8A at frequencies of 10 and 100 kHz. It is observed that the case temperature T_{cB} of device Q_B is consistently higher than the case temperature T_{cA} of device Q_A and the heatsink temperature T_h. This observation supports the hypothesis that the thermal system can be effectively modeled using a Cauer model, as formulated in Eq. (2.75).

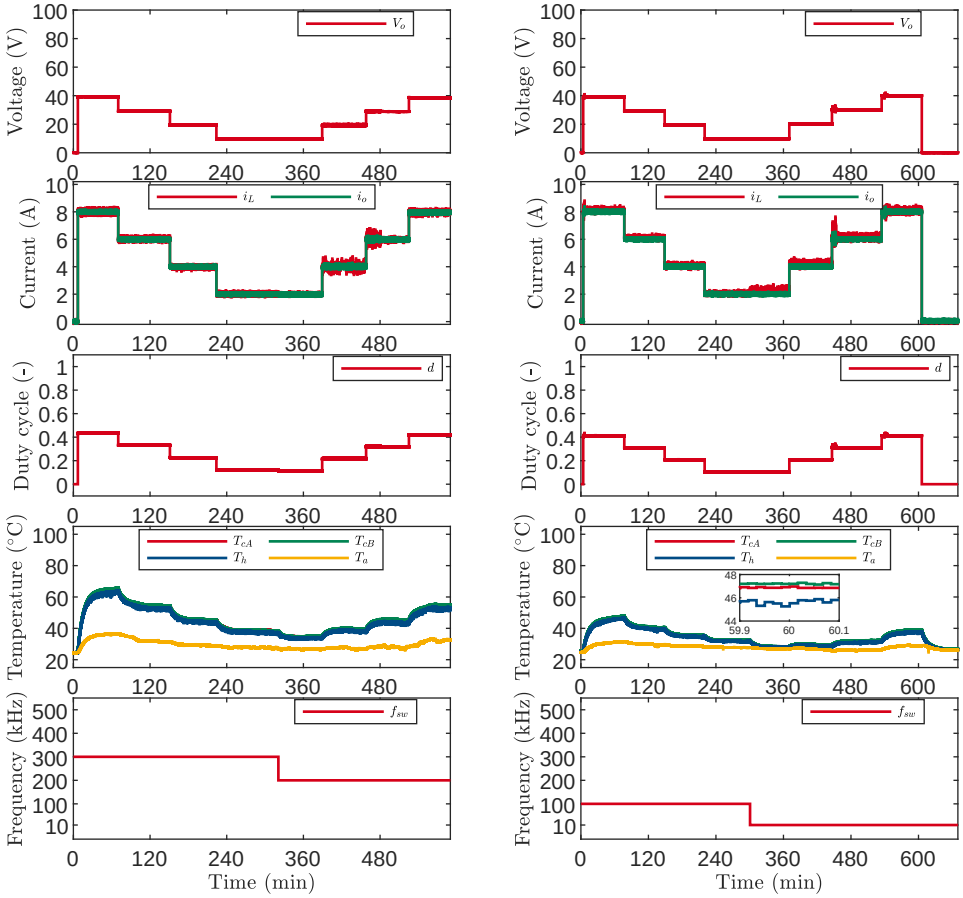

(a) $I \in \{2, 4, 6, 8\}$A and $f_{sw} \in \{200, 300\}$kHz.

(b) $I \in \{2, 4, 6, 8\}$A and $f_{sw} \in \{10, 100\}$kHz.

Figure 5.18: Variation of T_j respect to current I with fixed switching frequency $f_{sw} \in \{10, 100, 200, 300\}$kHz.

5.3.3.2 Summary results and estimation of thermal model

The summary results obtained at steady state from the experiments depicted in Fig. 5.17 and Fig. 5.18 are next analyzed.

In Chapter 2, Eq. (2.79) was derived to estimate the relationship between thermal resistances R_{jh} and R_h with temperatures T_{cA}, T_{cB}, T_h, and T_a in steady state. According to the datasheet [25, 86], the junction-to-heatsink resistance is $R_{jh} = 1.4°$ C/W. Therefore, if the relationship is 2.4, the heatsink resistance would be $R_h = 3.36°$ C/W. However, experimental data shows that this relationship is not constant. Consequently, the relationship between temperature and power loss, as established in Eq. (2.78), will be used. Power loss exhibits a quadratic variation with current and a linear dependence on frequency, as detailed in Eq. (2.81). The difference between case and ambient temperatures is directly proportional to power losses. This relationship is evident in Fig. 5.19, where power losses exhibit a quadratic dependence on current and a linear correlation with switching frequency. Therefore, the observed trends in temperature differences align with the established relationship for power losses. Nevertheless, it is crucial to acknowledge that these data possess a restricted valid range for positive currents other than 0. As depicted in Fig. 5.17(a), the ambient temperature near the heatsink rises in the presence of power losses. Additionally, Fig. 5.18(b) illustrates that when the current is 0, it descends to the actual outside ambient temperature, attaining thermal equilibrium.

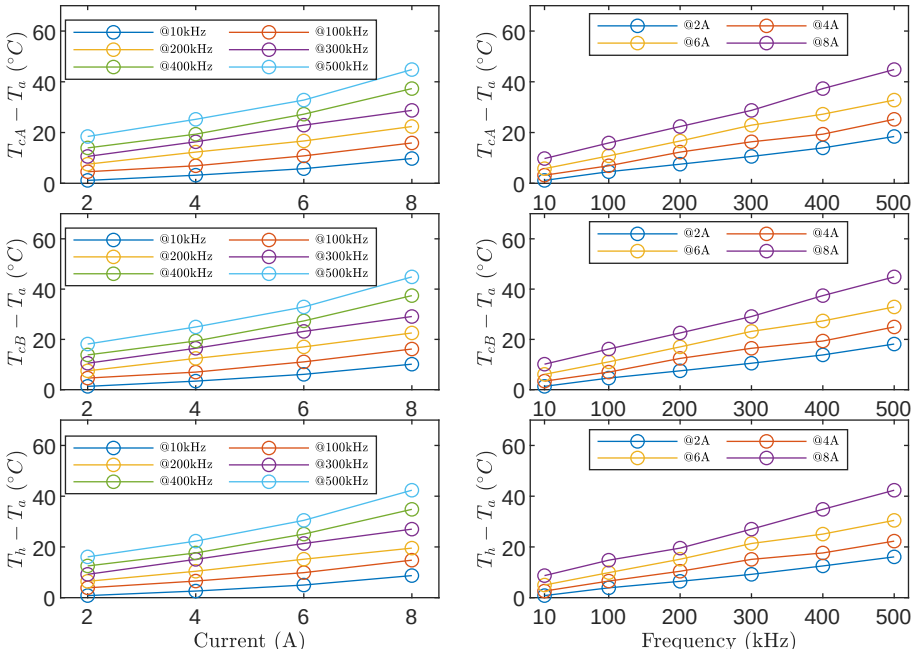

Figure 5.19: Variation of temperature respect to inductor current and switching frequency.

Then, an estimation of junction temperature is proposed with the aproximation that the measurement of case temperature is enough and has a ΔT that varies with the structure based on estimated power losses structure in Eq. (2.81). Then case and heatsink temperatures can be

estimated such that:

$$T_{cA} = T_a + \Delta T_A \qquad T_{cB} = T_a + \Delta T_B \qquad T_h = T_a + \Delta T_H \tag{5.1}$$

Where ΔT_A, ΔT_B, and ΔT_H are calculated using Eq. (5.2), Eq. (5.3), and Eq. (5.4) respectively.

$$\Delta T_A(I, f_{sw}) = a_1 I^2 + a_2 I + a_3 + a_4 I^2 f_{sw} + a_5 I f_{sw} + a_6 f_{sw} \tag{5.2}$$
$$\Delta T_B(I, f_{sw}) = b_1 I^2 + b_2 I + b_3 + b_4 I^2 f_{sw} + b_5 I f_{sw} + b_6 f_{sw} \tag{5.3}$$
$$\Delta T_H(I, f_{sw}) = h_1 I^2 + h_2 I + h_3 + h_4 I^2 f_{sw} + h_5 I f_{sw} + h_6 f_{sw} \tag{5.4}$$

To determine the parameters, the least squares method is employed. To facilitate this, the data should be organized in the following structure:

$$y(k) = \omega(k) + \sum_{i=1}^{n} \varphi_i(k)\theta_i \tag{5.5}$$

The parameters are then estimated using the least squares approach, and they must be represented in matrix form as follows:

$$Y = \Phi\theta \qquad Y = \begin{bmatrix} y(1) \\ \vdots \\ y(N) \end{bmatrix} \qquad \Phi = \begin{bmatrix} \varphi_1(1) & \dots & \varphi_n(1) \\ \vdots & \ddots & \vdots \\ \varphi_1(N) & \dots & \varphi_n(N) \end{bmatrix} \qquad \theta = \begin{bmatrix} \theta_1 \\ \vdots \\ \theta_n \end{bmatrix} \tag{5.6}$$

The parameters are calculated as:

$$\hat{\theta} = (\Phi^T \Phi)^{-1} \Phi^T Y \tag{5.7}$$

Where the matrices with the measured data are:

$$Y_A = \begin{bmatrix} T_{cA}(1) - T_a(1) \\ \vdots \\ T_{cA}(N) - T_a(N) \end{bmatrix} \quad Y_B = \begin{bmatrix} T_{cB}(1) - T_a(1) \\ \vdots \\ T_{cB}(N) - T_a(N) \end{bmatrix} \quad Y_H = \begin{bmatrix} T_h(1) - T_a(1) \\ \vdots \\ T_h(N) - T_a(N) \end{bmatrix} \quad \theta_A = \begin{bmatrix} a_1 \\ a_2 \\ a_3 \\ a_4 \\ a_5 \\ a_6 \end{bmatrix}$$

$$\theta_B = \begin{bmatrix} b_1 \\ b_2 \\ b_3 \\ b_4 \\ b_5 \\ b_6 \end{bmatrix} \quad \theta_H = \begin{bmatrix} h_1 \\ h_2 \\ h_3 \\ h_4 \\ h_5 \\ h_6 \end{bmatrix} \quad \Phi = \begin{bmatrix} I(1)^2 & I(1) & 1 & I(1)^2 f_{sw}(1) & I(1) f_{sw}(1) & f_{sw}(1) \\ \vdots & \vdots & \vdots & \vdots & \vdots & \vdots \\ I(N)^2 & I(N) & 1 & I(N)^2 f_{sw}(N) & I(N) f_{sw}(N) & f_{sw}(N) \end{bmatrix} \tag{5.8}$$

The parameters θ_A, θ_B and θ_H for T_{cA}, T_{cB} and T_h respectively are:

$$\theta_A = \begin{bmatrix} 0.0921573470380253 \\ 0.365510293517559 \\ -0.298662845406852 \\ 0.000252080839325791 \\ 0.0035605811991104 \\ 0.0259710433110181 \end{bmatrix} \quad \theta_B = \begin{bmatrix} 0.0886382185249346 \\ 0.434488478864409 \\ -0.254902190776875 \\ 0.000253150779639721 \\ 0.00361090536434228 \\ 0.0250251058862059 \end{bmatrix} \quad \theta_H = \begin{bmatrix} 0.0624357530016511 \\ 0.507596653245514 \\ -0.779380648645656 \\ 0.000351406189532499 \\ 0.00267442334635648 \\ 0.0236165753554527 \end{bmatrix} \tag{5.9}$$

Then, temperature time constants τ_A, τ_B and τ_H are obtained with measurement procedure from Eq. (2.85). The procedure is repeated multiple times with measurements to confirm the accurate estimation of the time constant. As the ambient temperature varied during the tests due to external factors such as air conditioning or the temperature of the day on which the test was conducted, the data in which the ambient temperature remained more constant is considered more reliable.

Finally, the time constants for the three temperatures were calculated, yielding values very close to each other, approximately 592 seconds. This consistency makes sense, considering that if the temperature remains at 5 times the time constant, around 50 minutes, most tests align with this time interval. Then:

$$\tau_A = \tau_B = \tau_H \approx 592s \tag{5.10}$$

And the aproximated first order dynamical systems for each temperature are:

$$\tau_A \frac{d}{dt} T_{cA} = -T_{cA} + T_a + \Delta T_A(I, f_{sw}) \tag{5.11a}$$

$$\tau_B \frac{d}{dt} T_{cB} = -T_{cB} + T_a + \Delta T_B(I, f_{sw}) \tag{5.11b}$$

$$\tau_H \frac{d}{dt} T_h = -T_h + T_a + \Delta T_H(I, f_{sw}) \tag{5.11c}$$

This first order systems can be written as:

$$\tau \frac{d}{dt} T = -T + T_a + K_{t1} + K_{t2} f_{sw} \tag{5.12}$$

Where,

$$K_{t1} = \theta_1 I^2 + \theta_2 I + \theta_3 \qquad K_{t2} = \theta_4 I^2 + \theta_5 I + \theta_6 \tag{5.13}$$

And the discrete-time model with sampling time $T_{s,t}$ is obtained with the same structure as in Eq. (2.86).

$$T(k+2) = b_1 T(k+1) + b_2 f_{sw}(k) + b_3 \tag{5.14}$$

Where

$$b_1 = \exp\left(-\frac{T_{s,t}}{\tau}\right) \qquad b_2 = K_{t2}(1-b_1) \qquad b_3 = (T_a + K_{t1})(1-b_1) \tag{5.15}$$

The linearized system can be obtained with an equilibrium point for T_Q with $I_Q \geq 0$ and $f_{sw,Q}$ such that

$$T_Q = T_{a,Q} + \theta_1 I_Q^2 + \theta_2 I_Q + \theta_3 + \left(\theta_4 I_Q^2 + \theta_5 I_Q + \theta_6\right) f_{sw,Q} \tag{5.16}$$

Finally,

$$\tau \frac{d}{dt} T = (T - T_Q) + K_2(f_{sw} - f_{sw,Q})) \tag{5.17}$$

$$K_2 = \theta_4 I_Q^3 + \theta_5 I_Q^2 + \theta_6 I_Q \tag{5.18}$$

Then the linear plant is

$$G_t(s) = \frac{K_2}{\tau s + 1} \tag{5.19}$$

Similarly to the discussion in Chapter 2, the parameters of the thermal model fluctuate with the current and ambient temperature, leading to the variations in the constants $b_2(I)$ and $b_3(I, T_a)$.

5.3.3.3 Comparison of Experimental Data with Adjusted Model

To verify that the adjusted model adequately captures the dynamic and steady-state behavior of the real system, a comparison is made between the data used for fitting with least squares and the dynamics observed in experimental data from a test conducted with the adjusted dynamic model. This is done to validate the performance and accuracy of the model.

In Fig. 5.20, the steady-state experimental data are depicted alongside the corresponding calculated data derived from the fitted model, utilizing the currents and frequencies obtained from the experiments. The calculated data align closely with the experimental data in most cases. However, noticeable discrepancies, such as at the frequencies of 350 kHz and 450 kHz, are present. It's important to note that these discrepancies may arise due to the data being averages of measurements in steady state, which are employed to mitigate variations caused by white noise.

Additionally, Fig. 5.21 illustrates the dynamic comparison between the experimental data and the simulation results obtained through the dynamically adjusted model. It is noteworthy that the fitted model consistently aligns with the majority of the dataset, thereby substantiating the assertion that the proposed model is deemed suitable for the objectives outlined in this study.

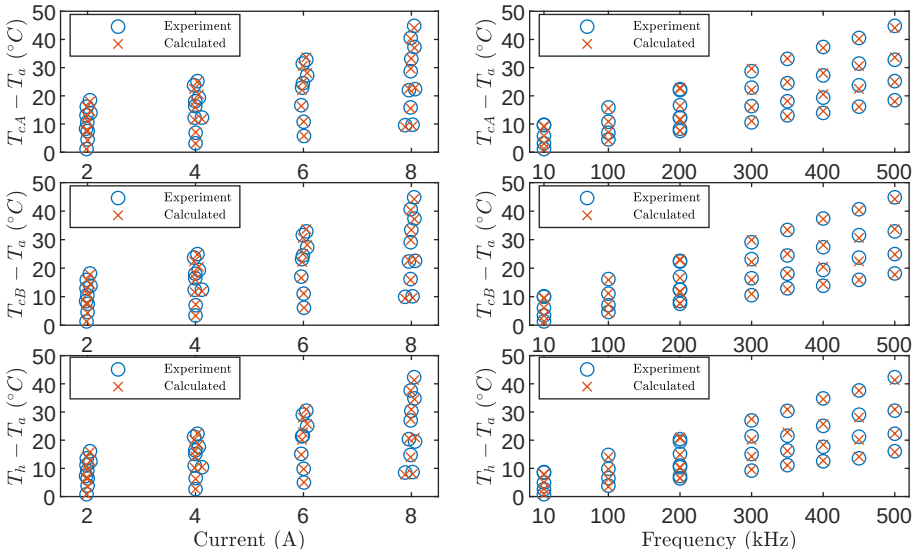

Figure 5.20: Comparison of experimental data with adjusted model.

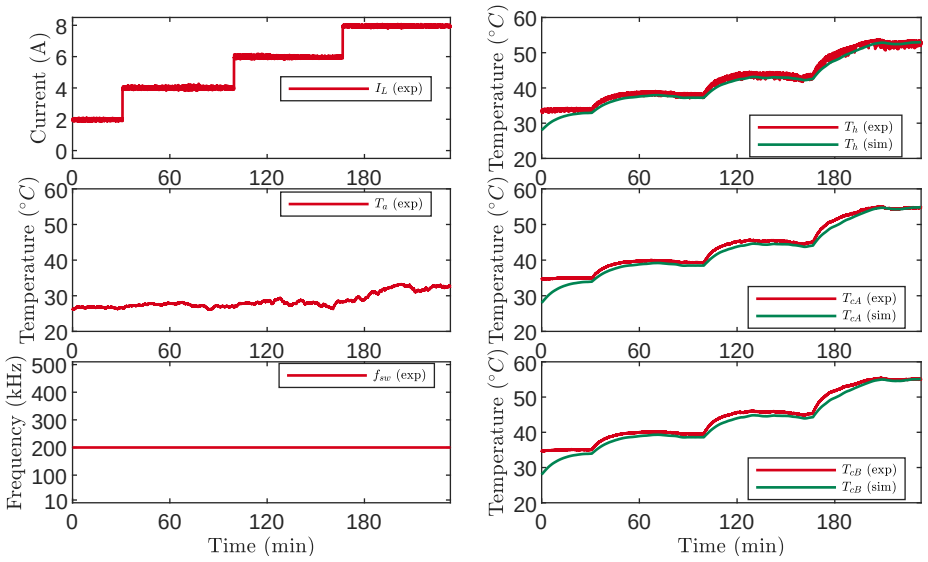

Figure 5.21: Dynamic comparison of experimental data with adjusted model.

5.3.3.4 Discussion about effiency

Throughout the experiments, meticulous recording of the power delivered by the DC Chroma source was undertaken. This dataset enables a comprehensive analysis of total power losses and the efficiency of the converter across various currents and switching frequencies. In Fig. 5.22, the efficiency and total loss powers are graphically depicted in relation to the output power, current, and switching frequency, respectively. Notably, it is observed that at low output power and high switching frequency, the efficiency is notably low. However, with increasing output power, the efficiency tends to converge to a value close to 98%. Moreover, the manual of the GaN Systems evaluation module [86] documents an output power sweep up to 2400W at a switching frequency of 80kHz, demonstrating an efficiency of 98.7%. Additionally, the efficiency appears to stabilize and become nearly constant after reaching 1000W. The efficiency curve from the manual is illustrated in Fig. 5.23.

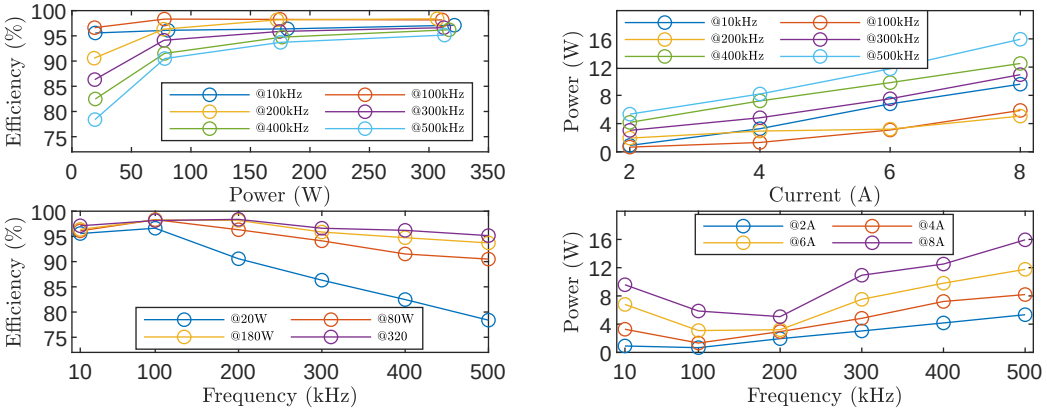

(a) Efficiency (b) Total power loss

Figure 5.22: Variation efficiency and total power loss respect to output power or current and frequency.

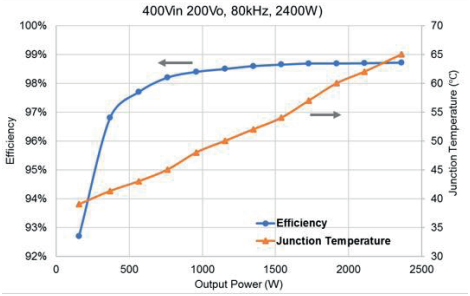

Figure 5.23: Efficiency curve from GaN Systems module manual [86].

Furthermore, it is noteworthy that the total power loss has a minimum at a switching frequency close to 200kHz. This phenomenon can be elucidated by considering that the total losses can be approximated as the sum of the losses in the GaN devices and the losses in the inductor, expressed as:

$$P_{Loss,Total} = P_{in} - P_{out} \approx P_{Loss,A} + P_{Loss,B} + P_{r_L} \tag{5.20}$$

The power loss in the inductor P_{r_L} was analyzed in Chapter 2, as denoted by Eq. (2.63), which indicates a dependence on parasitic resistance, current ripple, and its average value. Given that the current ripple decreases with frequency, it is reasonable to observe a reduction in losses with increasing frequency. However, in Fig. 5.24, the measurement of inductance and parasitic resistance using the Keysight E5061B network analyzer reveals a significant decrease in parasitic resistance as the frequency increases. This decrease becomes pronounced, reaching almost constant values and approaching zero at 200kHz. Hence, a minimum of losses is attained at high switching frequencies. Beyond this point, the losses escalate due to the linear nature of losses in GaN devices at the switching frequency.

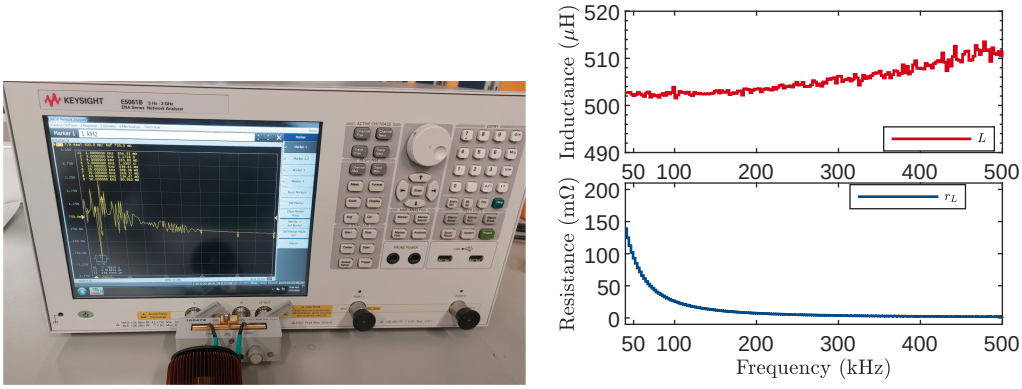

(a) Network Analyzer measuring r_L with frequencies from 5Hz to 50kHz

(b) Measurements from Network Analyzer with frequencies from 40 to 500kHz

Figure 5.24: Variation of inductance L and series resistance r_L of inductor respect to frequency.

5.3.4 Experiment 4: Comparison thermal control between PI and MPC

In this experiment, the parameters listed in Tab. 5.3 are utilized. However, the load resistance is varied, following the values presented in Tab. 5.1. This allows the implementation of a voltage control with a PI controller to emulate the operation of constant voltage and power variation, which manifests as current variation. The voltage PI controller is tuned with gains $K_{pv} = 0.79307$ and $K_{iv} = 0.78985$. This adjustment is made to ensure that in closed-loop operation, the system achieves a bandwidth of 30Hz with a 10% overshoot. According to the transfer function obtained in Eq. (5.19) with equilibrium point $Q = \{I_Q = 4\text{A}, f_{sw,Q} = 200\text{kHz}, T_{a,Q} = 25°\text{C}, T_{cB,Q} = 36.6°\text{C}\}$, a thermal PI controller is tuned with gains $K_{pt} = 4440.2$ and $K_{it} = 4378.017$. This adjustment is made to ensure that in closed-loop operation, the system achieves a bandwidth of 0.05Hz with a 3% overshoot. Furthermore, the system is configured to operate with multiples of 10kHz, and

this aspect is duly taken into account in the anti-windup scheme. Fig. 5.25 depicts the closed-loop response of the temperature control with the PI controller, wherein the temperature reference is varied from 40 to 50°C while adjusting the current in the range of 4 to 8A. Fig. 5.25.a illustrates the response under current control, while Fig. 5.25.b illustrates the response under voltage control.

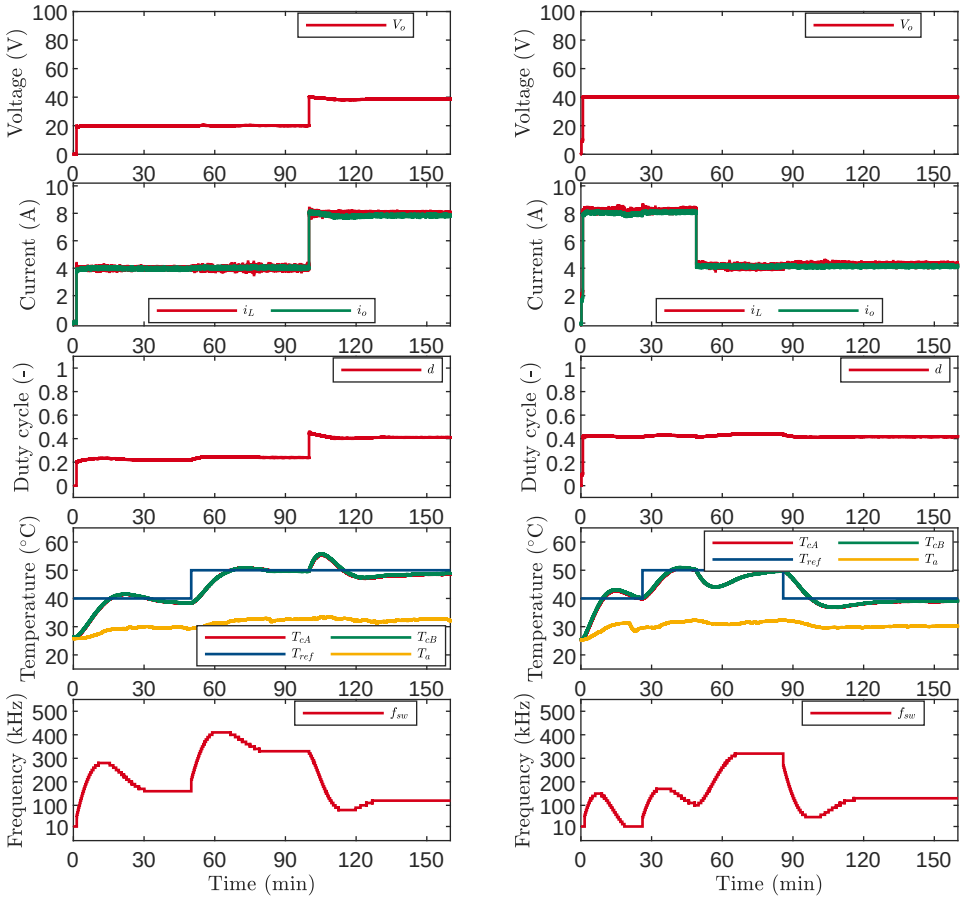

(a) Current control

(b) Voltage control

Figure 5.25: Thermal PI controller response with Current and Voltage control.

This verifies that temperature control can be effectively achieved, irrespective of the control type—whether it be current or voltage. Notably, the analysis does not delve into the impact of load changes on voltage control, as this aspect is extensively explored in the literature, with potential enhancements possible through controllers like the MPC proposed in this study. For the specific focus of this work, the rapid occurrence of this effect is deemed irrelevant to temperature dynamics. This is supported by the observation that, with a sampling time of 1s, no discernible increase or drop in voltage is observed when the load undergoes changes.

In Fig. 5.26.a, it is evident that without the ATC scheme, the temperature exhibits a wide range of variation when power or current changes at a fixed switching frequency. In this case, 200kHz is chosen due to having the lowest total losses, i.e., maximum efficiency. Conversely, Fig. 5.26.b demonstrates that implementing the ATC scheme effectively controls the temperature, maintaining it relatively constant at 40°C. However, it is notable that when there are load changes, the temperature experiences a disturbance that takes approximately 15 minutes to correct.

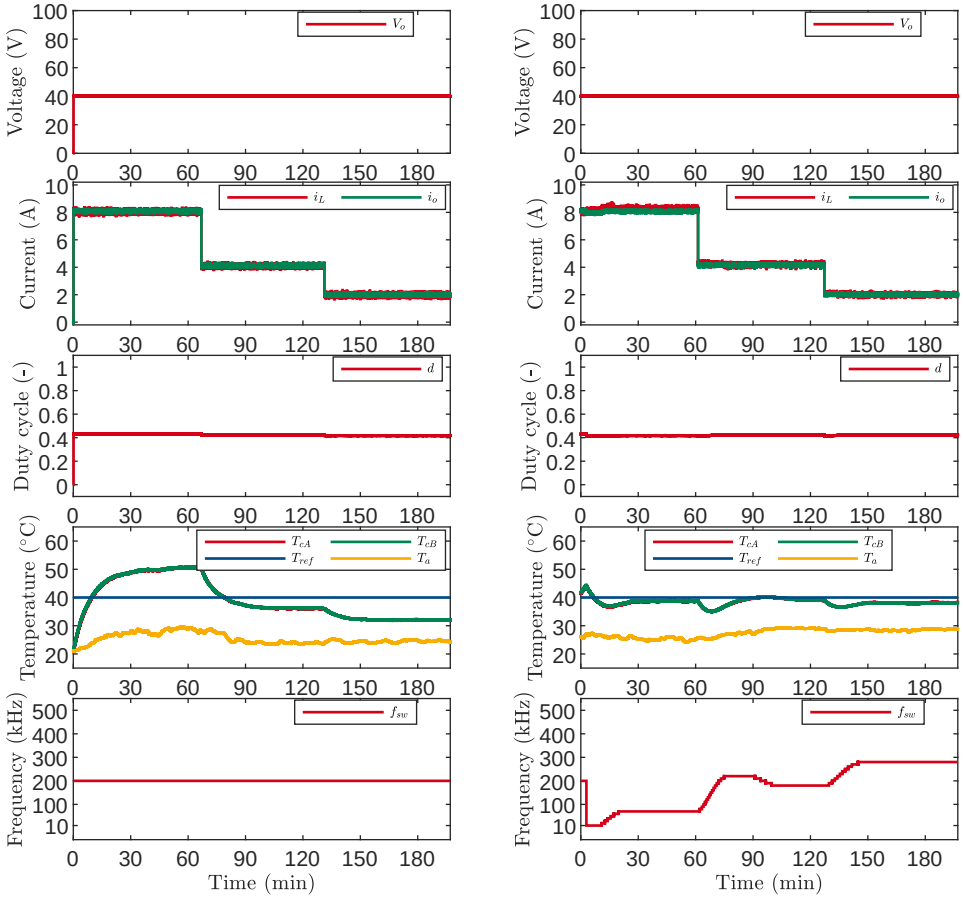

(a) Without ATC

(b) With ATC using PI

Figure 5.26: Influence of P_{out} variation in junction temperature.

The design of the PI controller is not thoroughly optimized for maximal performance but rather serves to demonstrate its primary functionality. Other potential designs could incorporate feedforward control or more aggressive actuation, which might generate faster responses but could potentially lead to overshooting.

Fig. 5.27 illustrates the operation of the ATC scheme with the MPC controller considering implementation delay with the addition of 1 step of prediction with the previous control input. In Fig. 5.27.a, it is evident that without proper adjustment of the controller, a response similar to hysteresis-type controllers can be obtained. In Fig. 5.27.b, the MPC controller can be tuned to relax the requirement for perfect reference tracking, allowing for a margin of error to maintain a quasi-constant switching frequency. In this study, a permissible error of 1.5°C relative to the reference temperature was allowed. Within this range, the model's optimal switching frequency is implemented to maintain the temperature as closely aligned with the reference as possible.

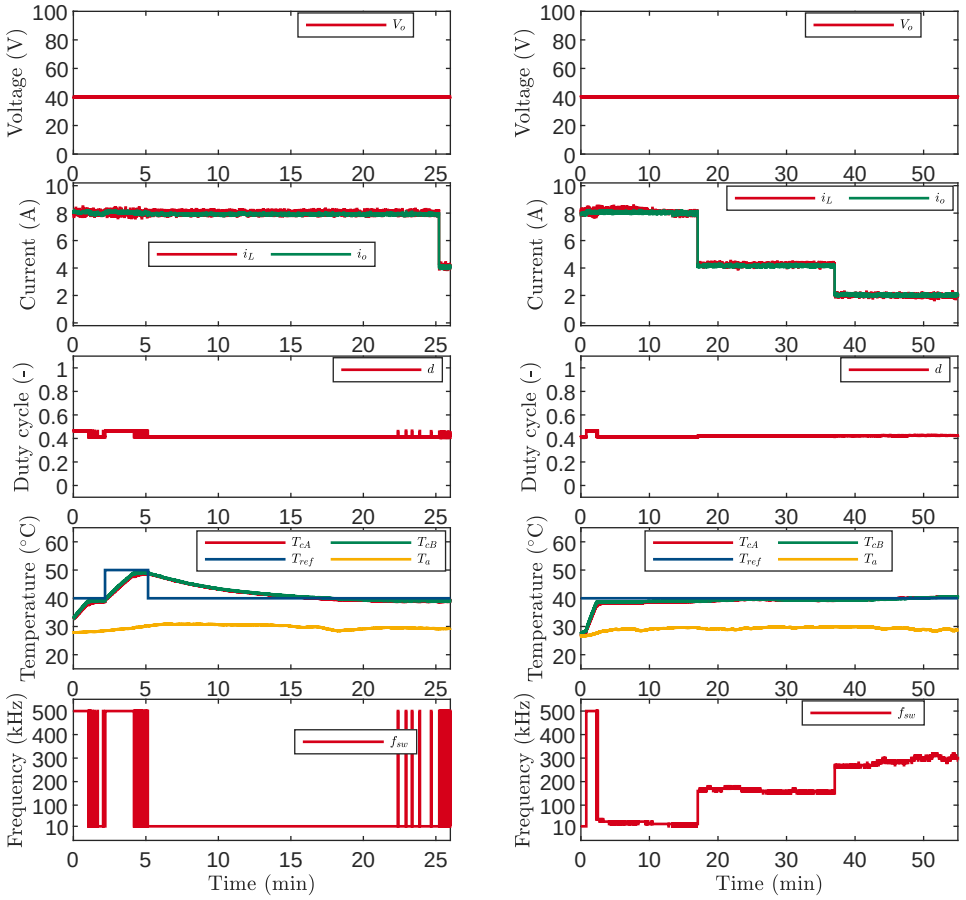

(a) Behavior of MPC as hysteresis.

(b) Behavior of MPC with relaxed requirement.

Figure 5.27: Influence of P_{out} variation in junction temperature with ATC using MPC.

In contrast to the response with the PI controller, when employing the MPC controller, the temperature scarcely varies during load changes. This validates the hypothesis of this work. Thus, utilizing MPC allows for the reduction of thermal stress on GaN devices by employing the switching frequency as a control variable.

5.3.5 Discussion about ATC scheme

The conducted experiments offer several points for consideration. The implementation of an ATC scheme undeniably achieves the intended goal of reducing thermal stress in power converters. Leveraging an MPC controller effectively mitigates stress by utilizing its understanding of system behavior with measured variables. However, it's essential to acknowledge that the implementation of such a controller demands a model, a process demonstrated in this work, yet known to be time-consuming and relatively complex compared to the PI controller. Even if successfully implemented, there might be operational similarities to a hysteresis controller, aiming for optimal use of performance saturations, particularly in the case of switching frequency.

Furthermore, the introduction of high-frequency harmonics in the current, resulting from varying the switching frequency, should be considered. Depending on the system, this may be detrimental due to EMI noise or potential resonances. In the context of EV powertrain systems, such concerns are mitigated, given their well-understood nature, and active filters have been considered to address potential challenges.

Contrary to the conceptual notion that high switching frequencies increase losses in the system, the impact on efficiency was analyzed and found to be less severe than anticipated. Operating at high output power tends to yield similar efficiency levels, irrespective of the switching frequency at which the system operates.

A critical aspect for the efficacy of the ATC scheme is the analysis of the operating range within which the system functions. Operating with high current may result in the absence of a switching frequency capable of maintaining a low constant temperature. Conversely, operating with low current may lead to consistently high-frequency switching with poor efficiency. Therefore, the careful selection of the reference temperature, considering the nominal operation of the system, becomes paramount.

Chapter 6

CONCLUSIONS

6.1 Summary

BASICALLY, two types of controllers are analyzed in this work to decouple current and temperature control. The conventional controller in power electronic systems is the Proportional-Integral (PI) controller, while Model Predictive Control (MPC) has gained popularity in recent decades due to its advantages in optimal control with fast dynamics, better response to measurable disturbances, and advancements in control technologies.

Initially, the DC-DC buck converter based on Gallium Nitride (GaN) devices was mathematically analyzed, considering various aspects to obtain a model close to reality. This involved accounting for dead time in switching signals and parasitic and conduction resistances. A relationship with the Cauer model was established, linking the junction temperature of GaN devices with loss powers that increase quadratically with the current and linearly with the switching frequency.

Subsequently, a controller based on the electrical model was proposed to optimally control the inductor current and follow a current reference. Simultaneously, using a similar optimization problem structure, a controller based on the loss model was proposed to control temperature. Simulations demonstrated the effectiveness of the proposed control schemes, initially utilizing a thermal model implemented in PLECS with information from datasheet.

Finally, the theoretical mathematical analysis and simulations were experimentally validated. Optimal current control was achieved, outperforming the PI controller in terms of dynamics. After numerous long-term experiments, sufficient data were obtained to propose a dynamic thermal model, approximated to a first-order system dependent on current and switching frequency. Implementing the PI controller in temperature control confirmed the benefits of including an Active Thermal Control (ATC) scheme to reduce thermal stress. Subsequently, the MPC controller was introduced, showcasing significant improvements in minimizing thermal stress during power changes.

6.2 Conclusions

The Continuous Control Set Model Predictive Control (CCS-MPC) demonstrates superior dynamic response compared to a Proportional-Integral (PI) controller, efficiently leveraging actuation

saturation. The implementation of a quantized switching frequency proves pivotal in minimizing switching losses. Synchronized sampling in the current control loop, unaffected by fluctuations, enables accurate average value sampling. However, MPC controllers require compensation for disturbances and modeling inaccuracies due to their significant reliance on the system model. The proposed control strategy facilitates the explicit formulation of control laws and maximizes the efficient use of system saturations.

The efficacy of MPC heavily depends on the precision of the model. In contrast, PI controllers exhibit robust control capabilities, requiring only a reasonable approximation of the model for adjustments.

When employing MPC, accounting for implementation delays is imperative to prevent overshoot or instability. PI controllers can manage adequately without considering these delays, albeit at the cost of increased oscillation and overshoot.

MPC excels in handling actuation saturations more adeptly than PI controllers, achieving faster dynamic responses and superior disturbance rejection for measurable or estimable perturbations. PI controllers necessitate anti-windup schemes and feedforward mechanisms to mimic similar behaviors.

In buck converters, thermal MPC is markedly more advantageous than voltage or current MPC due to its quicker response, aiding in maintaining a stable temperature profile. For boost converters, however, MPC outperforms PI in voltage control due to the presence of a non-minimum phase zero.

Losses in GaN converters are influenced by current and switching frequency rather than output power or voltage.

Similar efficiency can be attained at high output powers regardless of the switching frequency.

Total losses in buck converters reach a minimum at a switching frequency close to 200 kHz, resulting in enhanced efficiency regardless of the current level. This improvement is attributed to the reduction in power loss within the inductor as current ripple decreases and the significant reduction in parasitic resistance at higher frequencies, remaining nearly constant at 200 kHz.

Quantizing the control switching frequencies restricts the ability of PI controllers to accurately meet the temperature reference. In contrast, MPC can achieve the reference temperature by operating as a hysteresis between correct frequency multiples.

6.3 Future Work

Future work in this research encompasses the experimental validation of the control strategy proposed for the Two-Level Boost Converter, as well as its extension to multilevel DC-DC converters like the Three-Level Buck-Boost Converter (TLBBC) and AC-DC inverters, such as the Two-Level Voltage-Source Inverter (2L-VSI). It also involves employing the proposed powertrain system as a whole, which includes a boost converter, a buck converter, an inverter, and a motor.

The implementation of the I2C communication protocol on the MicroLabBox FPGA for direct temperature measurement from GY-906 sensors is another aspect of future work.

Further objectives include analyzing and comparing active thermal control using fans for the heatsink by evaluating the power required to run them at different speeds against the losses incurred from switching, and examining their impact on temperature dynamics and steady-state performance.

An increase in output power and current levels is also targeted.

Lastly, exploring bidirectional operation to simulate regenerative braking and its distinct effects compared to the unidirectional scenario previously studied is considered for future investigation.

Appendix A

ARDUINO UNO C CODES

In order to obtain the temperatures from the GY-906 sensors, the `"Adafruit_MLX90614.h"` library must be utilized. The objects are structured with `"Adafruit_MLX90614 sensorIR"` and must be initialized with an address using `sensorIR.begin(addrIR)`, which defaults to `"0x5A"`. As several sensors are employed, the default address must be altered; this is achieved as shown in Code A.2.

Once the temperature data is obtained as floating-point values, they must be converted to integer values. Considering their precision to two decimal places, truncation is performed using `int(T*100)`. Subsequently, the data is transmitted via the serial port (UART) using the `Serial.write(lsb)` function, which enables the sending of 8 bits. Given that `int` variables are 16 bits in size, the `sendInt16()` function is devised to decompose the variable into two bytes, sending the Less Significant Bits (LSB) followed by the Most Significant Bits (MSB). Since a UART communication module with custom storage has been configured, the key `"0x5555"` must be sent first to indicate that the temperatures will be received in order.

```
#include <Wire.h>
#include <Adafruit_MLX90614.h>
#define IRA 0x5A
#define IRB 0x5B
#define IRC 0x5C
float TcA = 0.0;
float TcB = 0.0;
float ThC = 0.0;
float TaC = 0.0;
int TcA_int = 0;
int TcB_int = 0;
int ThC_int = 0;
int TaC_int = 0;
Adafruit_MLX90614 sensorIRA;
Adafruit_MLX90614 sensorIRB;
Adafruit_MLX90614 sensorIRC;
void setup() {
  sensorIRA.begin(IRA);
  sensorIRB.begin(IRB);
  sensorIRC.begin(IRC);
```

```
21    Serial.begin(115200);
22  }
23  void loop() {
24    digitalWrite(8,HIGH);
25    while(!digitalRead(2));
26    digitalWrite(8,LOW);
27    TcA = sensorIRA.readObjectTempC();  //Case A temperature
28    TcB = sensorIRB.readObjectTempC();  //Case B temperature
29    ThC = sensorIRC.readObjectTempC();  //Heatsink temperature
30    TaC = sensorIRD.readAmbientTempC(); //Ambient temperature
31    TcA_int = int(TcA*100);
32    TcB_int = int(TcB*100);
33    ThC_int = int(ThC*100);
34    TaC_int = int(TaC*100);
35    sendInt16(0x5555);
36    sendInt16(TcA_int);
37    sendInt16(TcB_int);
38    sendInt16(ThC_int);
39    sendInt16(TaC_int);
40    delay(10);
41  }
42  void sendInt16(int data){
43    uint8_t msb = (data >> 8) & 0xFF; //Get byte MSB
44    uint8_t lsb = data & 0xFF;        //Get byte LSB
45    delayMicroseconds(100);
46    Serial.write(lsb);                //Send byte LSB
47    delayMicroseconds(100);           //Wait 100us to send next byte
48    Serial.write(msb);                //Send byte MSB
49  }
```

Listing A.1: Arduino code to get temperatures from IR sensors

```
1  #include <Wire.h> // I2C library, required for MLX90614
2  #include <SparkFunMLX90614.h> // SparkFunMLX90614 Arduino library
3
4  IRTherm therm; // Create an IRTherm object to interact with throughout
5
6  const byte oldAddress = 0x5A;
7  const byte newAddress = 0x5D;
8  int powerPin = 5; //connect sensor VDD to pin 5
9
10 void setup()
11 {
12   pinMode(powerPin, OUTPUT);
13   digitalWrite(powerPin, HIGH);
14   Serial.begin(115200); // Initialize Serial to log output
15   Serial.println("Press a key to begin");
16   while (!Serial.available()) ;
17
18   therm.begin(oldAddress); // Try using the old address first
19
20   byte address;
21   if (!therm.readID()) // Try reading the ID registers
22   {
23     // If the read fails, try re-initializing with the
24     // new address. Maybe we've already set it.
25     therm.begin(newAddress);
26
```

```
27      if (therm.readID()) // Read from the ID registers
28      { // If the read succeeded, print the ID:
29        Serial.println("Communicated with new address.");
30        Serial.println("ID: 0x" +
31                       String(therm.getIDH(), HEX) +
32                       String(therm.getIDL(), HEX));
33      }
34      else
35      {
36        Serial.println("Failed to communicate with either address.");
37      }
38    }
39    else
40    {
41      // If the read suceeds, change the address to something
42      // new.
43      if (!therm.setAddress(newAddress))
44      {
45        Serial.println("Failed to set new address.");
46      }
47      else
48      {
49        Serial.println("Set the address to 0x" + String(newAddress, HEX));
50        Serial.println("Cycle power to try it out.");
51      }
52    }
53    digitalWrite(powerPin, LOW);
54  }
55
56  void loop(){
57  }
```

Listing A.2: Arduino code to set new address to IR sensors

Appendix B

PUBLICATIONS GENERATED

The following publications have been completely derived from the research involved in the development of this thesis project.

ISI Journal Articles Submitted

- A. M. Alcaide, J. G. Berger, A. Stowhas, A. H. Wilson-Veas, E. Zafra, C. A. Rojas, G. Buticchi and S. Kouro, "The Impact of Modulation Techniques on Power Device Aging in Two-Level VSI Converters", IEEE Transactions on Industrial Electronics, May 2023.

International Conferences

- J. G. Berger, C. A. Rojas, C. M. Hackl and M. Aguirre, "Continuous-Control-Set Model Predictive Control with Active Thermal Control in GaN-based DC-DC Converters for EV applications," *2023 IEEE 8th Southern Power Electronics Conference and 17th Brazilian Power Electronics Conference (SPEC/COBEP)*, Florianopolis, Brazil, 2023, pp. 1-7, doi: 10.1109/SPEC56436.2023.10407859.

Projects related with the research

- ANID: FONDECYT Regular 1210757, Universidad Técnica Federico Santa María, Ph.D. Christian Rojas
- ANID: Basal Project FB0008, Universidad Técnica Federico Santa María, Advanced Center for Electrical and Electronic Engineering (AC3E), Ph.D. Christian Rojas
- Dirección de Postgrado y Programas: PIIC - "Análisis del impacto de técnicas de modulación en dispositivos de potencia en convertidores inversores fuente de voltaje de dos niveles", Universidad Técnica Federico Santa María, Ph.D. Christian Rojas

REFERENCES

[1] J. Rodriguez, F. Blaabjerg, and M. P. Kazmierkowski, "Energy Transition Technology: The Role of Power Electronics," *Proceedings of the IEEE*, vol. 111, no. 4, pp. 329–334, 2023.

[2] L. R. B. (2023) The environmental impact of battery production for electric vehicles. [Online]. Available: https://earth.org/environmental-impact-of-battery-production/

[3] J. Marsh. (2022) The environmental impact of electric car batteries. [Online]. Available: https://environment.co/the-environmental-impact-of-electric-car-batteries/

[4] D. A. Notter, M. Gauch, R. Widmer, P. Wäger, A. Stamp, R. Zah, and H.-J. Althaus, "Contribution of li-ion batteries to the environmental impact of electric vehicles," *Environmental Science & Technology*, vol. 44, no. 17, pp. 6550–6556, 2010, pMID: 20695466. [Online]. Available: https://doi.org/10.1021/es903729a

[5] M. Campbell. (2022) Los campos de litio en sudamérica revelan el lado oscuro de nuestro futuro "verde". [Online]. Available: https://es.euronews.com/green/2022/02/03/los-campos-de-litio-en-sudamerica-revelan-el-lado-oscuro-de-nuestro-futuro-verde#:~:text=La%20extracci%C3%B3n%20de%20litio%20perjudica,provoca%20la%20contaminaci%C3%B3n

[6] Z. Hausfather. (2019) Factcheck: How electric vehicles help to tackle climate change. [Online]. Available: https://www.carbonbrief.org/factcheck-how-electric-vehicles-help-to-tackle-climate-change/

[7] M. S. Koroma, D. Costa, M. Philippot, G. Cardellini, M. S. Hosen, T. Coosemans, and M. Messagie, "Life cycle assessment of battery electric vehicles: Implications of future electricity mix and different battery end-of-life management," *The Science of the total environment*, vol. 831, p. 154859, 2022, copyright © 2022 The Author(s). Published by Elsevier B.V. All rights reserved.

[8] Blackridge Research & Consulting. (2024) What is an agm battery? how are agm batteries different from other batteries? [Online]. Available: https://www.blackridgeresearch.com/blog/what-is-an-agm-battery-meaning-advantages-disadvantages-uses-vs-standard-gel-lead-acid-lithium-flooded-battery

[9] S. Rivera, S. M. Goetz, S. Kouro, P. W. Lehn, M. Pathmanathan, P. Bauer, and R. A. Mastromauro, "Charging infrastructure and grid integration for electromobility," *Proceedings of the IEEE*, vol. 111, no. 4, pp. 371–396, 2023.

[10] R. González, "Convertidor dc-dc basado en semiconductores gan con control activo de temperatura para aplicaciones en vehículos eléctricos," Master's thesis, Universidad Técnica Federico Santa María, July 2021.

[11] K. Vidyanandan, "Batteries for electric vehicles," 11 2019.

[12] Y. Xu *et al.*, "Maximizing efficiency in smart adjustable dc link powertrains with igbts and sic mosfets via optimized dc-link voltage control," *Batteries*, vol. 9, no. 6, 2023.

[13] Y. Xie, C. Wang, X. Hu, X. Lin, Y. Zhang, and W. Li, "An mpc-based control strategy for electric vehicle battery cooling considering energy saving and battery lifespan," *IEEE Transactions on Vehicular Technology*, vol. 69, no. 12, pp. 14 657–14 673, 2020.

[14] S. Rivera, S. Kouro, and B. Wu, *Charging Architectures for Electric and Plug-In Hybrid Electric Vehicles*. Cham: Springer International Publishing, 2017, pp. 111–149. [Online]. Available: https://doi.org/10.1007/978-3-319-43651-7_4

[15] H. Vella, "Electric vehicles charging back: From electric school buses to nissan leafs, can vehicle-to-grid technology accelerate the clean-energy revolution?" *Engineering & Technology*, vol. 15, no. 7/8, pp. 32–37, 2020.

[16] G. G. Farivar, W. Manalastas, H. D. Tafti, S. Ceballos, A. Sanchez-Ruiz, E. C. Lovell, G. Konstantinou, C. D. Townsend, M. Srinivasan, and J. Pou, "Grid-connected energy storage systems: State-of-the-art and emerging technologies," *Proceedings of the IEEE*, vol. 111, no. 4, pp. 397–420, 2023.

[17] H. Ben Sassi, F. Errahimi, N. Essbai, and C. Alaoui, "V2g and wireless v2g concepts: State of the art and current challenges," in *2019 International Conference on Wireless Technologies, Embedded and Intelligent Systems (WITS)*, 2019, pp. 1–5.

[18] E. Espina, J. Llanos, C. Burgos-Mellado, R. Cárdenas-Dobson, M. Martínez-Gómez, and D. Sáez, "Distributed control strategies for microgrids: An overview," *IEEE Access*, vol. 8, pp. 193 412–193 448, 2020.

[19] C. Cheng, F. Xie, B. Zhang, D. Qiu, W. Xiao, and H. Ji, "Modeling and nonlinear dynamic analysis of cascaded dc–dc converter systems based on simplified discrete mapping," *IEEE Transactions on Industrial Electronics*, vol. 70, no. 6, pp. 5830–5839, 2023.

[20] B. Stevanović, G. Salinas, P. Alou, J. A. Cobos, and M. Vasić, "Comparative evaluation of the two multilevel concepts with full zvs operation employing wbg devices for use in 1500-v pv systems," *IEEE Transactions on Industry Applications*, vol. 58, no. 3, pp. 3922–3935, 2022.

[21] A. I. Emon, M. ul Hassan, A. B. Mirza, J. Kaplun, S. S. Vala, and F. Luo, "A review of high-speed gan power modules: State of the art, challenges, and solutions," *IEEE Journal of Emerging and Selected Topics in Power Electronics*, vol. 11, no. 3, pp. 2707–2729, 2023.

[22] M. Buffolo, D. Favero, A. Marcuzzi, C. D. Santi, G. Meneghesso, E. Zanoni, and M. Meneghini, "Review and outlook on gan and sic power devices: Industrial state-of-the-art, applications, and perspectives," *IEEE Transactions on Electron Devices*, pp. 1–12, 2024.

[23] S. Biswas, D. Reusch, and M. de Rooij, "Design of gan-based multilevel switched capacitor converters—benefits and challenges," *IEEE Transactions on Industry Applications*, vol. 56, no. 2, pp. 979–988, 2020.

[24] K. Peng and E. Santi, "Characterization and modeling of a gallium nitride power hemt," in *2014 IEEE Energy Conversion Congress and Exposition (ECCE)*, 2014, pp. 113–120.

[25] GaN Systems Inc., "GS66516B 650 V E-mode GaN transistor Datasheet," 2020. [Online]. Available: https://gansystems.com/wp-content/uploads/2018/04/GS66516B-DS-Rev-180422.pdf

[26] A. M. Bouchour, A. E. Oualkadi, O. Latry, P. Dherbécourt, and A. Echeverri, "Estimation of losses of gan hemt in power switching applications based on experimental characterization," *Computers & Electrical Engineering*, vol. 84, p. 106622, 2020. [Online]. Available: https://www.sciencedirect.com/science/article/pii/S0045790620304778

[27] G. Liu, K. H. Bai, M. McAmmond, A. Brown, P. M. Johnson, A. Taylor, and J. Lu, "Comparison of sic mosfets and gan hemts based high-efficiency high-power-density 7.2kw ev battery chargers," in *2017 IEEE 5th Workshop on Wide Bandgap Power Devices and Applications (WiPDA)*, 2017, pp. 391–397.

[28] H. Bai, C. Liu, S. Zhuo, R. Ma, D. Paire, and F. Gao, "Fpga-based device-level electro-thermal modeling of floating interleaved boost converter for fuel cell hardware-in-the-loop applications," *IEEE Transactions on Industry Applications*, vol. 55, no. 5, pp. 5300–5310, 2019.

[29] Semikron, "SK25GH12T4 IGBT Module Datasheet," 2012. [Online]. Available: https://www.semikron-danfoss.com/dl/service-support/downloads/download/semikron-datasheet-sk-25-gh-12t4-24917100.pdf

[30] C. Rojas, "Multiobjective finite control set model predictive torque and stator flux control of an induction machine," PhD thesis, Universidad Técnica Federico Santa María, July 2013.

[31] R. K. K, D. Sankar, and H. T, "A comprehensive review on finite control set model predictive control: Trends and prospects," in *2022 Third International Conference on Intelligent Computing Instrumentation and Control Technologies (ICICICT)*, 2022, pp. 206–210.

[32] N. Rai and S. Chakravorty, "A review on the generalized formulations for selective harmonic elimination (she-pwm) strategy," in *2020 IEEE First International Conference on Smart Technologies for Power, Energy and Control (STPEC)*, 2020, pp. 1–6.

[33] M. P. Kazmierkowski, R. Krishnan, and F. Blaabjerg, "Control in power electronics: selected problems," 2002. [Online]. Available: https://api.semanticscholar.org/CorpusID:107395465

[34] M. Jeong and J. Biela, "Dynamic Voltage Control of Converters with LC-filters Using Model Predictive Control: Impacts on Grid-Forming and Grid-Following Control," in *2023 11th International Conference on Power Electronics and ECCE Asia (ICPE 2023 - ECCE Asia)*, 2023, pp. 1302–1308.

[35] M. Jeong, M. Schoen, and J. Biela, "When FPGAs Meet ADMM with High-level Synthesis (HLS): A Real-time Implementation of Long-horizon MPC for Power Electronic Systems," in *2023 11th International Conference on Power Electronics and ECCE Asia (ICPE 2023 - ECCE Asia)*, 2023, pp. 1704–1711.

[36] R. Ramos, D. Serrano, P. Alou, J. Oliver, and J. A. Cobos, "Control design of a single-phase inverter operating with multiple modulation strategies and variable switching frequency," *IEEE Transactions on Power Electronics*, vol. 36, no. 2, pp. 2407–2419, 2021.

[37] C. Suthar, V. I. Kumar, F. Alskran, and D. Maksimović, "An arbitrary waveform generator based on an eight-level flying-capacitor multilevel converter," in *2021 IEEE Applied Power Electronics Conference and Exposition (APEC)*, 2021, pp. 1008–1014.

[38] ——, "Estimator-Based Time-Optimal Control of Flying Capacitor Multilevel (FCML) Converters," in *2022 IEEE 23rd Workshop on Control and Modeling for Power Electronics (COMPEL)*, 2022, pp. 1–6.

[39] C. Suthar, V. I. Kumar, and D. Maksimović, "Estimator-based step-load transient improvements in a digitally controlled synchronous buck converter," in *2023 IEEE Applied Power Electronics Conference and Exposition (APEC)*, 2023, pp. 1189–1194.

[40] D. Jordan and J. Korn, "Deadbeat algorithms for multivariable process control," *IEEE Transactions on Automatic Control*, vol. 25, no. 3, pp. 486–491, 1980.

[41] X. Sun, X. Lin, D. Guo, G. Lei, and M. Yao, "Improved deadbeat predictive current control with extended state observer for dual three-phase pmsms," *IEEE Transactions on Power Electronics*, pp. 1–13, 2024.

[42] B. Zoghdar-Moghadam-Shahrekohne, A. Pozzi, and D. M. Raimondo, "Sos-based stability region enlargement of bilinear power converters through model predictive control," in *2021 29th Mediterranean Conference on Control and Automation (MED)*, 2021, pp. 847–854.

[43] S. H. Kafash *et al.*, "Model predictive control of bilinear systems as uncertain linear systems," in *2022 IEEE CCTA*, 2022, pp. 562–567.

[44] M. Ghadimi and J. Nazarzadeh, "On the Minimum Time Tracking Control of the Active Front End Converters," *IEEE Journal of Emerging and Selected Topics in Power Electronics*, vol. 10, no. 6, pp. 7029–7036, 2022.

[45] A. Safaeinasab, H. S. Gohari, and K. Abbaszadeh, "Design and control of a novel multi-port bidirectional buck-boost converter suitable for hybrid electric vehicle charging stations," in *2022 30th International Conference on Electrical Engineering (ICEE)*, 2022, pp. 1027–1032.

[46] Q. Yang, P. Karamanakos, W. Tian, X. Gao, X. Li, T. Geyer, and R. Kennel, "Computationally efficient fixed switching frequency direct model predictive control," *IEEE Transactions on Power Electronics*, vol. 37, no. 3, pp. 2761–2777, 2022.

[47] X. Zhang, G. Tan, X. Wu, Q. Wang, W. Zhang, T. Xia, and T. Shi, "Single-phase three-level pwm rectifier predictive control with fixed switching frequency based on current convex optimization," *IEEE Transactions on Power Electronics*, vol. 36, no. 10, pp. 12 090–12 101, 2021.

[48] Z. Zheng, S. J. Baek, D. H. Yu, and K. T. Chong, "Comparison study of the taylor series based discretization method for nonlinear input-delay systems," in *2013 Australian Control Conference*, 2013, pp. 397–402.

[49] G. D. Meena and J. Sivaramakrishnan, "Taylor discretization based class of exactly discretizable nonlinear systems," *IFAC-PapersOnLine*, vol. 49, no. 1, pp. 510–515, 2016, 4th IFAC Conference on Advances in Control and Optimization of Dynamical Systems ACODS 2016. [Online]. Available: https://www.sciencedirect.com/science/article/pii/S2405896316301057

[50] C. A. Silva and J. I. Yuz, "On sampled-data models for model predictive control," in *IECON 2010 - 36th Annual Conference on IEEE Industrial Electronics Society*, 2010, pp. 2966–2971.

[51] C. A. Rojas, J. I. Yuz, M. Aguirre, and J. Rodriguez, "A comparison of discrete-time models for model predictive control of induction motor drives," in *2015 IEEE International Conference on Industrial Technology (ICIT)*, 2015, pp. 568–573.

[52] R. H. Cuzmar, A. Mora, J. Pereda, P. Poblete, and R. P. Aguilera, "Long-Horizon Sequential FCS-MPC Approaches for Modular Multilevel Matrix Converters," *IEEE Transactions on Industrial Electronics*, p. Early Access, 2023.

[53] P. Cortes, J. Rodriguez, C. Silva, and A. Flores, "Delay compensation in model predictive current control of a three-phase inverter," *IEEE Transactions on Industrial Electronics*, vol. 59, no. 2, pp. 1323–1325, 2012.

[54] H. Chen, S. Tang, D. Wang, C. Zhang, Z. Zeng, and J. Wang, "Model predictive control based on state-space averaging model for three-level flying capacitor boost converter with constant switching frequency and improved dynamic performance," in *2020 IEEE 9th International Power Electronics and Motion Control Conference (IPEMC2020-ECCE Asia)*, 2020, pp. 3051–3056.

[55] H. Chen, D. Wang, S. Tang, X. Yin, J. Wang, and Z. J. Shen, "Continuous control set model predictive control for three-level flying capacitor boost converter with constant switching frequency," *IEEE Journal of Emerging and Selected Topics in Power Electronics*, vol. 9, no. 5, pp. 5996–6007, 2021.

[56] X. Gao, Y. Pang, J. Xia, N. Chai, W. Tian, J. Rodriguez, and R. Kennel, "Modulated model predictive control of modular multilevel converters operating in a wide frequency range," *IEEE Transactions on Industrial Electronics*, vol. 70, no. 5, pp. 4380–4391, 2023.

[57] J. S. Arora, "Chapter 4 - optimum design concepts: Optimality conditions," in *Introduction to Optimum Design (Third Edition)*, third edition ed., J. S. Arora, Ed. Boston: Academic Press, 2012, pp. 95–187. [Online]. Available: https://www.sciencedirect.com/science/article/pii/B9780123813756000048

[58] W. Wang, Y. Liu, Y. Chen, and C. Liu, "Optimization-based duty cycle allocation for a five-leg inverter to drive two electric motors," *IEEE Transactions on Power Electronics*, vol. 38, no. 9, pp. 11 327–11 337, 2023.

[59] O. Arpacik and M. M. Ankarali, "An efficient implementation of online model predictive control with field weakening operation in surface mounted pmsm," *IEEE Access*, vol. 9, pp. 167 605–167 614, 2021.

[60] D. Goldfarb and A. Idnani, "A numerically stable dual method for solving strictly convex quadratic programs," *Mathematical Programming*, vol. 27, no. 1, pp. 1–33, 09 1983. [Online]. Available: https://doi.org/10.1007/BF02591962

[61] G. Cimini, D. Bernardini, S. Levijoki, and A. Bemporad, "Embedded model predictive control with certified real-time optimization for synchronous motors," *IEEE Transactions on Control Systems Technology*, vol. 29, no. 2, pp. 893–900, 2021.

[62] I. Hammoud, S. Hentzelt, K. Xu, T. Oehlschlägel, M. Abdelrahem, C. Hackl, and R. Kennel, "On continuous-set model predictive control of permanent magnet synchronous machines," *IEEE Transactions on Power Electronics*, vol. 37, no. 9, pp. 10 360–10 371, 2022.

[63] J.-M. De Paris, H. Pinheiro, F. d. M. Carnielutti, V. F. Montagner, and D. M. Lima, "Mpc for grid forming converters with current limiting," in *IECON 2022 – 48th Annual Conference of the IEEE Industrial Electronics Society*, 2022, pp. 1–5.

[64] D. Schuetz, C. R. D. Osório, L. A. Maccari, D. M. Lima, F. d. M. Carnielutti, V. F. Montagner, and H. Pinheiro, "Space vector modulated model predictive control for grid-tied converters," *IEEE Transactions on Industrial Informatics*, vol. 19, no. 1, pp. 414–425, 2023.

[65] L. Zhou and M. Preindl, "Optimal-frequency critical soft switching method of synchronous dc/dc converter based on model predictive control," in *2019 IEEE Applied Power Electronics Conference and Exposition (APEC)*, 2019, pp. 2989–2994.

[66] ——, "Variable-switching constant-sampling frequency critical soft switching mpc for dc/dc converters," *IEEE Transactions on Energy Conversion*, vol. 36, no. 2, pp. 1548–1561, 2021.

[67] T. Hagawane, M. R. Sindhu, and R. Patankar, "Model predictive control of dual active bridge dc-dc converter based on pwm plus tps modulation for automotive applications," in *2022 International Virtual Conference on Power Engineering Computing and Control: Developments in Electric Vehicles and Energy Sector for Sustainable Future (PECCON)*, 2022, pp. 1–6.

[68] S. A. S. Schürch, P. L. Illesca, and C. A. Rojas, "Comparison of control schemes for a gan-based eight-cell flying capacitor converter dc/dc with enhanced loss model," in *2023 IEEE CHILEAN Conference on Electrical, Electronics Engineering, Information and Communication Technologies (CHILECON)*, 2023, pp. 1–6.

[69] A. Soldati, F. Dossena, G. Pietrini, D. Barater, C. Concari, and F. Iannuzzo, "Thermal stress mitigation by active thermal control: Architectures, models and specific hardware," in *2017 IEEE Energy Conversion Congress and Exposition (ECCE)*, 2017, pp. 3822–3829.

[70] S. Rahimpour, H. Tarzamni, N. V. Kurdkandi, O. Husev, D. Vinnikov, and F. Tahami, "An overview of lifetime management of power electronic converters," *IEEE Access*, vol. 10, pp. 109 688–109 711, 2022.

[71] D. Murdock, J. Torres, J. Connors, and R. Lorenz, "Active thermal control of power electronic modules," *IEEE Transactions on Industry Applications*, vol. 42, no. 2, pp. 552–558, 2006.

[72] Q. Zheng, Z. Ping, S. Soares, Y. Hu, and Z. Gao, "An active disturbance rejection control approach to fan control in servers," in *2018 IEEE Conference on Control Technology and Applications (CCTA)*, 2018, pp. 294–299.

[73] Q. Zheng and Z. Ping, "Active disturbance rejection control for server thermal management," in *2018 5th International Conference on Control, Decision and Information Technologies (CoDIT)*, 2018, pp. 158–163.

[74] J. Falck, M. Andresen, and M. Liserre, "Active thermal control of igbt power electronic converters," 11 2015, pp. 000 001–000 006.

[75] R. González, C. A. Rojas, and L. Callegaro, "Three-level dc-dc gan-based converter with active thermal control for powertrain applications in electric vehicles," in *2021 22nd IEEE International Conference on Industrial Technology (ICIT)*, vol. 1, 2021, pp. 502–507.

[76] C. A. Rojas, R. Gonzalez, L. Callegaro, and H. Young, "Mission profile-oriented active thermal control of a bidirectional three-level buck-boost gan-based dc-dc converter for electric vehicles powertrains," in *IECON 2021 – 47th Annual Conference of the IEEE Industrial Electronics Society*, 2021, pp. 1–6.

[77] A. Chanekar, N. Deshmukh, A. Arya, and S. Anand, "Gate voltage-based active thermal control of power semiconductor devices," *IEEE Transactions on Power Electronics*, vol. 38, no. 9, pp. 11 531–11 542, 2023.

[78] C. Zhang, X. Yuan, J. Wang, B. Hu, X. Yin, and Z. J. Shen, "Optimization of power sharing and switching frequency in si/wbg hybrid half-bridge converters using power loss models," *IEEE Journal of Emerging and Selected Topics in Power Electronics*, vol. 11, no. 3, pp. 2837–2849, 2023.

[79] R. Han, Q. Xu, H. Ding, P. Guo, J. Hu, Y. Chen, and A. Luo, "Thermal stress balancing oriented model predictive control of modular multilevel switching power amplifier," *IEEE Transactions on Industrial Electronics*, vol. 67, no. 11, pp. 9028–9038, 2020.

[80] R. Han, Q. Xu, L. Wang, C. Tang, B. Gao, J. Wang, and A. Luo, "Modulated model predictive control for reliability improvement of extremely low frequency power amplifier via junction temperature swing reduction," *IEEE Transactions on Industrial Electronics*, vol. 69, no. 1, pp. 302–313, 2022.

[81] Z. Li, M. Zhou, and H. Wang, "Temperature sensorless thermal management strategy for interleaving power converters," in *2022 International Power Electronics Conference (IPEC-Himeji 2022- ECCE Asia)*, 2022, pp. 466–470.

[82] Z. Li, J. Liang, and H. Wang, "Weight judgement based thermal balancing strategy for interleaved buck converters," in *2022 IEEE Energy Conversion Congress and Exposition (ECCE)*, 2022, pp. 1–6.

[83] J. Sheng, C. Chen, B. Li, X. Xiang, H. Yang, X. Zhang, and W. Li, "Thermal distribution analysis of modular multilevel dc-dc converters," in *2022 IEEE International Power Electronics and Application Conference and Exposition (PEAC)*, 2022, pp. 21–26.

[84] C. Yang, T. Peng, X. Huang, X. Fan, H. Tao, C. Yang, and W. Gui, "Electrothermal performance-based fcs-mpc for dynamic thermal balance control of traction converters," *IEEE Transactions on Transportation Electrification*, vol. 8, no. 1, pp. 277–287, 2022.

[85] F. A. Villarroel, J. R. Espinoza, M. A. Pérez, C. R. Baier, J. A. Rohten, R. O. Ramírez, E. S. Pulido, and J. J. Silva, "A predictive shortest-horizon voltage control algorithm for non-minimum phase three-phase rectifiers," *IEEE Access*, vol. 10, pp. 107 598–107 615, 2022.

[86] GaN Systems Inc., "High Power IMS Evaluation Platform Technical Manual," 2021. [Online]. Available: https://gansystems.com/wp-content/uploads/2020/05/GSP65RXXHB-EVB_Technical-Manual_Rev_200526.pdf

[87] J. Rawlings, D. Mayne, and M. Diehl, *Model Predictive Control: Theory, Computation, and Design*. Nob Hill Publishing, 2017. [Online]. Available: https://books.google.cl/books?id=MrJctAEACAAJ

[88] L. Grüne and J. Pannek, *Nonlinear Model Predictive Control*. Cham: Springer International Publishing, 2017, pp. 45–69. [Online]. Available: https://doi.org/10.1007/978-3-319-46024-6_3

[89] L. Wang, "A tutorial on predictive repetitive control," in *2016 Australian Control Conference (AuCC)*, 2016, pp. 114–119.

[90] E. Aydiner, M. A. Müller, and F. Allgöwer, "Periodic reference tracking for nonlinear systems via model predictive control," in *2016 European Control Conference (ECC)*, 2016, pp. 2602–2607.

[91] J. C. Holladay, "The stone-weierstrass theorem for quaternions," *Proc. Amer. Math. Soc.*, vol. 8, p. 656, 1957.

[92] J. Maciejowski, *Predictive Control: With Constraints*. Prentice Hall, 2002. [Online]. Available: https://books.google.cl/books?id=HV_Y58c7KiwC

[93] M. Papageorgiou, M. Leibold, and M. Buss, *Optimierung*. Springer, 2015, vol. 4.

[94] S. Bittanti, P. Bolzern, and P. Colaneri, "Stability analysis of linear periodic systems via the lyapunov equation," *IFAC Proceedings Volumes*, vol. 17, no. 2, pp. 213–216, 1984, 9th IFAC World Congress: A Bridge Between Control Science and Technology, Budapest, Hungary, 2-6 July 1984. [Online]. Available: https://www.sciencedirect.com/science/article/pii/S1474667017609716

[95] T. Ooba and Y. Funahashi, "Stability robustness for linear state space models — a lyapunov mapping approach," *Systems Control Letters*, vol. 29, no. 4, pp. 191–196, 1997. [Online]. Available: https://www.sciencedirect.com/science/article/pii/S0167691196000680

[96] E. F. Camacho and C. Bordons, *Constrained MPC*. London: Springer London, 1999, pp. 167–207. [Online]. Available: https://doi.org/10.1007/978-1-4471-3398-8_7

[97] G. C. Goodwin, S. F. Graebe, and M. E. Salgado, *Control System Design*, 1st ed. USA: Prentice Hall PTR, 2000.